



저작자표시-비영리-변경금지 2.0 대한민국

이용자는 아래의 조건을 따르는 경우에 한하여 자유롭게

- 이 저작물을 복제, 배포, 전송, 전시, 공연 및 방송할 수 있습니다.

다음과 같은 조건을 따라야 합니다:



저작자표시. 귀하는 원저작자를 표시하여야 합니다.



비영리. 귀하는 이 저작물을 영리 목적으로 이용할 수 없습니다.



변경금지. 귀하는 이 저작물을 개작, 변형 또는 가공할 수 없습니다.

- 귀하는, 이 저작물의 재이용이나 배포의 경우, 이 저작물에 적용된 이용허락조건을 명확하게 나타내어야 합니다.
- 저작권자로부터 별도의 허가를 받으면 이러한 조건들은 적용되지 않습니다.

저작권법에 따른 이용자의 권리는 위의 내용에 의하여 영향을 받지 않습니다.

이것은 [이용허락규약\(Legal Code\)](#)을 이해하기 쉽게 요약한 것입니다.

[Disclaimer](#)

공학박사학위논문

기포 플룸에 의해 유도되는 난류  
혼합에 대한 실험 및 이론 연구

**An experimental and theoretical study on turbulent  
mixing induced by bubble plume**

2021년 8월

서울대학교 대학원  
기계항공공학부  
김 현 석



# 기포 플룸에 의해 유도되는 난류 혼합에 대한 실험 및 이론 연구

An experimental and theoretical study on turbulent  
mixing induced by bubble plume

지도교수 박 형 민

이 논문을 공학박사 학위논문으로 제출함

2021년 4월

서울대학교 대학원  
기계항공공학부  
김 현 석

김현석의 공학박사 학위논문을 인준함

2021년 6월

위 원 장	<u>송 성 진</u>
부위원장	<u>박 형 민</u>
위 원	<u>김 호 영</u>
위 원	<u>황 원 태</u>
위 원	<u>김 동 주</u>



# An experimental and theoretical study on turbulent mixing induced by bubble plume

Hyunseok Kim

Department of Mechanical and Aerospace Engineering  
Seoul National University

## Abstract

Turbulent mixing induced by bubble plume occurs over a wide scale range (from  $O(100 \mu\text{m})$  to  $O(1 \text{ km})$ ) accompanying a complex interaction between the gas and the liquid phase, so a precise and systematic understanding of this is desired. However, previous studies have not considered the unsteady behavior of the bubble plume and the turbulence caused by the bubble-liquid interaction. Instead, it has been investigated in terms of time-averaged flow. In this study, the unsteady motion of the bubble plume and the bubble-induced turbulence were examined in detail for two types of bubble plumes, conventional and churn-turbulent, using high-precision optical experimental techniques such as the shadow technique, optical flow method, and laser doppler anemometry. The characteristic length, speed, and time scales that describe unsteady characteristics of the bubble are established. The length scale characterizing the bubble plume was the buoyancy characteristic length scale  $D_m$  in the streamwise direction, the bubble plume radius  $r_{1/2}$  in the radial direction, and the velocity scale was the bubble relative velocity ( $V_{Ro}$ ) and the liquid central velocity ( $U_c$ ). Also, the characteristic time was an integral time scale. Regardless of the bubble plume type, the bubble plume's instability (consists of precession, meandering, and bulge) and turbulence statistics were described as a function of  $z/D_m$ . In the streamwise direction, there are two distinct regions, one is an adjustment region where physical quantities rapidly change and the other is an asymptotic region that converges. The boundary between the adjustment and the asymptotic region was observed as  $z = D_m$ . In addition, the radial distribution of mean and turbulence parameters was well described as  $r/r_{1/2}$ , and it was quantitatively verified that the characteristic velocity, length, and time scale of such a large scale can well represent the characteristics of the bubble plume. Through the turbulent energy spectrum, it was found that the turbulent energy generation by bubbles occurs at the plume scale, which supports that the physical quantity of the bubble plume can be well defined with large characteristic scales. In order to explain the difference in the turbulence statistics after convergence height (the churn-turbulent bubble plume has higher convergent turbulence statistics), which cannot be described on a large characteristic scale, an analytical framework was established. The correlation between the bubble-induced turbulence and the gas phase parameters was derived from the time-averaged two-phase Navier-Stokes equation. The proposed methodology was verified with various bubbly flow geometries such as bubble swarm, bubble plume, and bubbly pipe flow, and it was revealed that the methodology proposed in this study can

analytically justify the previous empirical relations. In addition, it was found that it is necessary to consider the gas-liquid interaction suitable for each situation in order to predict the specific trend of bubble-induced turbulence. Based on the obtained understanding, finally, a criterion for determining the mixing pattern that occurs when a stably stratified fluid is mixed with a bubble plume, and a scaling relation for the mixing velocity are suggested. The mixing pattern was easily predicted by the simple ratio of the buoyancy applied to the bubble plume and the gravity applied to the fluid layer, which consisted of the initial conditions. Furthermore, the mixing velocity is well described by the Froude number which is defined as the ratio of the characteristic velocity of air-liquid interaction to the gravitational force which stabilizes the stratified fluids. Based on the accurate experimental results, this study provides a comprehensive characterization of the turbulent mixing by bubble plume covering from a macroscopic description of the average flow to a specific scaling relation for turbulence statistics. It gives useful knowledge that can be used immediately in the industrial field as well as is an academic achievement that helps understand the physical characteristics of bubble flow.

**Keyword :** turbulent mixing, stably stratified fluids, bubbly flow, bubble plume, bubble-induced turbulence

**Student Number :** 2013-23064





# Table of Contents

<b>Abstract</b>	<b>i</b>
<b>Contents</b>	<b>v</b>
<b>List of Tables</b>	<b>viii</b>
<b>List of Figures</b>	<b>ix</b>
<b>Nomenclature</b>	<b>xv</b>
<b>Chapter</b>	
<b>1. Introduction</b>	<b>1</b>
1.1 Bubble plume	1
1.2 Stratified fluid mixing induced by bubble plume	2
1.3 Outline of the thesis	3
<b>2. Experimental methods</b>	<b>4</b>
2.1 Bubble plume generation and the setup for optical measurement	4
2.1.1 Facility and equipment	4
2.1.2 Regime of bubble plume	5
2.2 Stably stratified fluids mixing induced by bubble plume	6
2.2.1 Stably stratified fluids	6
2.2.2 Optical setup for mixing experiment	7
2.3 Image post-processing algorithm: shadowgraph technique	7
2.3.1 Definition of parameters to characterize bubble plume kinematics	7
2.3.2 Watershed transform for discrimination of overlapped bubbles	9
2.4 Optical flow algorithm to evaluate the gas phase velocity field	11
2.4.1 Lucas-Kanade method	11
2.4.2 Validation of the technique	12
2.5 Laser doppler anemometry (LDA)	12
2.5.1 LDA measurement condition	12
2.5.2 LDA post-processing algorithms	13
2.6 Post-processing on color image to characterize the fluid mixing	13
<b>3. Bubble plume dynamics</b>	<b>26</b>
3.1 Background	26
3.2 Regimes of bubble plume	29

3.3 Gas-phase flow dynamics .....	30
3.3.1 Bubble plume kinematics .....	30
3.3.2 Time-averaged flow field of the gas phase .....	32
3.4 Liquid phase flow dynamics .....	33
3.4.1 Time-averaged flow field of the liquid phase .....	33
3.4.2 Turbulence statistics of the liquid phase .....	36
3.4.3 Characteristic time scales of the bubble-induced turbulence	37
3.4.4 Averaged mass and momentum flow rates of the liquid phase .....	37
3.4.5 Turbulence energy spectra .....	39
3.5 Concluding remarks .....	40
<b>4. An analytical framework to characterize the bubble-induced turbulence</b> .....	<b>58</b>
4.1 Background .....	58
4.2 Scaling analysis of two-phase averaged Navier-Stokes equation .....	63
4.2.1 Revisit to the bubble parameter .....	63
4.2.2 Interfacial momentum transfer term, $\Phi_b$ .....	66
4.2.3 Contribution of surface tension force .....	69
4.3 Relation between total liquid momentum and interfacial momentum transfer for bubble plume .....	69
4.4 Concluding remarks .....	76
<b>5. Stably stratified fluids mixing induced by bubble plume</b> .....	<b>82</b>
5.1 Background .....	82
5.2 Types of the mixing induced by bubble plume .....	83
5.3 Mixing time .....	84
5.4 Mixing velocity .....	85
5.5 Scaling relation on the mixing velocity .....	86
5.6 Concluding remarks .....	88
<b>6. Conclusion</b> .....	<b>102</b>
<b>7. Appendix</b> .....	<b>107</b>
7.1 Relation between total liquid momentum and interfacial momentum transfer for various bubbly flows .....	107
7.1.1 Homogeneous bubble swarm .....	107
7.1.2 Rising bubbles under the prescribed grid turbulence .....	110
7.1.3 Upward bubbly pipe flow .....	112
<b>Bibliography</b> .....	<b>123</b>
<b>Abstract in Korean</b> .....	<b>131</b>



# List of Tables

TABLE 2.1. Ion combination table. Tick: a combination that cause bubble coalescence inhibition. Cross: a combination without coalescence inhibition (the table is taken from Craig 2004). ..... 15

TABLE 3.1. Reference parameters to describe the bubble plume based on 1-D plume model. .... 42

TABLE 4.1. Flow conditions of various bubbly flows characterized with the scaling relation developed in the present study:  $\langle \bar{d}_b \rangle$ , bubble size;  $\langle \alpha \rangle$ , volume void fraction;  $Re_b (= V_R \langle \bar{d}_b \rangle / \nu)$ , bubble Reynolds number;  $Re (= U_c 2L_c / \nu)$ , liquid-phase Reynolds number (in the case of bubble plume,  $L_c = L_r$  and for the bubbly pipe flow,  $Re$  is the bulk Reynolds number before the bubble injection);  $We_b (= \rho_w V_R^2 \langle \bar{d}_b \rangle / \sigma)$ , bubble Weber number;  $We (= \rho U_c^2 L_c / \sigma)$ , Weber number based on liquid-phase scales;  $Fr (= U_c^2 / gL_c)$ , Froude number. Here,  $\langle \rangle$  and the overbar denotes spatial and temporal average respectively, and  $U_c$  and  $L_c$  is the characteristic velocity scale and length scale of the liquid phase, respectively. Without any comment,  $L_c$  is  $L_z$  for the bubble plume and  $L_r$  for the bubbly pipe flow. .... 78

TABLE 5.1. Mixing type depending on density difference and the bubble plume type. .... 89

## List of Figures

- FIGURE 2.1. (a) Schematic of the experimental setup for bubble plume measurement. Bubble plume kinematics and the bubble velocity is taken by high speed camera (b) Typical images for the conventional and churn-turbulent bubble plume. Inset shows the enlarged view. .... 16
- FIGURE 2.2. A regime map of bubble plume. The left side of the dashed line corresponds to conventional bubble plume and the other side is churn-turbulent bubble plume. .... 17
- FIGURE 2.3. Process to make the stably stratified fluids (a) the lower liquid with porous filter (b) the stably stratified fluids (c) the stably stratified liquids 3 hours after first made. .... 18
- FIGURE 2.4. (a) Schematic of the experimental setup for fluid mixing induced by bubble plume with two color CCD camera (b) An example of the image ( $\Delta\rho/\rho_w = 0.016$ ). .... 19
- FIGURE 2.5. Parameterization of bubble plume kinematics (a) Raw image (b) binarized image with the center and the boundary (c) A schematic on the definition of parameters describing bubble plume kinematics. .... 20
- FIGURE 2.6. An example of watershed transform to discriminate overlapped bubbles in conventional bubble plume. Left: Raw image, right: processed result at (a) original image scale (b) enlarged image. .... 21
- FIGURE 2.7. An example of watershed transform to discriminate overlapped bubbles in churn-turbulent bubble plume. Left: Raw image, right: processed result at (a) original image scale (b) enlarged image. .... 22
- FIGURE 2.8. An example of Lucas-Kanade method for (a) conventional bubble plume (b) churn-turbulent bubble plume. .... 23
- FIGURE 2.9. Validation of Lucas-Kanade method with single bubble rising near the wall. Temporal variation of (a) horizontal velocity (b) vertical velocity. (c) Raw image. .... 24

- FIGURE 2.10. z-t contour of B channel image taken at  $x = 200$  mm for conventional bubble plume with  $\Delta\rho/\rho_w = 0.068$ . (a) Before and (b) after the normalization. In (b), the dashed line corresponds to the velocity of the density front descent of lower layer. .... 25
- FIGURE 3.1. (a) A snapshot of the conventional (left) and the churn-turbulent (right) bubble plume.  $d_{50} = 3.35$  mm (conventional bubble plume) and 6.26 mm (churn-turbulent bubble plume). (b) The probability density function of the bubble diameter weighted by its volume. .... 43
- FIGURE 3.2. Temporal structures observed in bubble plume kinematics. (a) Precession radius, (c) meandering radius, and (c) bulge length. 44
- FIGURE 3.3. Time averaged parameters on bubble plume kinematics. (a) Time averaged plume width, (b) bulge amplitude, (c) precession amplitude, and (d) meandering amplitude. .... 45
- FIGURE 3.4. Time averaged parameters on bubble plume kinematics normalized by  $r_{1/2}$ . (a) Time-averaged plume width, (b) bulge amplitude, (c) precession amplitude, and (d) meandering amplitude. .... 46
- FIGURE 3.5. Gas phase parameters: (a) vertical variation of the central relative rise velocity of a bubble and the radial distribution of the (b) time-averaged bubble velocity, and (c) bubble relative velocity. .... 47
- FIGURE 3.6. Time averaged liquid velocity contour obtained by LDA (a)  $U_z$  and (b) Turbulence kinetic energy (Left: conventional bubble plume; Right: churn-turbulent bubble plume). .... 48
- FIGURE 3.7. Time-averaged profiles of (a) liquid axial velocity, and (b) liquid radial velocity. (c) A schematic representing the time-averaged plume velocity field. .... 49
- FIGURE 3.8. Comparison with the previously suggested empirical relation by Lai *et al.* (2019) including the previous results: (a) normalized central velocity, (b) normalized  $r_{1/2}$ , and (c) normalized  $Q_{top-hat}$ . 50
- FIGURE 3.9. Axial variation of the liquid parameters: (a) the inverse of the central velocity normalized by bubble relative velocity, (b) the normalized  $r_{1/2}$ , and (c) the normalized turbulence kinetic energy. 51

FIGURE 3.10. Turbulence statistics of the liquid fluctuation velocity normalized by central velocity. (a) root-mean square vertical velocity, (b) root-mean square radial velocity, (c) skewness of the vertical liquid velocity fluctuation, and (d) flatness of the vertical liquid velocity fluctuation. .... 52

FIGURE 3.11. Characteristic time scales of the liquid vertical velocity fluctuation. (a) Integral time scale, (b) Taylor microscale, and (c) Kolmogorov time scale. .... 53

FIGURE 3.12. Integrated parameters of the induced liquid plume. (a) mass flow rate, (b) total momentum flow rate, (c) mean momentum flow rate, (d) turbulence momentum flow rate, and (e) the ratio of turbulence to mean momentum flow rate. .... 54

FIGURE 3.13. Energy spectrum of the vertical liquid velocity fluctuations at the center ( $r = 0$  mm) and the edge ( $r = 75$  mm) of the induced liquid plume. (a)  $r = 0$  mm,  $z = 50, 100$  mm, (b)  $r = 75$  mm,  $z = 50, 100$  mm, (c)  $r = 0$  mm,  $z = 200, 300$  mm, (d)  $r = 75$  mm,  $z = 200, 300$  mm. .... 55

FIGURE 3.14. Energy spectrum of the vertical liquid velocity fluctuations at the center ( $r = 0$  mm) and the edge ( $r = 75$  mm) of the induced liquid plume normalized by integral time scale. (a)  $r = 0$  mm,  $z = 50, 100$  mm, (b)  $r = 75$  mm,  $z = 50, 100$  mm, (c)  $r = 0$  mm,  $z = 200, 300$  mm, (d)  $r = 75$  mm,  $z = 200, 300$  mm. .... 56

FIGURE 3.15. Characteristic length scale of energy bump representing spectral energy injection by bubbles. .... 57

FIGURE 4.1. Induced liquid flow statistics in bubble plume, (a) averaged axial velocity, (b) averaged radial velocity, and (c) root-mean-square vertical fluctuation velocity, (d) root-mean-square radial fluctuation velocity and (e) root-mean-square radial and azimuthal fluctuation velocity normalized by the plume central velocity  $U_c$  and a half of the full width half maximum of  $U_z, r_{1/2}$ . .... 79

FIGURE 4.2. Scale comparison of  $A( \frac{U_z^2 + \overline{u'_z u'_z} - \overline{u'_r u'_r}}{U_c^2} )$  and  $B( \frac{U_r U_z + \overline{u'_r u'_z}}{U_c^2} ) \frac{L_z}{L_r}$  in the case of (a) conventional bubble plume and (b) churn-turbulent bubble plume. .... 80

FIGURE 4.3. In the case of the bubble plume, total liquid momentum parameter (  $M_t = \frac{U_z^2 + \overline{u'_z u'_z} - \overline{u'_r u'_r}}{U_c^2}$  ) as a function of (a) the interfacial momentum transfer parameter (  $I = \frac{\alpha}{(1-\alpha)} \frac{V_R^2 + V_R U_c}{U_c^2}$  ) and (b) the interfacial momentum transfer parameter weighted by the bubble Reynolds number, the bubble Weber number, the Reynolds number (based on the central velocity and the plume width) and the averaged volume void fraction. In (b), the solid line is  $M_t = 6.92(IRe_b^2 We_b^{-2} Re^{-0.6} \langle \alpha \rangle^{-2})^{0.34}$ . ..... 81

FIGURE 5.1. Stably stratified fluids mixing induced by (a) conventional bubble plume, and (b) churn-turbulent bubble plume when  $\Delta\rho/\rho_w = 0.016$ . ..... 90

FIGURE 5.2. Stably stratified fluids mixing induced by (a) conventional bubble plume, and (b) churn-turbulent bubble plume when  $\Delta\rho/\rho_w = 0.037$ . ..... 91

FIGURE 5.3. Stably stratified fluids mixing induced by (a) conventional bubble plume, and (b) churn-turbulent bubble plume when  $\Delta\rho/\rho_w = 0.068$ . ..... 92

FIGURE 5.4. Schematics of mixing type. (a) Falling type. (b) Peeling type. .... 93

FIGURE 5.5. Mixing type parameter depending on the density difference. .. ..... 94

FIGURE 5.6. Local mixing time contour for conventional bubble plume ((a), (b), and (c)) and churn-turbulent bubble plume (d), (e), and (f)). The density difference is (a), (d):  $\Delta\rho/\rho_w = 0.016$ , (b), (e):  $\Delta\rho/\rho_w = 0.037$ , and (c), (f):  $\Delta\rho/\rho_w = 0.067$ . ..... 95

FIGURE 5.7. Global mixing time variation with  $x$ . ..... 96

FIGURE 5.8. Mixing velocity variation with  $x$ . ..... 97

FIGURE 5.9. Global mixing time averaged inside the bubble plume with respect to difference difference. .... 98

- FIGURE 5.10. Mixing velocity averaged inside the bubble plume with respect to difference difference. .... 99
- FIGURE 5.11. Mixing velocity averaged inside the bubble plume scaled with the Froude number based on the liquid central velocity. .. 100
- FIGURE 5.12. Mixing velocity averaged inside the bubble plume scaled with the Froude number based on the interfacial momentum transfer parameter. .... 101
- FIGURE 7.1. In the case of the homogeneous bubble swarm (Lance & Bataille 1991; Martinez-Mercado *et al.* 2007; Riboux *et al.* 2010; Mendez-Diaz *et al.* 2013; Lee & Park 2020), variation of total liquid momentum parameter ( $\overline{u'_z u'_z} / V_b^2$ ) with (a) the interfacial momentum transfer parameter ( $I = \alpha / (1 - \alpha)$ ) and (b) the interfacial momentum transfer parameter weighted by the bubble Reynolds number and the bubble Weber number. In (b), the solid line is  $M_t = 2.74 \times 10^{-4} I Re_b^{1.4} We_b^{-0.6}$ . .... 119
- FIGURE 7.2. In the case of the rising bubbles under the prescribed grid turbulence (Lance & Bataille 1991; Alm eras *et al.* 2017), variation of total liquid momentum parameter ( $\overline{u'_z u'_z} / u_o'^2$ ) with the interfacial momentum transfer parameter ( $\frac{\alpha}{1 - \alpha} \frac{V_R^2}{u_o'^2}$ ). The solid line is  $M_t = 2.5 I^{0.7}$ . .... 120
- FIGURE 7.3. In the case of the laminar bubbly pipe flow (Hosokawa & Tomiyama 2013; Kim *et al.* 2016), total liquid momentum parameter ( $M_t = -r^{**} \Delta \tau (\rho_w U_c^2)$ ) as a function of (a) the interfacial momentum transfer parameter ( $I = \int_0^{r^*} \frac{\alpha}{1 - \alpha} \frac{V_R^2}{U_c^2} \frac{R}{d_b} r'^* dr'^*$ ) and (b) the interfacial momentum transfer parameter weighted by the bubble Reynolds number, the pipe Reynolds number (based on the bulk velocity and the pipe diameter), the averaged volume void fraction and the ratio of averaged bubble diameter to the pipe diameter. In (b), the solid line is  $M_t = 0.014 I Re b^{-0.6} Re^{1.8} \langle \alpha \rangle^{-0.4} (\langle \bar{d}_b \rangle / D)^4$ . .... 121
- FIGURE 7.4. In the case of the turbulent bubbly pipe flow (Shawkat *et al.* 2008; Lee *et al.* 2021), total liquid momentum parameter ( $M_t = -r^{**} \Delta \tau (\rho_w U_c^2)$ ) as a function of (a) the interfacial momentum transfer



# Nomenclature

## Roman symbols

$b$	the bubble parameter
$D$	the pipe diameter
$D_m$	plume characteristic length scale
$Eo$	Eötvös number
$f$	function
$H$	height of the stagnant water
$H_{low}$	height of the lower (heavier) layer
$L_l$	integral length-scale
$p$	pressure
$Q_b$	volume flow rate of gas
$Re$	Reynolds number
$r$	the cylindrical coordinate $r$ , radial-direction
$r_{1/2}$	a half of the full width at half maximum based on $U_z$
$t$	time
$T_I$	integral time scale
$u_i$	liquid velocity in $i$ -direction
$U_i$	the time-averaged liquid velocity in $i$ -direction
$U_c$	the time-averaged characteristic liquid velocity
$V_b$	the time-averaged vertical bubble velocity
$V_R$	the time-averaged relative velocity of a bubble
$V_{Ro}$	the reference bubble relative velocity
$v_i$	bubble velocity in $i$ -direction
$We$	Weber number
$z$	the cylindrical coordinate $z$ , axial-direction

## Greek Symbols

$\alpha$	local void fraction
$\alpha_e$	entrainment coefficient
$\delta$	bubble plume width
$\kappa$	local curvature of a bubble
$\mu$	dynamic viscosity
$\nu$	kinematic viscosity
$\rho$	density
$\sigma$	surface tension
$\tau$	total stress, $\tau = \tau_\mu + \tau_{uv}$
$\Phi$	interfacial momentum transfer term
$\phi$	sparger diameter
$\nabla$	spatial-gradient

## Superscripts

*	normalization
( )'	temporal fluctuation
( $\bar{\quad}$ )	time-averaged quantity

### Subscripts

<i>b</i>	bubble
<i>i</i>	inside of the bubble plume
<i>l</i>	liquid-phase
<i>o</i>	without bubbles
<i>rms</i>	root-mean-square
<i>w</i>	water
$\langle \ \rangle$	spatially-averaged quantity

### Abbreviations

B.P	bubble plume
FoV	field of view
LES	large eddy simulation
PDF	probability density function
TKE	turbulent kinetic energy

# Chapter 1

## Introduction

Fluid mixing induced by bubble plume is a commonly observed system in nature and industry, such as seawater and freshwater mixing, chemical reactors, oil mixing, natural gas seeps, underwater oil spill, and aeration tanks. Although a physical model based on systematic understanding is demand, because the problem is multi-phase (liquids and gas), multi-scale (from  $O(100 \text{ um})$  to  $O(1\text{km})$ ), and multi-physics (turbulence, chemical reaction, phase change, and heat transfer, etc) problems, it is extremely complex to characterize simple description. Therefore, usually, the system is greatly simplified and approximated with a simple model, or treated by case-by-case optimization with trial and error (Socolofsky *et al.* 2011; Boufadel *et al.* 2020; Ainsworth *et al.* 2021). In this paper, we established the parameter set and an analytical framework that govern the bubble plume through precise experiments and rigorous theoretical analysis for bubble plume and fluid mixing induced bubble plume, which has been approximated by the 1-D mixture model and analyzed only from the perspective of plume scale parameters. Based on this, we propose a physical scaling relation for fluid mixing induced by bubble plume.

### 1.1 Bubble plume

Bubble plumes are formed by bundles of bubbles applied locally to a stationary bath and are useful because they are easy to manufacture and cause fluid mixing very effectively (Lima Neto *et al.* 2016; Lai & Sokolofsky 2019; Boufadel *et al.* 2020). In particular, fluid mixing using bubble plume has a great advantage. It requires little maintenance cost compared to other fluid mixing techniques and can be effectively used for high viscosity fluids. Also, since it is a very general geometry, it can be said that a systematic study and a strict understanding of bubble plume are indispensable for an academic understanding of bubble-induced turbulence. Due to this necessity, research on bubble plume has been conducted since 50 years ago (Cederwall & Ditmars 1970), and simple theoretical techniques for this have already been systematically established and verified through several studies (Wüest *et al.* 1992; Bombardelli *et al.* 2007; Lai & Sokolofsky 2019). However, the turbulence characteristics are different. Compared to other types of bubbly flows, the turbulence characteristics and mixing of bubble plumes have not been understood much. The reason is that this system is more complicated than the homogeneous bubble swarm, and research results are insufficient compared to the bubbly pipe flow. In the previous study, the entrainment hypothesis was applied to the induced liquid plume induced by bubble plume as in the analysis of single-phase bubble plume, and only large-scale parameters of the plume scale such as plume mass flow rate and plume width were examined. In fact, bubble plume has not only agitation by bubble wake, but also collective behavior such as precession, meandering, and bulge of bubble plume itself. In particular, since fluid mixing is a phenomenon that includes a very small scale, fluid mixing induced by bubble

plume is a phenomenon that spans a very wide scale from a very small scale to a plume scale, and an experimental study is essential for correct understanding.

## **1.2 Stratified fluid mixing induced by bubble plume**

Stably stratified fluids are layers of heavy and light fluids, and there are many examples of stratified layers formed by temperature gradients in sea and lake, chemical reactors, and oil mixtures. In stably stratified fluids, the gravitational force acting on the fluid acts as a stabilizing effect, so spontaneous mixing, not caused by an external force, rarely occurs. In fact, studies on mixing stably stratified fluids using shear flow, vortex forcing, and buoyant plume have been studied experimentally and numerically (Strang & Fernando 2001; Olsthoorn & Dalziel 2015; Xue *et al.* 2019). Mixing stably stratified fluids using bubble plume is very widely used because it is very easy to construct and can produce efficient mixing at a low cost. However, there has been less systematic research on mixing by bubble plume because of the (1) difficulty in measurement (2) wide scale range (3) lack of information on bubble plume.

Therefore, in this study, we will develop and use a precise measurement technique to examine the turbulence of bubble plume in-depth and investigate mixing thoroughly.

## **1.3 Outline of the thesis**

Therefore, in this study, after developing and validating a technique to precisely measure the gas and liquid velocity fields of bubble plume (chapter 2), it is experimentally investigated that the bubble plume dynamics (chapter 3) and the stably stratified fluids mixing by bubble plume (chapter 5). Also, an analytical framework for characterizing bubble-induced turbulence is presented (chapter 4 and appendix), and a scaling relation for fluid mixing velocity is proposed based on this.

# Chapter 2

## Experimental methods

### 2.1 Bubble plume generation and the setup for optical measurement

#### 2.1.1 Facility and equipment

The experiment was carried out in a  $500 \times 500 \times 600$  mm<sup>3</sup> acrylic tank with tap water, as shown in [figure 2.1\(a\)](#). To generate bubble plume, bubbles were introduced through a single porous sparger (pore size of  $0.5 \mu\text{m}$ ) at the center of the bath bottom with an air (volume flow rate is fixed as 6 lpm) supply from the air compressor. Gas pressure was determined by a pressure regulator (SMC, IR1000-01BG) which has 0.2 Mpa as maximum pressure. Also, the flow rate was controlled by a needle valve and measured by a digital gas flow meter (SMC, PFM710S-C4-D) which has 10 lpm as maximum pressure. In addition, to protect the flow meter from the water invasion, an air filter (SMC, AF20-01B-A) was used.

To realize the different bubble size distribution, i.e., the typical quasi-Gaussian distributions with  $\langle \bar{d}_b \rangle = 4.64$  mm ( $\bar{d}_b = 1-10$  mm) and  $\langle \bar{d}_b \rangle = 7$  mm ( $\bar{d}_b = 1-20$  mm), two types of cylindrical spargers were used; one with a diameter of 24.5 mm and a height of 35 mm, and the other with a diameter of 12.7 mm and a height of 20 mm. With the same flow rate of air, as the sparger diameter decreases (increasing the superficial velocity of gas phase), it is found that the bubble plume transitions from conventional plume to the turbulent churn flow (Montoya *et al.* 2016) with a more enhanced (or irregular) bubble-bubble interaction and a wider bubble size distribution ([figure 2.1\(b\)](#)).

Gas-phase information was obtained from images taken in two types of field of view with a high-speed camera (Phantom MIRO M310). First, 20000 images were taken at 10 Hz in a 220 mm width, 350 mm height field of view to get information on large-scale bubble plume kinematics. In specially, two high-speed cameras were used to get a 3D information of the bubble plume motion. In addition, to obtain gas phase velocity field and bubble size distribution, 100,000 images were taken at 2000 Hz in a field of view of 200 mm in width and 130 mm in height.

The fluid mixing experiment was taken by two-color CCD camera (Vieworks, VH-4mc) with 8 Hz during  $60 \times 180$  sec depending on the density difference ([figure 2.4\(a\)](#)).

#### 2.1.2 Regime of bubble plume

As mentioned in section 2.1.1, with the smaller sparger at the same flow rate of 6 lpm, a bubble plume (with  $\bar{d}_b = 1-20$  mm) which has characteristics significantly different from that of the conventional bubble plume (with  $\bar{d}_b = 1-10$  mm) is formed. This bubble plume had very similar characteristics to chur-turbulent bubbly flow observed in bubble column or bubbly pipe flow. First, it has a much wider bubble size distribution than the conventional bubble plume, and accordingly,

the average bubble diameter increases. Also, the motion of the bubble plume becomes dynamic.

We named the bubble plume with more dynamic motion as a churn-turbulent bubble plume. In addition, conditions for churn-turbulent bubble plume transition were investigated and a regime map was drawn. In bubble column and bubbly pipe flow, churn-turbulent bubble plume transition is determined as a function of system size (i.e., bath size or pipe diameter) and gas superficial velocity. In an open system such as bubble plume, the system size is difficult to define. In place of this, we defined the confinement parameter and used it as a substitute. The mechanism of creation of the churn-turbulent regime has not been elucidated in detail, but according to our observations, it looks like that it is formed when more than a certain amount of gas is introduced within a certain space in the process of overcoming the pressure applied to the sparger. Therefore, the confinement parameter was defined as the square of the ratio of the height  $H$  representing the pressure of the stagnant water and  $D$ , which determines the spatial scale in which the gas is injected. In addition, gas superficial velocity is normalized as system

Froude number which has the definition of  $Fr_{sys} = \sqrt{\frac{\rho_w V_c^2}{\Delta\rho g a}} \approx \sqrt{\frac{Q_b^2}{g a^5}}$  where,  $a$  is

the square root of the outer area of the sparger. In [figure 2.2](#), the conditions describing the transition between the conventional and the churn-turbulent bubble plume are represented by a dashed straight line. The left side of the line corresponds to the conventional bubble plume and the other side is the churn-turbulent bubble plume. The condition we chose was designated by arrows in the regime

## 2.2 Stably stratified fluids mixing induced by bubble plume

### 2.2.1 Stably stratified fluids

Stably stratified fluids were developed in the following way (Lima Neto *et al.* 2016). First, make heavier fluid and put a porous filter on it ([figure 2.3\(a\)](#)). Feeding lighter fluids over a porous filter at a sufficiently slow flow rate can create stably stratified fluids with distinct boundaries ([figure 2.3\(b\)](#)). In order to confirm the stability of the formed fluid layer, the fluid layer was observed 3 days after the fluid layer was formed. As shown in [figure 2.3\(c\)](#), it can be seen that there is no significant difference except that the interface is slightly blurred.

For heavier fluid, sodium acetate ( $\text{CH}_3\text{COONa}$ ) aqueous solution was used. According to Craig 2004, bubble coalescence inhibition occurs depending on the combination of ions that make up the aqueous solution (see [table 2.1](#)). Therefore, to avoid this, sodium acetate, a combination marked with a cross, was used. The experiment was carried out at a water temperature of 15 degrees Celcius, and the density difference was carried out at  $\Delta\rho/\rho_w = 0.016, 0.037, \text{ and } 0.068$ . Here,  $\Delta\rho$  is the difference in density between heavy and light fluids, and  $\rho_w$  is the density of water. To track the heavier fluid, it was colored with food dye which has sufficiently small diffusivity (Landeau *et al.* 2014).

### 2.2.2 Optical setup for mixing experiment

Stably stratified fluids mixing experiment was carried in same acrylic tank

described in section 2.1 with two color CCD camera and two tungsten lamps (figure 2.4(a)). The height of the lower layer with heavier fluids ( $H_{low}$ ) was half of the entire fluid height (i.e., tank height). The image was taken with 8Hz until the fluids are sufficiently mixed (typically, during 60 ~ 180 sec) with 5 times for each case. The field of view covered  $(r,z) = (-215 \sim 215, 0 \sim 430)$ . When calculating the mean and standard deviation of the parameters, the results obtained from each of the two cameras were considered together to have a sufficient number of samples. Moreover, we assumed that the system is statistically in symmetry based on the center of the bubble plume. After all, a total of 20 samples were obtained for each case.

## 2.3 Image post-processing algorithm: shadowgraph technique

To obtain gas-phase information, a shadowgraph technique consisting of tungsten lamps and high-speed camera was used. The bubble size, bubble velocity, and volume void fraction were obtained by applying binarization, watershed transform, and Lucas-Kanade algorithm to images taken from two large and small fields of view. In this section, the algorithms to evaluate bubble plume kinematics parameters and the bubble size going to be dealt with.

### 2.3.1 Definition of parameters to characterize bubble plume kinematics

It is well known that bubble plume has characteristic motions such as precession, meandering, and bulge (Seol *et al.* 2009; Simiano *et al.* 2009). The characteristic of these movements is that they are not individual bubble motions, but collective motions that take place at the entire bubble plume scale. In order to quantify this, the boundary of the bubble plume was traced in this study. Of course, it would be best to get information by tracking all the individual bubbles constituting the bubble plume, but a method for tracking individual bubbles in the high volume void fraction system as discussed in this study has not been developed until now. Therefore, as an alternative, the temporal behavior of bubble plumes was examined.

To tracing the bubble plume boundary, binarization was first performed. Binarization was performed in the most basic way of making 0 and 1 based on the threshold. The boundary of the bubble plume was determined in the following way. First, the plume center of each height is determined by weighting 0 and 1 of each position to the horizontal coordinates at each height and the average of it. After that, the standard deviation is calculated by the same weighting, and the left and right boundaries are determined by three times the standard deviation around the center. An example of the bubble plume center and boundary determined in this way is shown in figure 2.5(a).

Bubble plume kinematics parameters defined as follows were obtained from the determined bubble plume boundary and the center (figure 2.5(b)). Here,  $X_c(z)$ ,  $W(z)$  is the time-averaged plume center and the width, respectively. Also,  $x_c(t,z)$ ,  $w(t,z)$  is the instantaneous center and width. In addition, we defined the instantaneous tilted plume center,  $X_{tc}(t,z)$ , which is used for the definition of precession amplitude. It is defined as the center of the linearly approximated trace of the instantaneous

boundary. Precession amplitude, meandering amplitude, and bulge amplitude are defined as follows:

$$x_{pc}(t, z) = X_{ic}(t, z) - X_c(z) \quad (2.1)$$

$$x'_m(t, z) = x_c(t, z) - X_{ic}(t, z) \quad (2.2)$$

$$w'_x(t, z) = w_x(t, z) - W_x(t, z) \quad (2.3)$$

The precession amplitude represents the distance between the tilted center and the time-averaged plume center. Also, the meandering amplitude corresponds to the difference between the instantaneous center and the tilted center which means that it is an amplitude of the instantaneous distortion. Finally, the bulge amplitude is the instantaneous width fluctuation. About the bubble plume kinematics, because we took images with two cameras, we can have the following parameters including 3D information of the bubble plume motion. Here, 'y' designate the horizontal axis of the perpendicular camera. We named the each parameter as precession radius, meandering radius, and bulge length.

$$r_{pc}(t, z) = \sqrt{x_{pc}^{\prime 2}(t, z) + y_{pc}^{\prime 2}(t, z)} \quad (2.4)$$

$$r_m(t, z) = \sqrt{x_m^{\prime 2}(t, z) + y_m^{\prime 2}(t, z)} \quad (2.5)$$

$$w'(t, z) = \text{sign}(w'_x(t, z) \cdot w'_y(t, z)) \cdot |w'_x(t, z) \cdot w'_y(t, z)| \quad (2.6)$$

### 2.3.2 Watershed transform for discrimination of overlapped bubbles

To estimate the bubble size distribution from the images taken at the larger field of view (200 mm in width and 130 mm in height), the watershed transform was used. At first, based on the roundness, the single (a non-overlapped bubble) bubble was filtered. Here, the roundness is defined as the region area divided by  $4\pi$  times of the perimeter, and 0.7 was used as the threshold value. Next, the watershed transform was operated on the remained blobs. The watershed transformation separates the blob based on its gray values. It finds a midway between the peak (or the valley) of the blob (Lee & Park 2020). The most important part of the watershed transform is finding the peak (so-called maxima or minima). Within the blob area, we used binarization for finding maxima with the otsu method (Otsu 1979). In addition, based on the spatial size of the maxima, the falsely detected maxima was filtered out (the threshold was an area of  $0.5 \text{ mm}^2$ ).

The discrimination result of overlapped bubbles by the method described above are shown in figures 2.6-2.7. The part marked with cyan is the area recognized as a bubble in binarization, and the discriminated bubble is represented by being separated by a gray line. First, it can be seen that both the conventional bubble plume and the churn-turbulent bubble plume are discriminated well even though there are some errors. However, in the case of churn-turbulent bubble plume, sometimes small bubbles are distributed over the large bubbles, then the blob is split based on the image, but large bubbles are hidden behind the separated small bubbles. Therefore, it is possible that the number of large bubbles was collected

somewhat less in the size distribution of churn-turbulent bubble plume.

## 2.4 Optical flow algorithm to evaluate the gas phase velocity field

In particular, in the case of bubble velocity, there were too many bubbles to apply conventional particle tracking velocimetry (PTV), so individual particle tracking was not able to be performed, and the Lucas-Kanade method, which is a kind of optical flow algorithm that calculates velocity from gray value gradients, was used and validation for this was performed. The volume void fraction was determined by applying the relationship between the bubble velocity and the volume void fraction to the bubble velocity thus obtained.

### 2.4.1 Lucas-Kanade method

The Lucas-Kanade method is a well-known optical flow algorithm. It is established based on very simple assumptions.  $I(x,y,t)$  is a gray value at the position  $(x,y)$  at time  $t$ . If the point moves with a velocity  $(w_x, w_y)$ , by the first-order Taylor expansion,

$$I(x + \delta x, y + \delta y, t + \delta t) = I(x, y, t) + \frac{\partial I}{\partial x} \delta x + \frac{\partial I}{\partial y} \delta y + \frac{\partial I}{\partial t} \delta t, \quad (2.7)$$

$$-\frac{\partial I}{\partial t} = \frac{\partial I}{\partial x} w_x + \frac{\partial I}{\partial y} w_y. \quad (2.8)$$

Let  $L_w$  is the length of the square window which is a spatial unit that has the same velocity. Then, each pixel  $p_i$ , satisfies the following equation.

$$-\left. \frac{\partial I}{\partial t} \right|_{q_i} = \left. \frac{\partial I}{\partial x} \right|_{q_i} w_x + \left. \frac{\partial I}{\partial y} \right|_{q_i} w_y \quad (2.9)$$

If there are  $N$  pixels in the window, then we have

$$\begin{bmatrix} I_x(q_1) & I_y(q_1) \\ \vdots & \vdots \\ I_x(q_N) & I_x(q_N) \end{bmatrix} \begin{pmatrix} w_x & w_y \end{pmatrix} = \begin{bmatrix} -I_t(q_1) \\ \vdots \\ -I_t(q_N) \end{bmatrix}. \quad (2.10)$$

Therefore,

$$\begin{pmatrix} w_x & w_y \end{pmatrix} = \begin{bmatrix} I_x(q_1) & I_y(q_1) \\ \vdots & \vdots \\ I_x(q_N) & I_x(q_N) \end{bmatrix}^{-1} \begin{bmatrix} -I_t(q_1) \\ \vdots \\ -I_t(q_N) \end{bmatrix}. \quad (2.11)$$

We evaluated the bubble velocity field by applying the above equation to the bubble shadow image. Before the vector evaluation, the gray value of the position which is not corresponding to the bubble area set to be zero to exclude the

background effect. Also, after vector evaluation, vectors at the background area were filtered out.

## 2.4.2 Validation of the technique

PTV results and LK (the Lucas-Kanade method) results are shown in [figure 2.9](#) for bubbles rising around the wall for validation of the velocity field obtained by the method described above. The air bubble rises by periodically colliding with the wall as shown in [Figure 2.9\(c\)](#). It can be seen that the PTV and LK results agree well. Both  $v_x$  and  $v_y$  had distinct periods, which were confirmed to agree well in both methods. Time-averaged horizontal velocity differed by 3%, and time-averaged vertical velocity differed by 10%.

## 2.5 Laser doppler anemometry (LDA)

### 2.5.1 LDA measurement condition

We used the one-dimensional laser-Doppler anemometry (LDA) (Dantec Dynamics, 1D FiberFlow) to measure the liquid-phase velocity induced by the bubbles, with hollow glass tracer particles (mean diameter of 10  $\mu\text{m}$ ). To achieve the statistical convergence of the velocity data, at each measurement position, the signal was obtained for 5 minutes at the data rate of 200-850 Hz. The beam diameter of the laser was 1.35 mm, and the sensor gain was set to be 8 dB, by which the signal-to-noise ratio and the first to second peak ratio was set to be 5 dB and 8:1, respectively, to minimize the effect of noise owing to the presence of bubbles. The actual measurements were done at  $r = 0, 10, 20, 30, 40, 50, 60, 75, 90, 150$  mm with  $z = 30, 50, 100, 200, 300$  mm, determined to cover the spatially evolving characteristics of bubble plume. Also, in the case of the churn-turbulent bubble plume, points at  $r = 5, 15$  mm were added at  $z = 30, 50$  mm. Here, we used a cylindrical coordinate which has its origin at the center of the sparger top area.

### 2.5.2 LDA post-processing algorithms

Velocity data measured by LDA needs to be compensated because fast-moving fluid elements are over-collected (Damaschke *et al.* 2018). In this study, first, second, and third moments were calculated using transit time (or, residence time) as a weighting factor as commonly used (Damaschke *et al.* 2018). Transit time is the time spent by particles crossing the measurement volume. In addition, the autocorrelation function was determined by the slotting method (Damaschke *et al.* 2018), from which the Taylor microscale and Kolmogorov time scale were obtained. The energy spectrum of the vertical liquid velocity fluctuation was obtained by direct fourier transformation (Velte *et al.* 2014).

## 2.6 Post-processing on color image to characterize the fluid mixing

The images taken with a color CCD camera of fluid mixing are as shown in [figures 5.1-5.3](#). The image (blue channel gray values extracted from the RGB image) was divided into several panels with equal intervals of 10 mm from the left boundary to the right boundary. The intensity information of each panel is averaged inside the panel in the horizontal direction for each time step. For each horizontal

position, when the averaged intensity at each time step is stacked, it becomes a z-t contour as shown in [figure 2.10\(a\)](#). The contour in [figure 2.10\(a\)](#) was normalized because of the influence of the inhomogeneity of background illumination. At first, during the experiment, after the mixing is completed, the bubble injection is stopped and about 50 images are taken. Normalization is performed using the average value of the last 50 images as a reference. Since mixing has already been completed, this reference value should have a uniform value for the height ( $z$ ). In fact, due to inhomogeneous background illumination, the center tends to be bright and the periphery is dark. At each time step, by dividing the reference intensity, the contour without the background illumination effect is obtained as shown in [figure 2.10\(b\)](#).

In [figure 2.10\(b\)](#), two boundaries are observed around  $t = 0$  (one is upward and the other is downward). Here,  $t = 0$  corresponds to the moment when the bubble plume first touches the liquid interface. The upward slope corresponds to peeling, and the downward slope corresponds to the sinking of the upper and lower liquid layer boundaries. We defined this slope ( $dH_{low}/dt$ ) as  $u_{low}$ .

TABLE 2.1. Ion combination table. Tick: a combination that cause bubble coalescence inhibition. Cross: a combination without coalescence inhibition (the table is taken from Craig 2004).

Anions	Cations	H <sup>+</sup>	Li <sup>+</sup>	Na <sup>+</sup>	K <sup>+</sup>	Cs <sup>+</sup>	Mg <sup>2+</sup>	Ca <sup>2+</sup>	NH <sub>4</sub> <sup>+</sup>	(CH <sub>3</sub> ) <sub>4</sub> N <sup>+</sup>	(CH <sub>3</sub> ) <sub>3</sub> NH <sup>+</sup>	(CH <sub>3</sub> ) <sub>2</sub> NH <sub>2</sub>	(CH <sub>3</sub> )NH <sub>3</sub> <sup>+</sup>
Type	Type												
OH <sup>-</sup>	$\alpha$	$\times$	$\alpha$	$\checkmark$	$\alpha$	$\checkmark$		$\alpha$	$\alpha$	$\beta$	$\beta$	$\beta$	$\beta$
Cl <sup>-</sup>	$\alpha$	$\times$	$\checkmark$	$\checkmark$	$\checkmark$		$\checkmark$	$\checkmark$		$\times$	$\times$	$\times$	$\times$
Br <sup>-</sup>	$\alpha$	$\times$		$\checkmark$	$\checkmark$	$\checkmark$							
NO <sub>3</sub> <sup>-</sup>	$\alpha$	$\times$	$\checkmark$	$\checkmark$	$\checkmark$			$\checkmark$					
ClO <sub>3</sub> <sup>-</sup>	$\beta$			$\times$									
ClO <sub>4</sub> <sup>-</sup>	$\beta$	$\checkmark$		$\times$			$\times$		$\times$				
CH <sub>3</sub> COO <sup>-</sup>	$\beta$	$\checkmark$		$\times$	$\times$	$\times$	$\times$		$\times$	$\checkmark$			
SO <sub>4</sub> <sup>2-</sup>	$\alpha$	$\times$	$\checkmark$	$\checkmark$			$\checkmark$						
(COO) <sub>2</sub> <sup>2-</sup>	$\alpha$	$\times$			$\checkmark$								

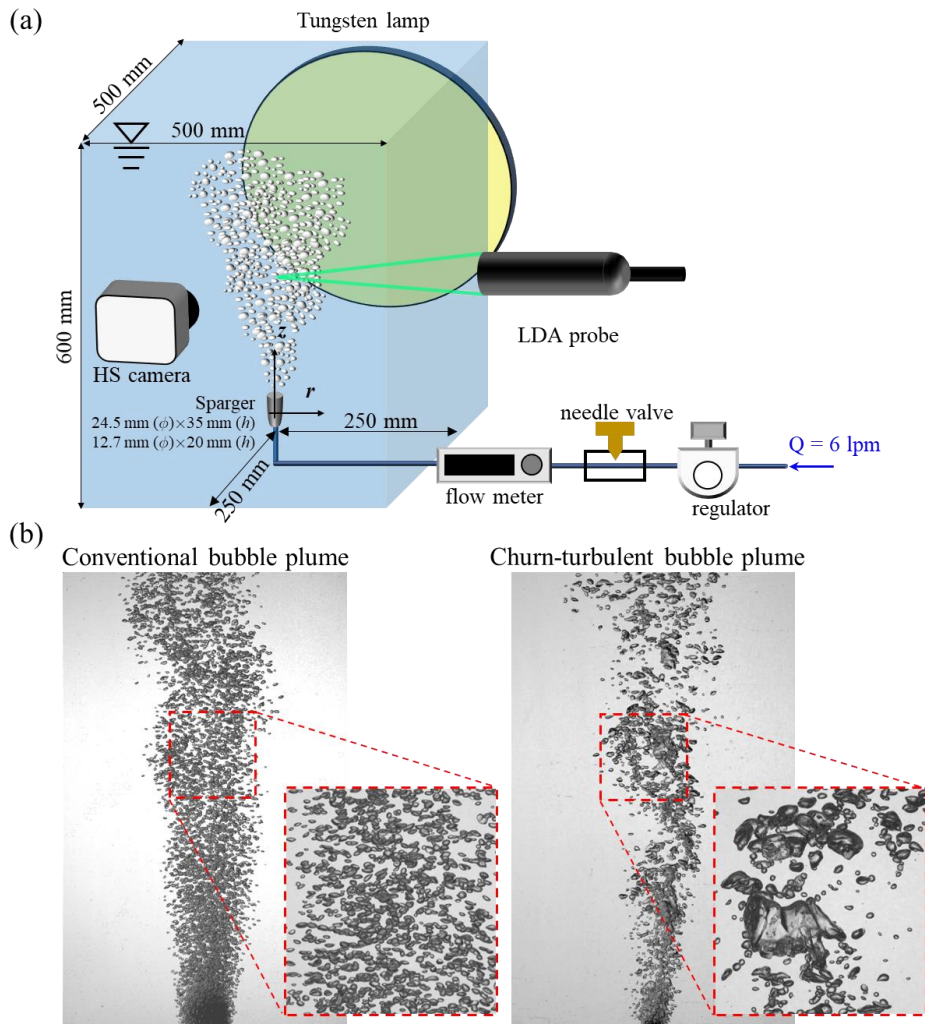


FIGURE 2.1. (a) Schematic of the experimental setup for bubble plume measurement. Bubble plume kinematics and the bubble velocity is taken by high speed camera (b) Typical images for the conventional and churn-turbulent bubble plume. Inset shows the enlarged view.

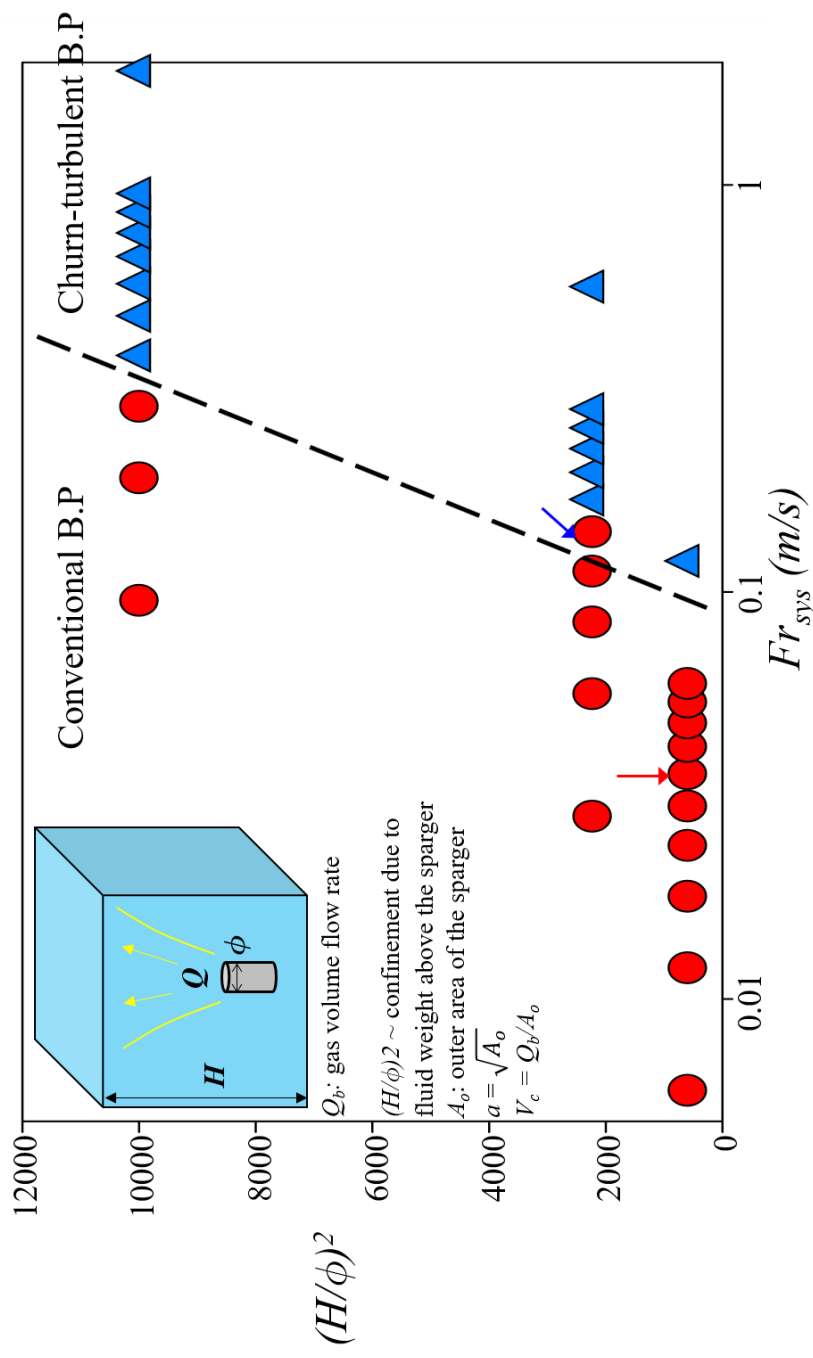


FIGURE 2.2. A regime map of bubble plume. The left side of the dashed line corresponds to conventional bubble plume and the other side is churn-turbulent bubble plume.

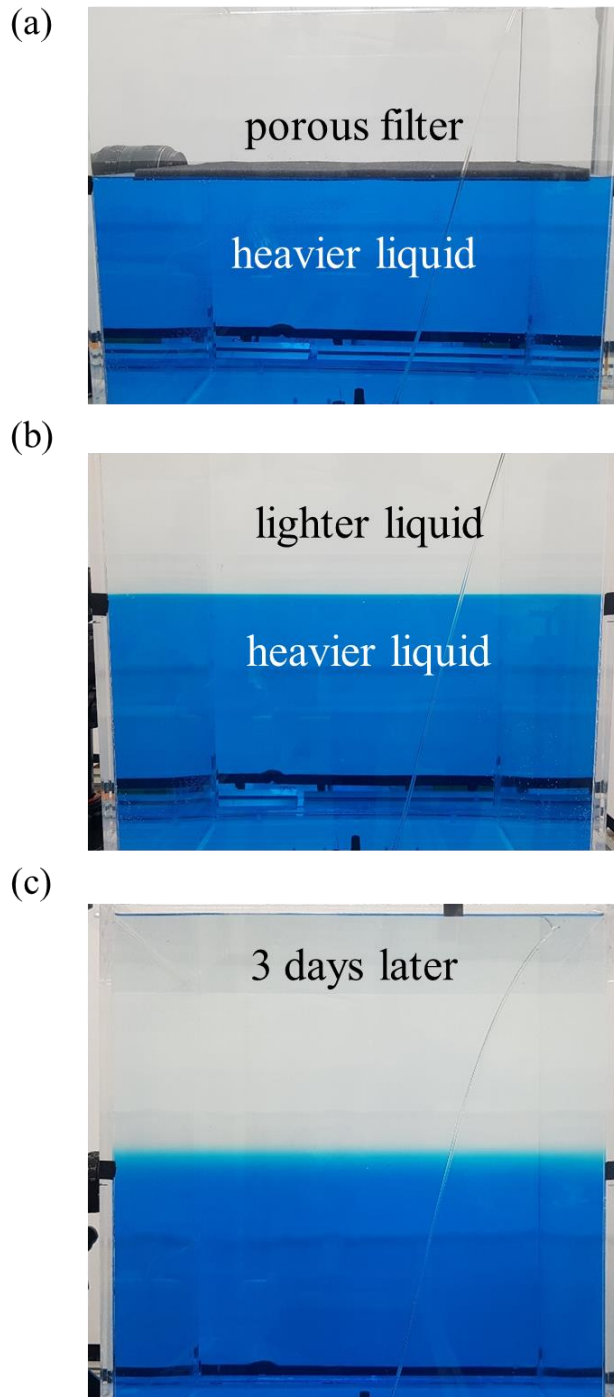


FIGURE 2.3. Process to make the stably stratified fluids (a) the lower liquid with porous filter (b) the stably stratified fluids (c) the stably stratified liquids 3 hours after first made.

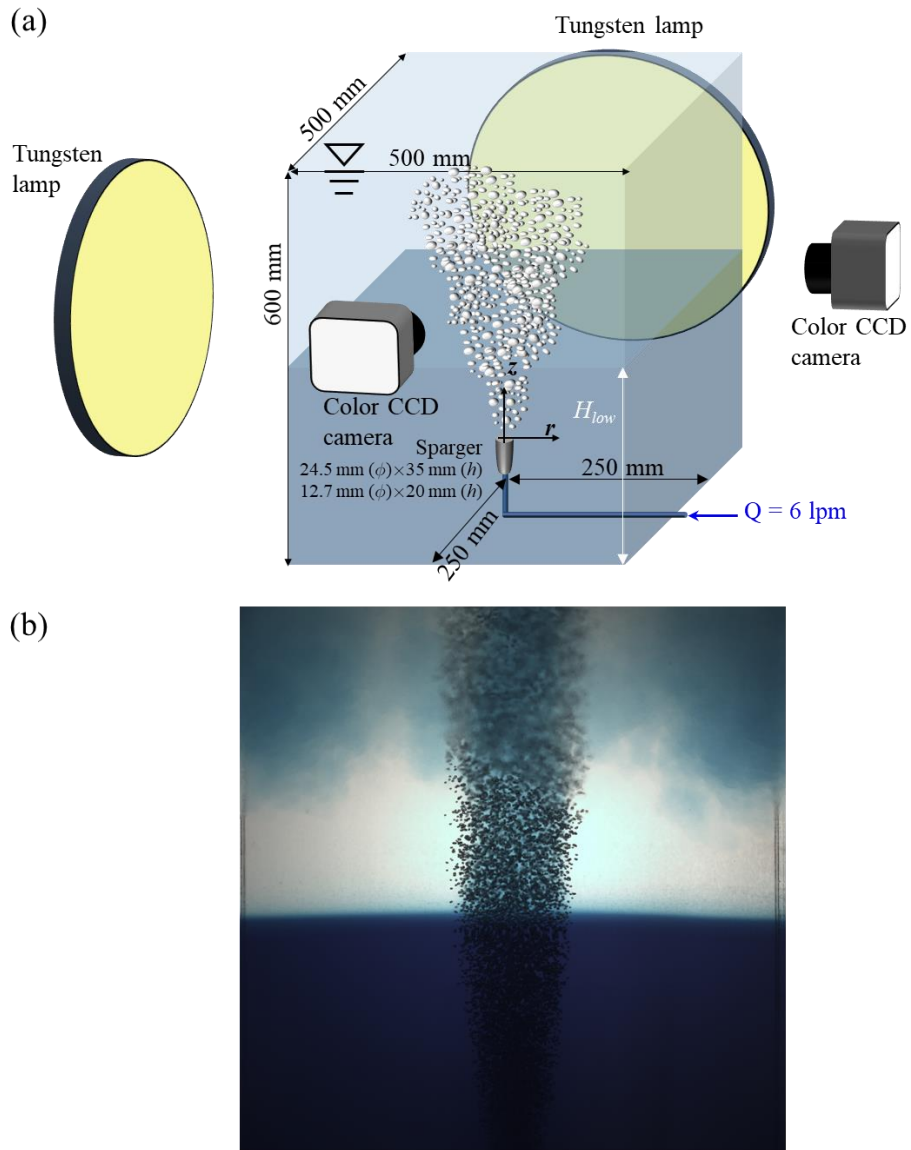


FIGURE 2.4. (a) Schematic of the experimental setup for fluid mixing induced by bubble plume with two color CCD camera (b) An example of the image ( $\Delta\rho/\rho_w=0.016$ ).

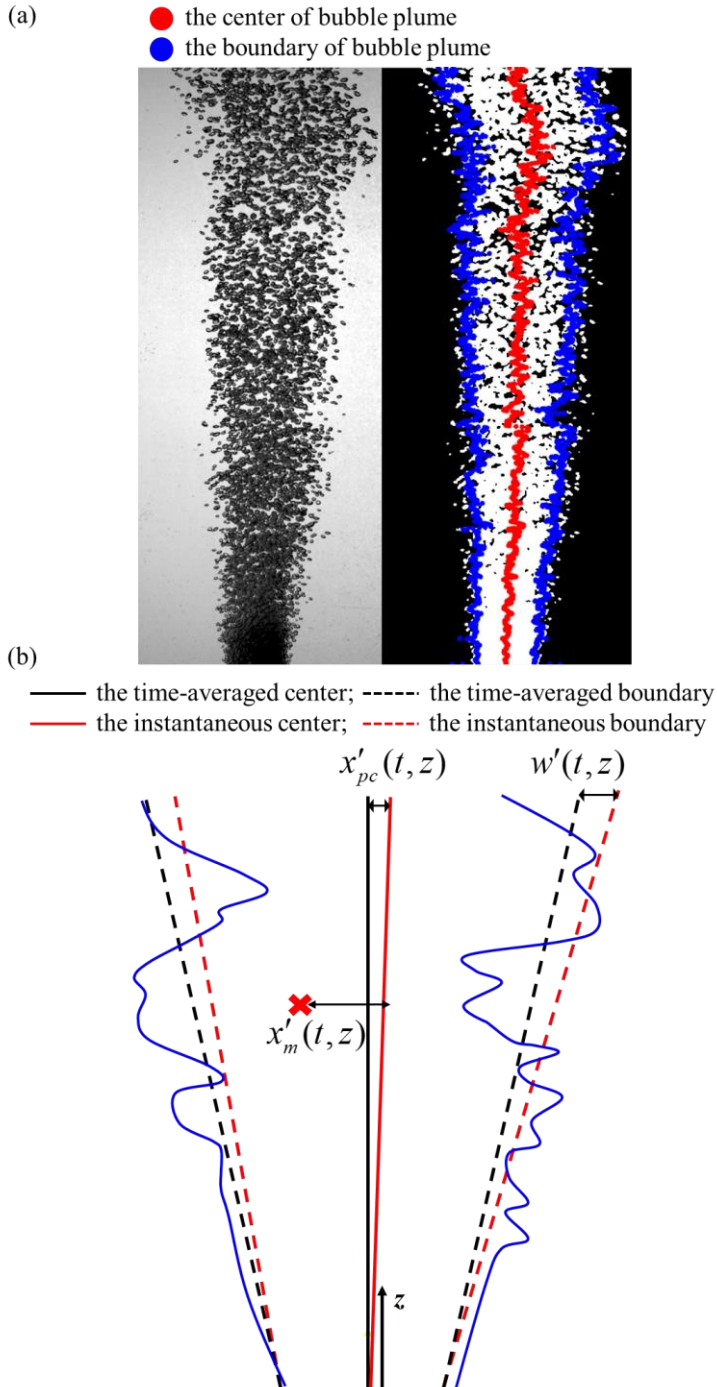


FIGURE 2.5. Parameterization of bubble plume kinematics (a) Raw image (b) binarized image with the center and the boundary (c) A schematic on the definition of parameters describing bubble plume kinematics.

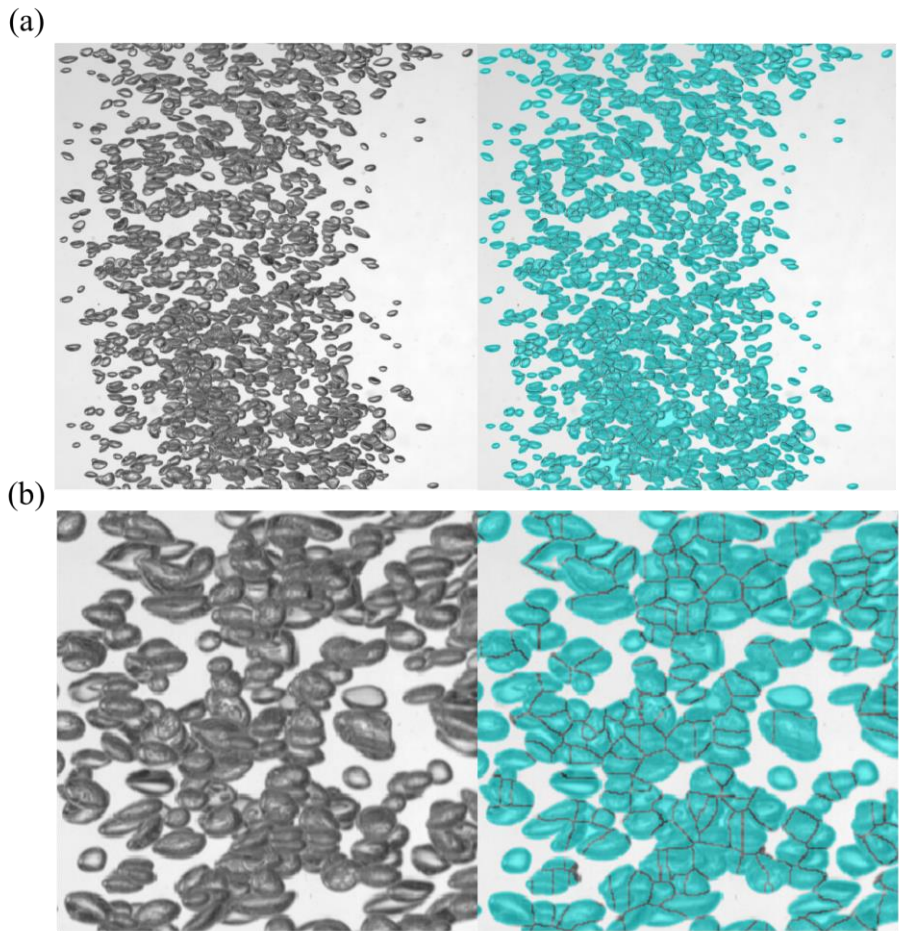


FIGURE 2.6. An example of watershed transform to discriminate overlapped bubbles in conventional bubble plume. Left: Raw image, right: processed result at (a) original image scale (b) enlarged image

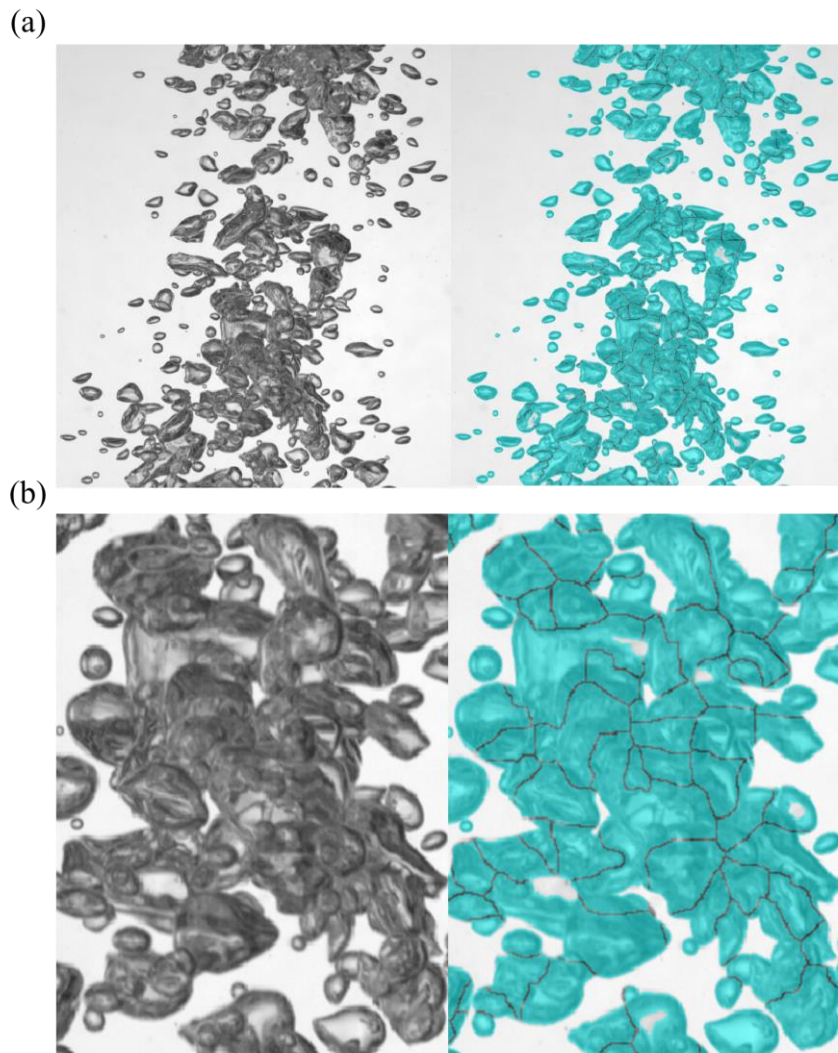


FIGURE 2.7. An example of watershed transform to discriminate overlapped bubbles in churn-turbulent bubble plume. Left: Raw image, right: processed result at (a) original image scale (b) enlarged image

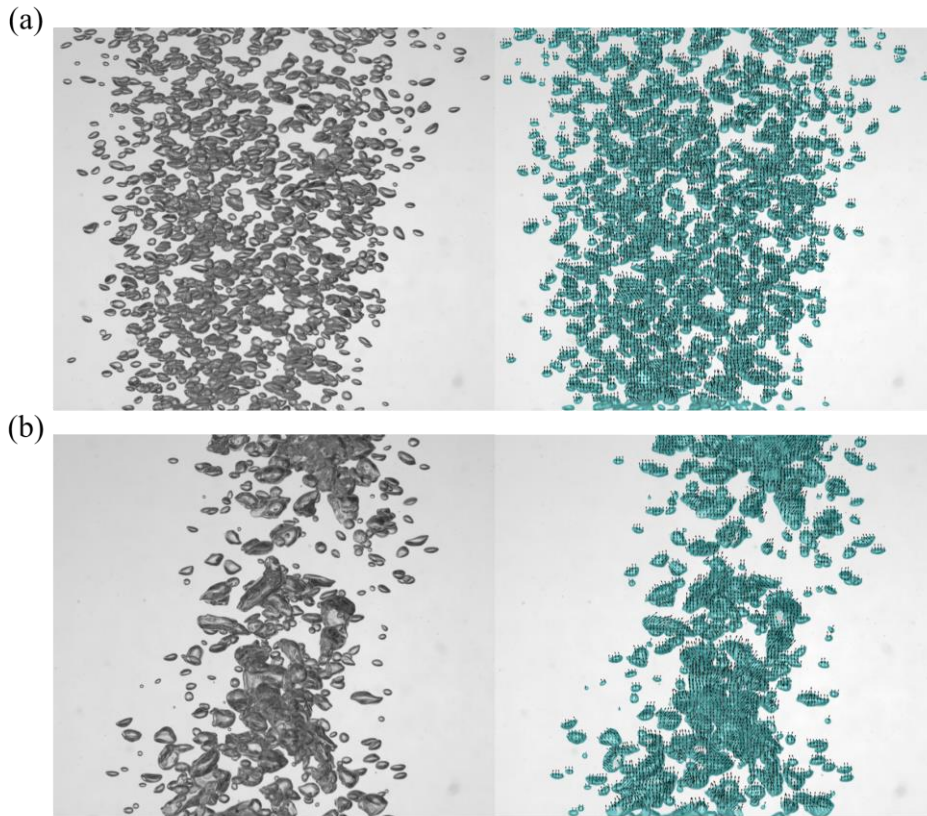


FIGURE 2.8. An example of Lucas-Kanade method for (a) conventional bubble plume (b) churn-turbulent bubble plume

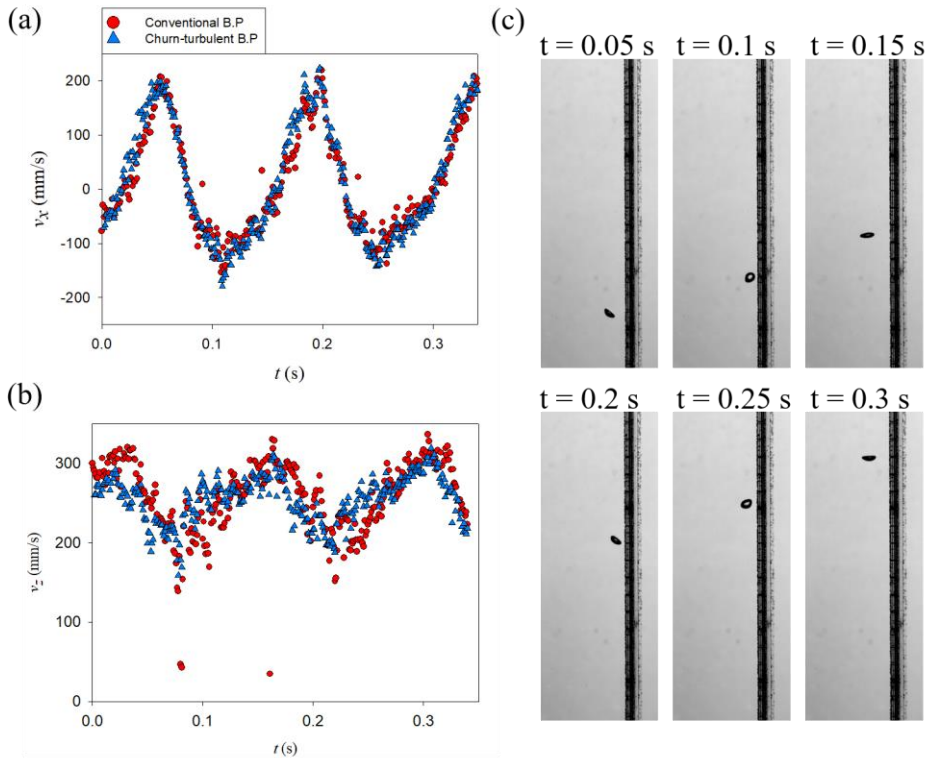


FIGURE 2.9. Validation of Lucas-Kanade method with single bubble rising near the wall. Temporal variation of (a) horizontal velocity (b) vertical velocity. (c) Raw image.

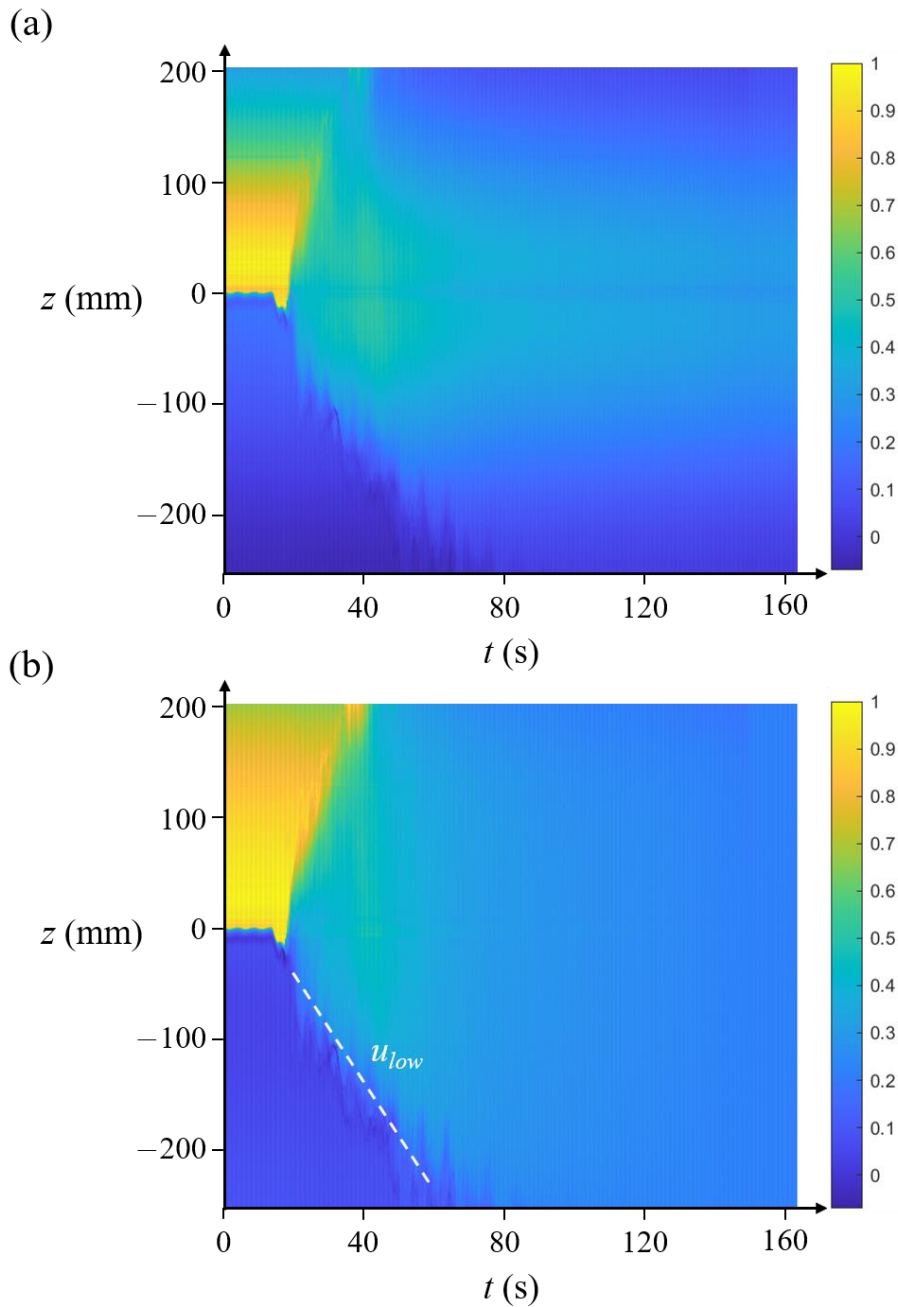


FIGURE 2.10.  $z$ - $t$  contour of B channel image taken at  $x = 200$  mm for conventional bubble plume with  $\Delta\rho/\rho_w = 0.068$ . (a) Before and (b) after the normalization. In (b), the dashed line corresponds to the velocity of the density front descent of lower layer.

# Chapter 3

## Bubble plume dynamics

### 3.1 Background

About bubble plume dynamics, previous studies have mainly concentrated on conventional bubble plumes (Fanneløp & Sjoen 1980; Milgram 1983; Wüest *et al.* 1992; Bombardelli *et al.* 2007; Fraga & Stoesser 2016; Lai & Sokolofsky 2019; Wang *et al.* 2019; Li *et al.* 2020), and in the case of the churn-turbulent bubble plume, the formation conditions were only dealt (Hur *et al.* 2013), and no studies on dynamics have been performed in detail. On the other hand, the exploration of the churn-turbulent regime in bubbly flow has been mainly made in bubbly pipe flow (Schlegel *et al.* 2013; Zhou *et al.* 2016; Li *et al.* 2018) and bubble column (Nedeltchev & Shaikh 2013; Montoya *et al.* 2016). The reason is that, as mentioned in section 2.1.2, the confinement effect is important in the transition to the churn-turbulent regime. Because the confinement effect is greater in the closed system by walls such as bubble column and bubbly pipe flow than in the opened system such as bubble plume so, transition to churn-turbulent regime easily occurs in bubble column and bubbly pipe flow.

On the conventional bubble plume, the result from the time-averaged mixture (drift-flux) model equation was widely used to characterize the large-scale feature of bubble plume (ex. time-averaged vertical velocity at the center and radius of the induced liquid plume). It starts from the time-averaged mixture (drift-flux) model equation (Ishii & Hibiki 2011).

$$\rho_w (\overline{u_m} \cdot \nabla) \overline{u_m} + \nabla \overline{p} = \nabla \cdot \left( \mu (\nabla \overline{u_m} + \nabla^T \overline{u_m}) \right) + \alpha (\rho_w - \rho_b) g \hat{z} \quad (3.1)$$

Here,  $u_m$  is the mixture velocity. When normalize it with bubble relative velocity and volume flow rate of gas,  $Q_b$  and take the vertical component of the equation:

$$\left( \overline{u_{m,z}^*} \cdot \nabla^* \right) \overline{u_{m,z}^*} + \frac{\partial \overline{p}^*}{\partial z^*} = \nabla^* \cdot \left( \frac{1}{Re} \left( \nabla^* \overline{u_{m,z}^*} + \nabla^{*T} \overline{u_{m,z}^*} \right) \right) + \alpha \left( 1 - \frac{\rho_b}{\rho_w} \right) \frac{g Q_b}{V_R^3 L} \quad (3.2)$$

If we assume that the effect of pressure gradient with high-Reynolds number condition, following scaling relation satisfies.

$$\left( \frac{U_m}{V_R} \right)^2 \sim \frac{g Q_b}{V_R^3 L} \quad (3.3)$$

Also, for air-water mixture, mixture parameters almost the same as the parameter of water, therefore,

$$\left(\frac{U_z}{V_R}\right)^2 \sim \frac{gQ_b}{V_R^3 L}. \quad (3.4)$$

Also, under the assumption that  $U_z \sim V_R$ , the characteristic length scale  $L$  satisfies that

$$L \sim \frac{gQ_b}{V_R^3}. \quad (3.5)$$

When equation (3.5) is combined with entrainment hypothesis, the characteristic length scale  $D_m$  comes out.

$$D_m = \frac{gQ_b}{4\pi\alpha_{th}^2 V_R^3}. \quad (3.6)$$

In the previous studies, experimental results of the bubble plume are mainly dealt in terms of scaling relation between normalized central velocity  $U_c/V_R$  and plume radius  $r_{1/2}/D_m$  as a function of  $z/D_m$  (Bombardelli *et al.* 2007; Lai & Sokolofsky 2019). Indeed, the scaling relation has shown relatively satisfactory accuracy (figure 3.8). However, since this equation (3.6) is for a mixture plume, it eventually becomes a scaling relation for liquid parameters, gas-phase phenomena such as bubble plume kinematics have not been verified. In addition,  $D_m$ , by definition, reflects information on bubble plume as an entrainment coefficient, bubble relative velocity, and volume flow rate. Since the entrainment coefficient and bubble relative velocity are mainly assumed to be constant, it is determined only as a function of volume flow rate and  $Q_b$ . However, this does not provide information on the difference between the conventional bubble plume and the churn-turbulent bubble plume, nor does it provide information on the amount of turbulence. Therefore, based on the various data obtained in this study, we verify the usefulness and limitations of the characteristic length scale  $D_m$ .

In bubble plume, the study of liquid phase velocity field mainly focuses on the average velocity and width, and there have been some studies on the amount of turbulence (Bryant *et al.* 2009, Simiano *et al.* 2009; Li *et al.* 2020), but all of them are limited to the small volume void fraction. However, considering various instability such as bubble plume kinematics, a study on the situation of high volume void fraction is necessary. Therefore, in this study, quantitative analysis of bubble plume unsteady characteristics, such as bubble plume kinematics, turbulence statistics, etc. is performed in consideration of the high volume void fraction situation.

The topic covered in this chapter is as follows.

- (1) Effectiveness of scaling with  $D_m$ ,  $r_{1/2}$  and  $U_c$
- (2) Bubble plume kinematics and bubble velocity field
- (3) Quantitative and detailed understanding of the induced liquid turbulence
- (4) Integrated mass and momentum flow rate
- (5) Scale distribution of turbulence energy in bubble plume

## 3.2 Regimes of bubble plume

As mentioned in section 2.1.2, the present study examines two different types of bubble plumes, conventional bubble plume, and churn-turbulent bubble plume. Conventional bubble plume is mainly composed of bubbles having a size of 3-5 mm and shows relatively stable bubble plume movement. On the other hand, the churn-turbulent bubble plume has a much wider size distribution than the conventional bubble plume (figure 3.1(a)) and shows a dynamic bubble plume motion. In addition, vigorous breakup and coalescence of large air bubbles ( $\sim O(10$  mm)) are observed.

The bubble size distribution of the bubble plume covered in this study is shown in figure 3.1(b). Here, since the number of large bubbles has a large volume at least and the effect on the flow can be large, the PDF was defined by using the volume of each bubble as a weighting factor. The specific definition is as follows. First, a PDF is obtained by counting the number of bubbles corresponding to each size as a general definition. After that, each frequency was multiplied by  $\Omega_i/\Omega$  with

$\Omega = \sum_{i=1}^{N_b} \Omega_i$ . The definition of  $\Omega_i$  is the volume of the  $i$ -th bubble size in the PDF,

i.e.,  $\Omega_i = \pi d_i^3/6$  ( $d_i$ : the size of the  $i$ -th bubble size in the PDF domain). From figure 3.1(b), it can be seen that the churn-turbulent bubble plume has a much wider size distribution than the conventional bubble plume, and even contains  $O(10$  mm) bubbles. The median diameter was 3.35 mm for the conventional bubble plume and 6.26 mm for the churn-turbulent bubble plume.

## 3.3 Gas-phase flow dynamics

The driving source of the bubble plume is the buoyancy applied to the gas phase, and the buoyancy applied to the bubble is transferred to the liquid through interfacial momentum transfer to developing the bubble plume. Therefore, as mentioned in section 3.1, scaling with large scale parameters derived from the equation that the buoyancy is scaled with the averaged momentum using the 1-D mixture model has been useful in the meantime. However, as shown in section 3.4, such scaling with large scale parameters was insufficient to explain the difference in turbulence statistics. Therefore, in this study, we distinguish gas-phase and liquid-phase and examines the interaction between the two phases. First, in this section, we will look at the kinematics and dynamics of gas-phase. The gas-phase flow dynamics of bubble plume can be seen in two aspects: the average velocity of individual bubbles and the bubble plume kinematics generated by the collective behavior of the bundle of bubble. In the following part, bubble plume kinematics is examined first, followed by a time-averaged velocity field of the gas phase.

### 3.3.1 Bubble plume kinematics

Bubble plume kinematics were classified into precession, meandering, and bulge. First, the precession, meandering radius, and bulge length at each height over time were plotted as contours (figure 3.2). All parameters had high values in churn-turbulent bubble plume, and it was confirmed that the tendency was changed around 100 mm in height. In closer examination, it was confirmed that the precession radius increased noticeably after 100 mm, but the difference was more pronounced in the conventional bubble plume. On the other hand, the meandering

radius and bulge length showed more distinct differences in the churn-turbulent bubble plume with  $z = 100$  mm. In addition, a structure propagating downstream from the meandering radius and bulge length was observed. The propagation velocity was 23.5 cm/s, which is much slower than the bubble velocity ( $\sim 0.6$ - $0.7$  m/s) (see [figure 3.5](#)). In other words, meandering and bulge can be said to propagate downstream at a slower rate (23.5 cm/s) than the rising rate of individual bubbles. In the case of bulge length, a positive value (red color) indicates swelling of the bubble plume, and a negative number (blue color) indicates contraction. In the case of conventional bubble plume, the frequency of contraction is high, whereas, in the case of churn-turbulent bubble plume, the frequency of swelling is high. As for the duration of the structure, it can also be seen that the precession has a much longer time (order of several seconds) than that of meandering and bulge.

[Figure 3.3](#) shows the time-averaged plume width, and root-mean-square bulge length, precession radius, and meandering radius. Here, the rms parameters are named bulge amplitude, precession amplitude, and meandering amplitude, respectively. Conventional bubble plume has a much larger time-averaged plume width than churn-turbulent bubble plume, but root-mean-square parameters do not. Specifically, the conventional bubble plume had a larger value before 100 mm in height, but the churn-turbulent bubble plume had a higher value after 100 mm. However, at this time, the precession amplitude was consistently higher in the churn-turbulent bubble plume. As mentioned in [section 3.1](#), it appears to be divided into an adjustment region and an asymptotic region, and it can be seen that the criterion is around  $D_m$  ( $\sim 150$ - $200$  mm). Therefore, the parameters were examined by normalizing the vertical coordinates to  $D_m$  ([figure 3.4](#)). Here, the characteristic length scale in the radial direction was  $r_{1/2}$ , which is the characteristic length scale of the liquid velocity. Surprisingly, the adjustment region and the asymptotic region were distinguished based on  $z = D_m$  for all parameters. Normalized time-averaged width, bulge amplitude, precession amplitude, and meandering amplitude all showed a tendency to converge after  $z = D_m$ . In particular, in the case of churn-turbulent bubble plume, the change in the adjustment region was very remarkable. However, the normalized precession amplitude of the conventional bubble plume did not change significantly according to the height, which means that the precession amplitude of the conventional bubble plume occupies a constant ratio of 20-30% of  $r_{1/2}$  at all heights. Overall, bubble plume kinematics are divided into an adjustment region and an asymptotic region based on  $z = D_m$ . In the asymptotic region, they converge to have a constant ratio for the induced liquid plume radius ( $2r_{1/2}$ ), and in the adjustment region, the ratio was first high, and decrease with increasing height. In particular, this trend was remarkably observed in churn-turbulent bubble plume. The discussion of the existing adjustment region was limited to liquid statistics, but it can be seen that the same discussion can be extended to the bubble kinematics parameters. In addition, the typical adjustment region refers to the region that converges regardless of the initial condition. About that, it is shown that the convergence values of the churn-turbulent bubble plume and the conventional bubble plume are different.

### 3.3.2 Time-averaged flow field of the gas phase

The gas-phase velocity fields are drawn in [figure 3.1](#). First, the center value of the bubble relative velocity, which is the momentum source of the induced liquid

plume, is plotted against the height. Here, bubble relative rise velocity,  $V_R = V_b - U_z$ .  $V_b$  is the time-averaged bubble rise velocity, and  $U_z$  is the time-averaged liquid vertical velocity.  $V_{Rc}$  is  $V_R$  at the center of the plume. Like the bubble plume kinematics parameters,  $V_{Rc}$  also showed a tendency to converge toward  $z = D_m$ . Next, look at the radial distribution of time-averaged bubble velocity and relative velocity. the bubble velocity has a high value near the center and a bell-shape that decreases toward the edge. Overall, it tends to increase as the height increases, and it tends to converge around  $z = 200 - 300$  mm. And the conventional bubble plume showed a faster trend.

In the case of a bubble plume, because the bubble rises in a background induced plume flow, bubble relative velocity defined as bubble velocity subtracted by time-averaged liquid velocity. Bubble relative velocity has a low value in the vicinity of the center and increases toward the edge, because the volume void fraction in the central area is high, and the hindrance effect by bubbles is strong. Bubble relative velocity tended to converge more clearly as the height increased. In addition, since the relative velocity near the edge hardly changed with respect to the height, the average of these was defined as the reference relative velocity  $V_{Ro}$  (table 3.1). Interestingly, it can be seen that at low heights, the relative velocity may be very small or even negative, which does not mean that the bubble is actually slower than the surrounding liquid flow when moving. When defining the bubble relative velocity, it was defined as the difference between the time-averaged bubble velocity and the liquid velocity. In order to accurately determine whether the bubble is faster or slower than the surrounding flow, conditionally average and compare only the moment when the bubble passes. However, due to the limitation of the technique of this study, the relative velocity could not be obtained with such a definition, so it was substituted and used as the difference between time-averaged velocities. Of course, not only this study, but also many previous studies use the same definition of relative velocity, and it has been confirmed that the trend is similar (Simiano *et al.* 2009).

## 3.4 Liquid phase flow dynamics

### 3.4.1 Time-averaged flow field of the liquid phase

In this section, the liquid velocity field measured through LDA is elaborated. Figure 3.6 shows the time-averaged axial velocity and turbulence kinetic energy contour. The averaged axial velocity contours from both bubble plumes show a very similar trend, whereas the turbulence kinetic energy shows a very different trend. In particular, the difference between the two bubble plumes is remarkable after passing around  $z = 100$  mm. The conventional bubble plume has an off-axis peak from  $z = 100$  mm and the TKE is greatly reduced, whereas the churn-turbulent bubble plume maintains the central peak and has a higher value than the conventional bubble plume. In other words, it means that the two bubble plumes have a similar average flow and at the same time show a significant difference in the turbulence.

The radial profiles of the liquid velocity statistics corresponding to each height are going to be investigated in detail. First, the average behavior of induced liquid plume can be depicted through time-averaged axial velocity (figure 3.7(a)) and radial velocity (figure 3.7(b)). First, as previously reported (Lai & Sokolofsky

2019), time-averaged axial velocity is nicely scaled with central velocity  $U_c$  and half of the full width half maximum of  $U_z$ ,  $r_{1/2}$ . Here,  $U_z(r_{1/2}) = 0.5U_c$ , usually, plume radius is defined as  $2r_{1/2}$  (Lai & Sokolofsky 2019).  $U_z$  of all heights collapse into one profile, and interestingly, they overlap well with the profile of the single-phase jet. On the other hand, the radial profile showed a different tendency according to the height, and showed a significant difference from the single-phase jet. Since the single-phase jet is a momentum driven flow, the radial velocity near the center has a positive value and as it goes to the plume edge, a negative radial velocity (a trace of the entrainment) appears. On the other hand, the bubble plume has a negative value in an entire section other than the center. This reveals the characteristics of the bubble plume very well. The momentum source of the bubble plume is the buoyancy applied to the bubble, and the mass flow of the induced liquid plume caused by the bubble is totally originated from the surrounding liquid. Therefore, a strong negative radial velocity is inevitable at the starting point of the bubble plume. This is expressed schematically in figure 3.7(c).

The analysis result of the 1-D mixture model is represented by scaling of  $U_c$  and  $r_{1/2}$  to  $z/D_m$  (figure 3.8). The solid line shown together in each graph is the one proposed by Bombardelli *et al.* (2007) according to the 1-D mixture model and presented with a slight modification by Lai & Sokolofsky (2019). It can be seen that the experimental results of this study also well follow the suggested relational equation according to the previous data. However, the conventional bubble plume result has a slightly different slope from the previous result, which is also observed in the entrainment coefficient.  $\alpha_{th}$  is the entrainment coefficient assuming the top-hat profile and is twice the square root of the entrainment coefficient of the gaussian profile, which is close to the actual axial velocity profile. The entrainment coefficient of the conventional bubble plume was 0.06, and the churn-turbulent bubble plume was 0.82 (Table 3.1). Surprisingly, the entrainment coefficient of churn-turbulent bubble plume, rather than the conventional bubble plume, was very close to the previously reported value of 0.083. For this reason, rather, the results of churn-turbulent bubble plume showed a similar tendency to those previously reported. Why does the churn-turbulent bubble plume have a value similar to that of the previously studied bubble plumes? For now, a possible answer is that since the conventional bubble plume examined in this study is a much higher volume void fraction (or, superficial velocity) than the system examined in the previous studies, the entrainment coefficient seems to have changed due to its influence. As is well known, the entrainment coefficient is influenced by the turbulent structure of the flow, and the turbulent structure in the bubbly flow is highly dependent on the volume void fraction (or, superficial velocity).

For the results of this study, the axial variation of the central velocity, radius, and turbulence kinetic energy at the center is shown in figure 3.9. First, the slopes of figures 3.9(a) and (b) that churn-turbulent bubble plume has a large entrainment coefficient. In addition, since the churn-turbulent bubble plume has a larger entrainment coefficient, it can be speculated that the churn-turbulent bubble plume may have a wider width than the conventional bubble plume if it goes further downstream than the currently observed position. On the other hand, through figure 3.9(c), the normalized turbulence kinetic energy of the liquid phase is also well divided between the adjustment region and the establishment region according to  $z/D_m$ . In addition, as in the case of precession, meandering, and bulge amplitude in

bubble plume kinematics, the convergence value of normalized turbulence kinetic energy in churn-turbulent bubble plume had a larger value.

### 3.4.2 Turbulence statistics of the liquid phase

The turbulence statistics of the induced liquid plume are shown in [figure 3.10](#). For root-mean-square (rms) fluctuation velocity, vertical velocity was greater than radial velocity, and churn-turbulent bubble plume had a higher value than conventional bubble plume at all heights and radial positions. At rms vertical fluctuation velocity, the conventional bubble plume had an off-axis peak from  $z = 100$  mm, while the churn-turbulent bubble plume had a central peak except for the highest position. At the highest position,  $z = 300$  mm, the flat profile is shown near the center. In addition, as the height increased, both bubble plumes showed a convergent profile. Particularly interestingly, the convergence profile of the conventional bubble plume almost coincided with that of the single-phase jet. Radial fluctuation velocity was observed to have a central peak at a low height in the case of a conventional bubble plume and a flat profile near the center as the height increases. The churn-turbulent bubble plume showed central peaks at all heights as well as the rms vertical fluctuation velocity. In the case of the rms radial fluctuation velocity, the conventional bubble plume showed a convergence profile similar to that of the single-phase jet.

The gaussianity of fluctuation velocity can be determined through skewness ([figure 3.10\(c\)](#)) and flatness ([figure 3.10\(d\)](#)), which are the third and fourth-order moments of vertical fluctuation velocity. First, skewness was mostly positive skewness in both bubble plumes. If positive skewness is explained in terms of velocity fluctuation PDF, the maximum value is located in the negative fluctuation, but the high fluctuation velocity is more distributed in the positive value. This is in good agreement with the previously reported features of the PDF of bubble-induced turbulence (Riboux *et al.* 2010; Risso 2018; Lai & Sokolofsky 2019). In the vicinity of the plume edge, there is a difference between the two bubble plumes. The conventional bubble plume increases gradually like a single-phase flow jet (solid line) and has a large positive value, whereas the churn-turbulent bubble plume decreases toward the edge. It shows a value close to gaussian. Flatness represents the amount of non-gaussian tail, and the larger the flatness, the greater the portion of the fluctuation velocity having extreme values, and in this case, high intermittency is often accompanied (Davidson 2015). When the height is low, a fairly high flatness is observed near the center. Conventional bubble plume shows a flatness profile that converges from  $z = 100$  mm and churn-turbulent bubble plume from  $z = 200$  mm. It showed a high value of 20. This is consistent with the single-phase jet results.

### 3.4.3 Characteristic time scales of the bubble-induced turbulence

The characteristic time scales for turbulent flow are shown in [figure 3.11](#). When the height is low, the integral time scale, Taylor microscale, and Kolmogorov time scale all have low values, and the overall scale increases as the flow develops as the height increases, and this tendency is more pronounced than the integral time scale. Based on the measurement result at the highest position, the integral time scale had

a peak around  $r = r_{1/2}$  in both bubble plumes, which is different from the single-phase jet result (Pope 2000) whose integral scale increases as it approaches the edge. No distinct difference was observed between the conventional bubble plume and the churn-turbulent bubble plume.

### 3.4.4 Averaged mass and momentum flow rates of the liquid phase

The induced liquid mass flow rate in bubble plume has the following definition.

$$\dot{m} = 2\pi \int_0^{2r_{1/2}} (1-\alpha) U_z^2 r dr \quad (3.7)$$

$$\dot{M}_{total} = 2\pi \int_0^{2r_{1/2}} (1-\alpha) \left( U_z^2 + \overline{u'_z u'_z} - \overline{u'_r u'_r} \right) r dr \quad (3.8)$$

Here, the momentum flow rate is defined from equations (4.22)-(4.23) and is consistent with the definition of momentum flow rate considering turbulence in a single-phase jet or buoyant plume. The above equation (3.8) can be divided into mean momentum flow rate and turbulence momentum flow rate as follows.

$$\dot{M}_{mean} = 2\pi \int_0^{2r_{1/2}} (1-\alpha) U_z^2 r dr \quad (3.9)$$

$$\dot{M}_{turb} = 2\pi \int_0^{2r_{1/2}} (1-\alpha) \left( \overline{u'_z u'_z} - \overline{u'_r u'_r} \right) r dr \quad (3.10)$$

First, in both the mass flow rate, total momentum flow rate, and mean momentum flow rate, the conventional bubble plume had a high value, and the turbulence momentum flow rate had a value comparable to that of the conventional bubble plume and churn-turbulent bubble plume. However, at the highest height, the conventional bubble plume had a somewhat higher value. Therefore, at low height, the turbulence momentum flow rate to mean momentum flow rate ratio showed a high value for churn-turbulent bubble plume, but the difference decreases as the height increases. It showed a similar value of about 20%. Since the same flow rate is injected into the conventional bubble plume and the churn-turbulent bubble plume, the buoyancy flux applied by gravity is the same as  $gQ_b$ . In this situation, the mass and momentum flow rates that occur in the induced liquid plume differ, which means that the interfacial momentum transfer between the gas phase and the liquid phase varies according to the bubble plume type. In the case of churn-turbulent bubble plume, the amount of temporally fluctuating components is larger than that of the conventional bubble plume. In the case of the single-phase jet, the total momentum flow rate is constant in the axial direction, it increases continuously in the bubble plume because, unlike the single-phase jet, the induced liquid plume induced by the bubble plume has the momentum source (buoyancy).

### 3.4.5 Turbulence energy spectra

The velocity spectrum is shown in figure 3.13 to examine the scalewise energy distribution of the vertical fluctuation velocity. First, at  $r = 75$  mm near the plume edge, the overlapping spectrum was shown regardless of the type and height of the

bubble plume. This means that there is little difference between the bubble plume type and the scalewise energy distribution according to the height. On the other hand, there was a clear difference near the center. First, at the height  $z = 50$  mm, the two bubble plumes have a similar energy spectrum. When  $z = 100$  mm, energy bumps were observed around  $f = 10$  Hz in churn-turbulent bubble plumes, unlike conventional bubble plumes. This is not observed with conventional single-phase liquid jets. In the existing bubble swarm studies, it has been reported that spectral energy injection by bubbles is performed at a scale smaller than the integral scale and forms a local bump (Prakash *et al.* 2016). In churn-turbulent bubble plume, turbulence energy injection by bubble is observed at a lower height than conventional bubble plume. When the height reaches 200 mm, energy bumps are observed in both bubble plumes, and it is observed that the position moves toward the large scale as the height increases. In addition, it can be seen that the energy bump of the conventional bubble plume is generated on a larger scale.

Looking at the spectrum normalized with the integral time scale, it can be seen that the energy bump is located near  $fT_I \sim 1$ . In other words, spectral energy injection by air bubbles occurs at a frequency corresponding to the integral time scale, and this is expressed as a length scale as shown in figure 3.15. Conventionally, in the bubble swarm, energy bumps have been reported to appear at a scale similar to the bubble diameter. However, in this study, it can be seen that the bubble plume is observed at a plume radius ( $2r_{1/2}$ ) or a longer scale belonging to a much larger scale.

### 3.5 Concluding remarks

In this chapter, two types of bubble plumes (conventional and churn-turbulent bubble plumes) have been examined in detail in terms of bubble plume kinematics, gas-phase velocity fields, and liquid phase dynamics. Previous studies on have been conducted on the relation between characteristic length scale  $D_m$ , central velocity,  $U_c$ , half of the induced liquid plume radius,  $r_{1/2}$  based on the 1-D mixture model. We have checked whether these characteristic scales can be applied to other parameters as well as the plume scale parameters of the induced liquid plume that have been previously dealt with.

First to the best of our knowledge, it was confirmed that bubble plume kinematics were quantified for the first time, and the parameters normalized to  $r_{1/2}$  showed a tendency to converge according to  $z/D_m$ . In other words, the region previously referred to as the adjustment region is defined as  $z < D_m$ . In this region, the bubble plume kinematics parameters have a larger value than  $r_{1/2}$ , whereas as they enter the asymptotic region after  $z = D_m$ , It was observed to have a converged value. In addition, at this time, it was quantitatively confirmed that the convergence value was larger in the churn-turbulent bubble plume, that is, more dynamic bubble plume kinematics were shown.

Similarly, by examining the normalized turbulence energy of the center in addition to the scaling on the central velocity or radius that has been done for the induced liquid plume, it was confirmed that the turbulence amount can also be classified into an adjustment and asymptotic region based on  $z = D_m$ .

By resolving the inside of the induced liquid plume, the average velocity and radial distribution of turbulence statistics were confirmed. Through this, it was confirmed that the various physical quantities of the induced liquid plume of the

conventional bubble plume were quite similar to that of the single phase jet, and the churn-turbulent bubble plume had a consistently higher rms fluctuation velocity than the conventional bubble plume.

In addition, the mass flow rate and momentum flow rate of the induced liquid plume were examined, and it was confirmed that the churn-turbulent bubble plume had a particularly high relative turbulence momentum flow rate.

Finally, by examining the energy spectrum of the vertical fluctuation velocity, the scale-wise turbulence energy distribution of the two bubble plumes was confirmed. As previously reported, energy bumps, which are traces of spectral energy injection by the bubble, exist in the bubble plume. It was confirmed that it occurs. Since  $u_{\text{rms},c}T_1 \sim O(r_{1/2})$ , unlike the bubble swarm, energy injection occurred at the plume scale, not the bubble size, in the bubble plume.

Despite the aforementioned usefulness, it was difficult to scale detailed turbulence statistics with only  $U_c$ ,  $r_{1/2}$ , and  $D_m$ . In the following chapter 4, a useful theoretical framework will be presented.

TABLE 3.1. Reference parameters to describe the bubble plume based on 1-D plume model

	Conventional bubble plume	Churn-turbulent bubble plume
$\alpha_{th}$	0.06	0.082
$V_{Ro}$ (m/s)	0.47	0.41
$D_m$ (m)	0.20	0.17

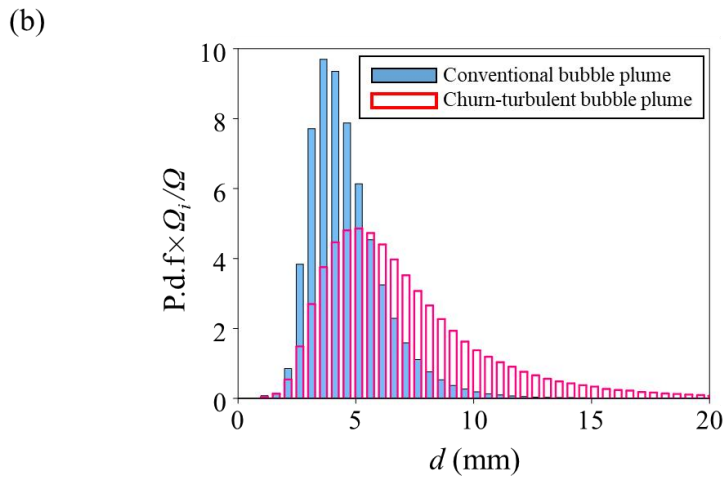
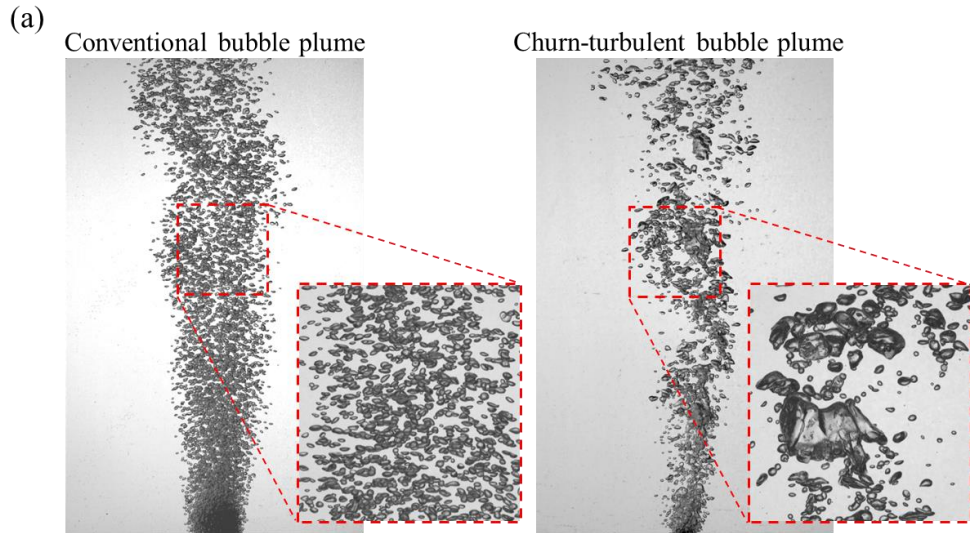


FIGURE 3.1. (a) A snapshot of the conventional (left) and the churn-turbulent (right) bubble plume.  $d_{50} = 3.35$  mm (conventional bubble plume) and 6.26 mm (churn-turbulent bubble plume). (b) The probability density function of the bubble diameter weighted by its volume.

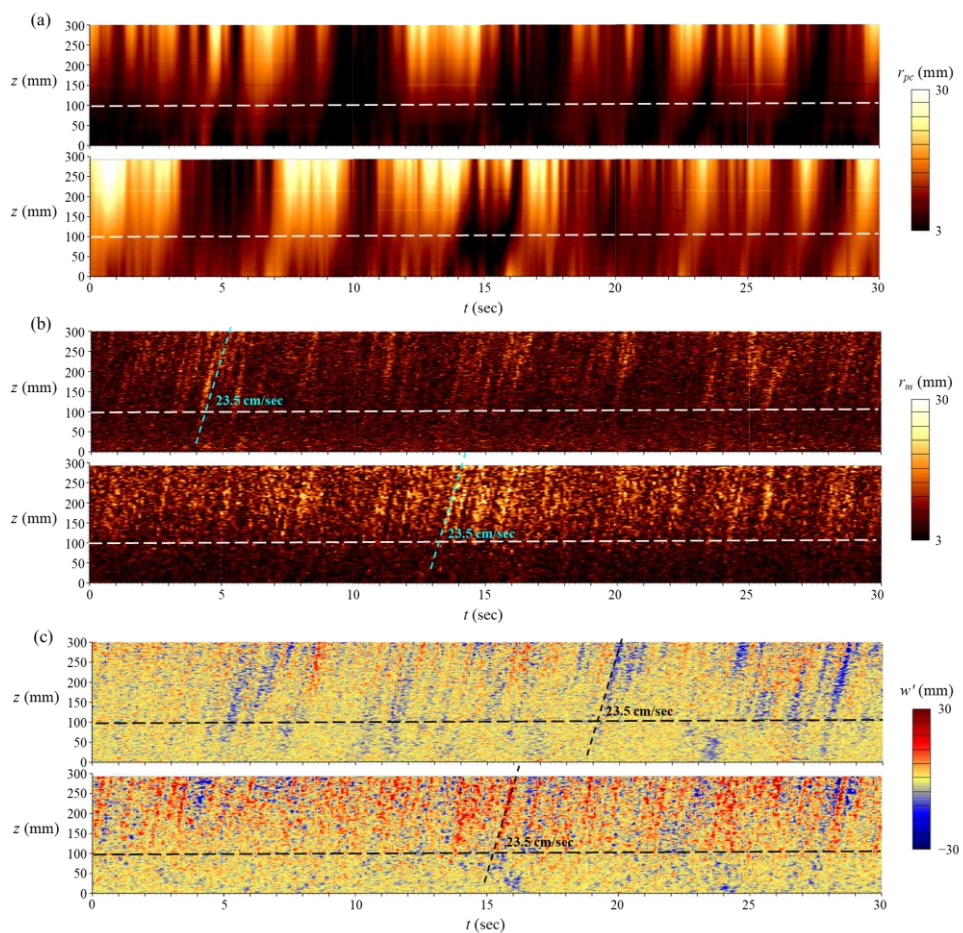


FIGURE 3.2. Temporal structures observed in bubble plume kinematics. (a) Precession radius, (b) meandering radius, and (c) bulge length.

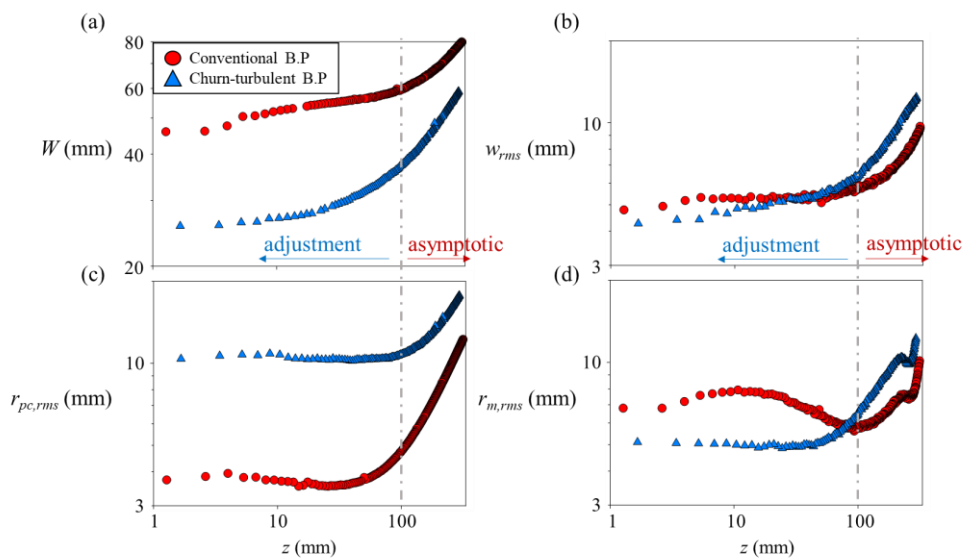


FIGURE 3.3. Time averaged parameters on bubble plume kinematics. (a) Time averaged plume width, (b) bulge amplitude, (c) precession amplitude, and (d) meandering amplitude.

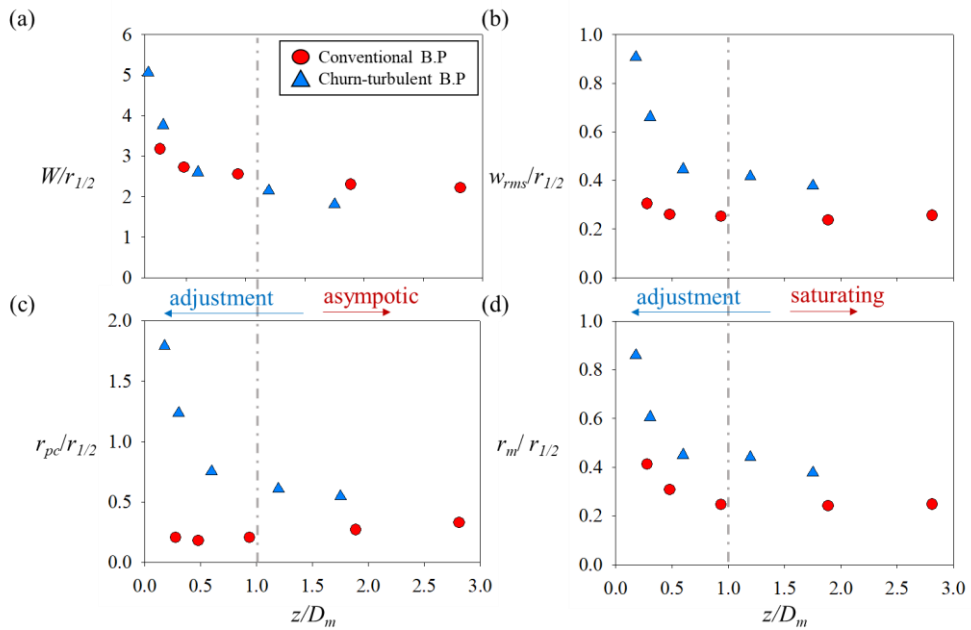


FIGURE 3.4. Time averaged parameters on bubble plume kinematics normalized by  $r_{1/2}$ . (a) Time-averaged plume width, (b) bulge amplitude, (c) precession amplitude, and (d) meandering amplitude

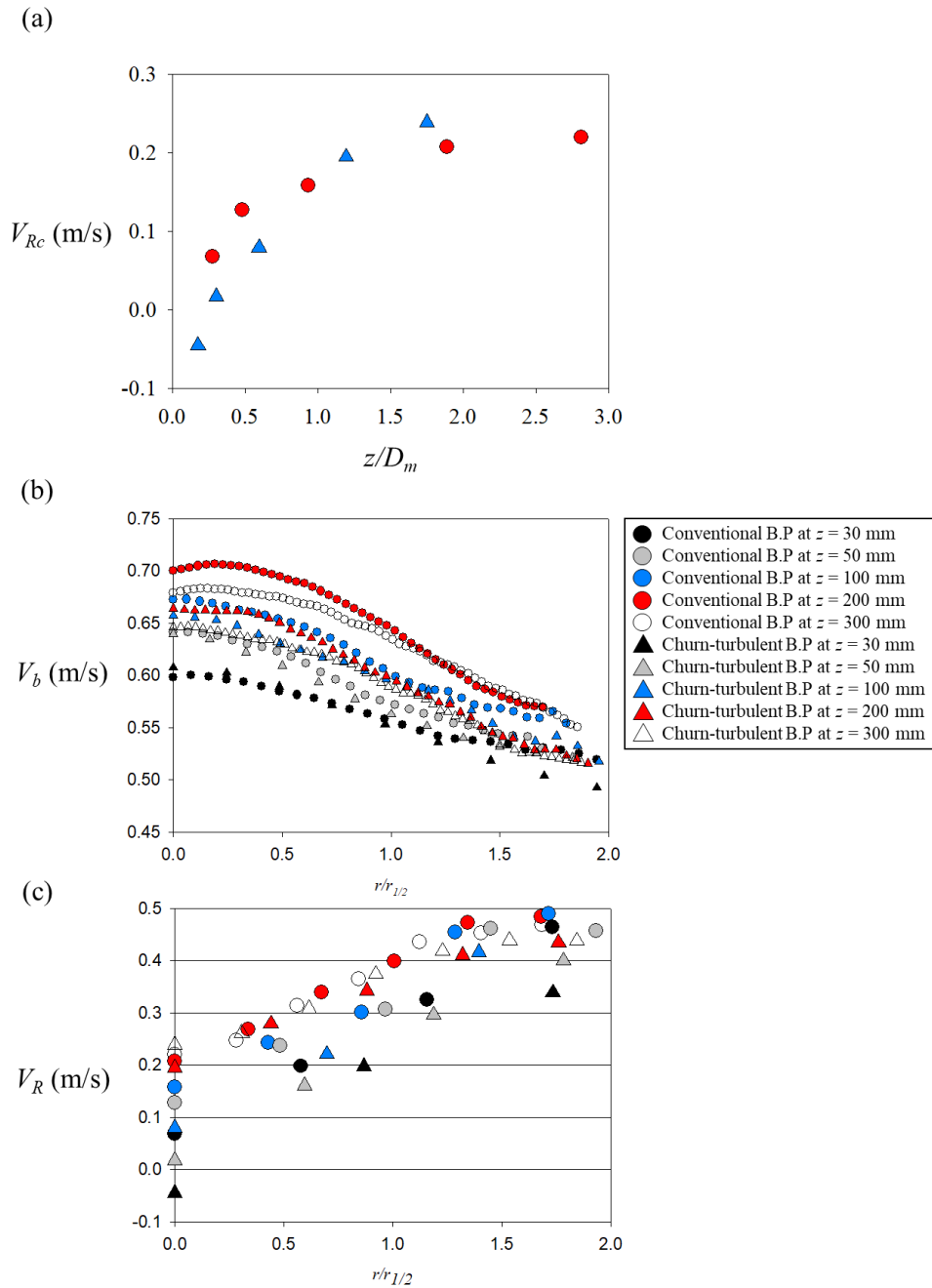


FIGURE 3.5. Gas phase parameters: (a) vertical variation of the central relative rise velocity of a bubble and the radial distribution of the (b) time-averaged bubble velocity, and (c) bubble relative velocity.

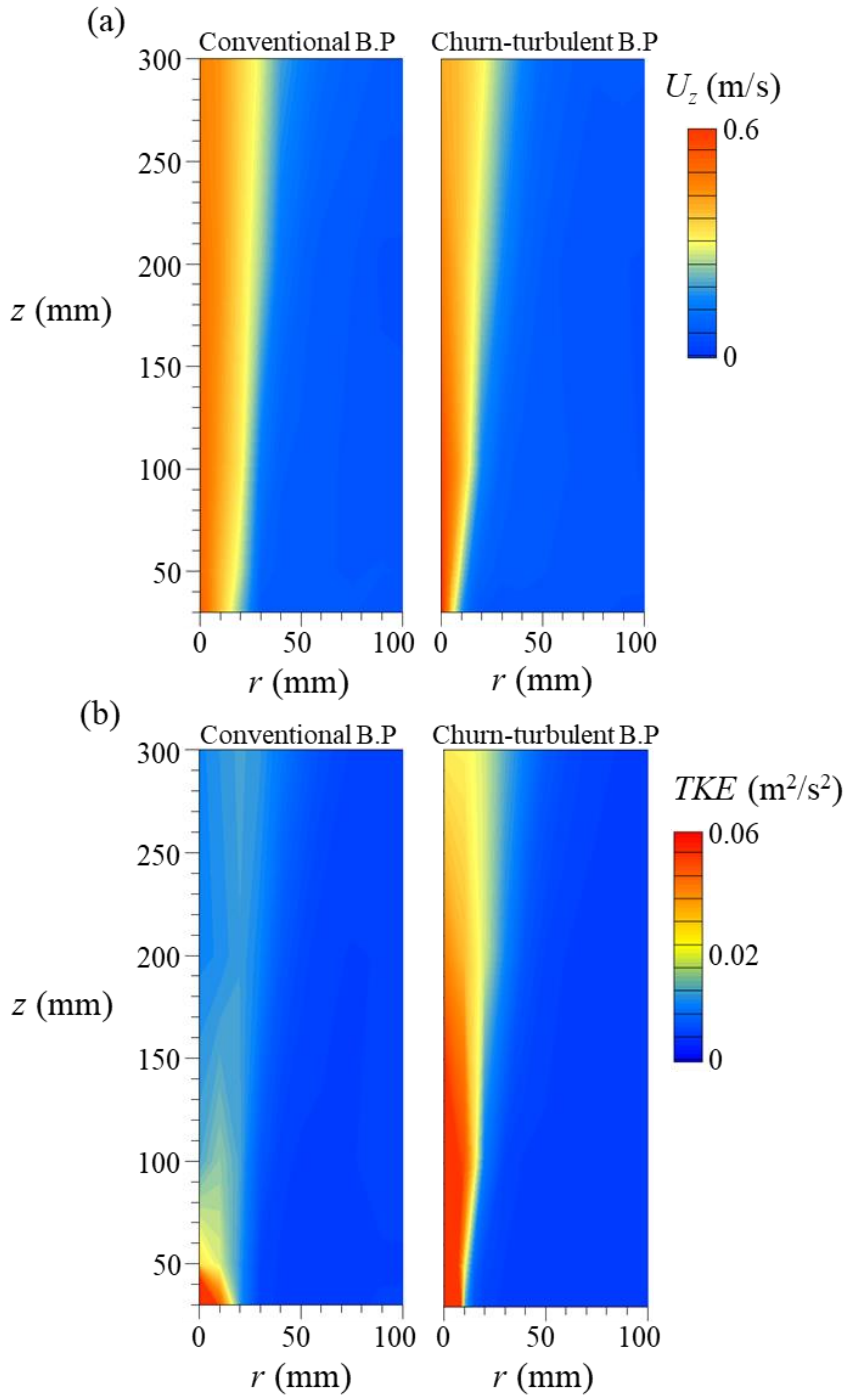


FIGURE 3.6. Time averaged liquid velocity contour obtained by LDA (a)  $U_z$  and (b) Turbulence kinetic energy (Left: conventional bubble plume; Right: churn-turbulent bubble plume).

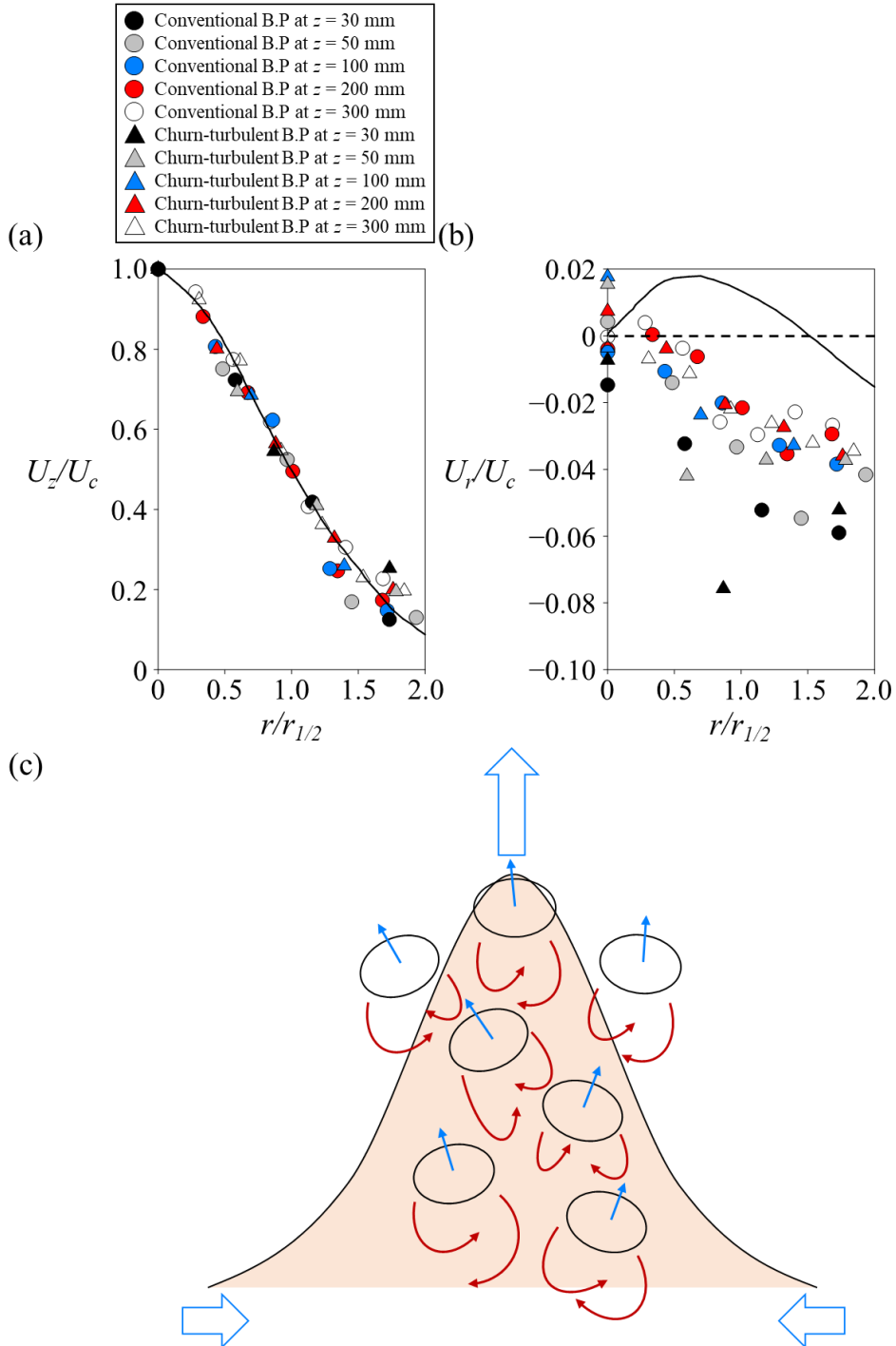


FIGURE 3.7. Time-averaged profiles of (a) liquid axial velocity, and (b) liquid radial velocity. (c) A schematic representing the time-averaged plume velocity field.

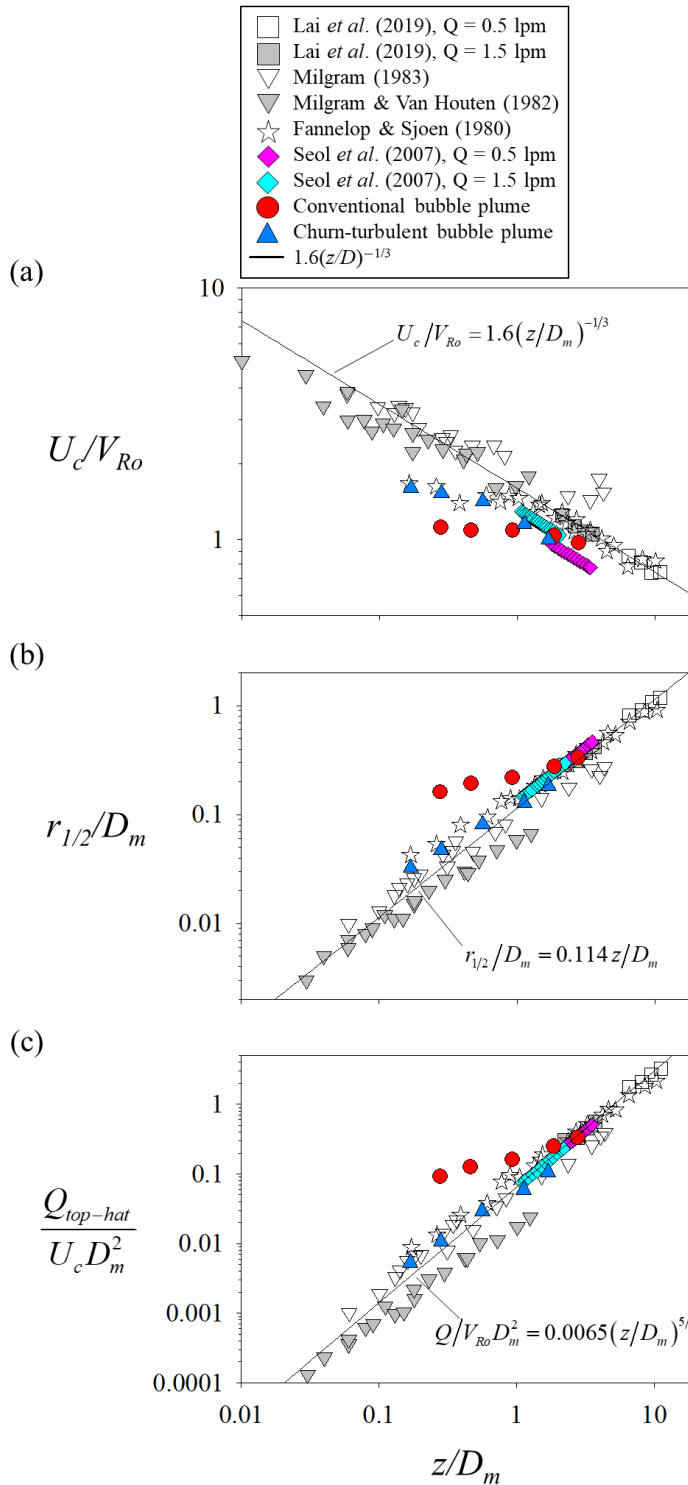


FIGURE 3.8. Comparison with the previously suggested empirical relation by Lai *et al.* (2019) including the previous results: (a) normalized central velocity, (b) normalized  $r_{1/2}$ , and (c) normalized  $Q_{top-hat}$

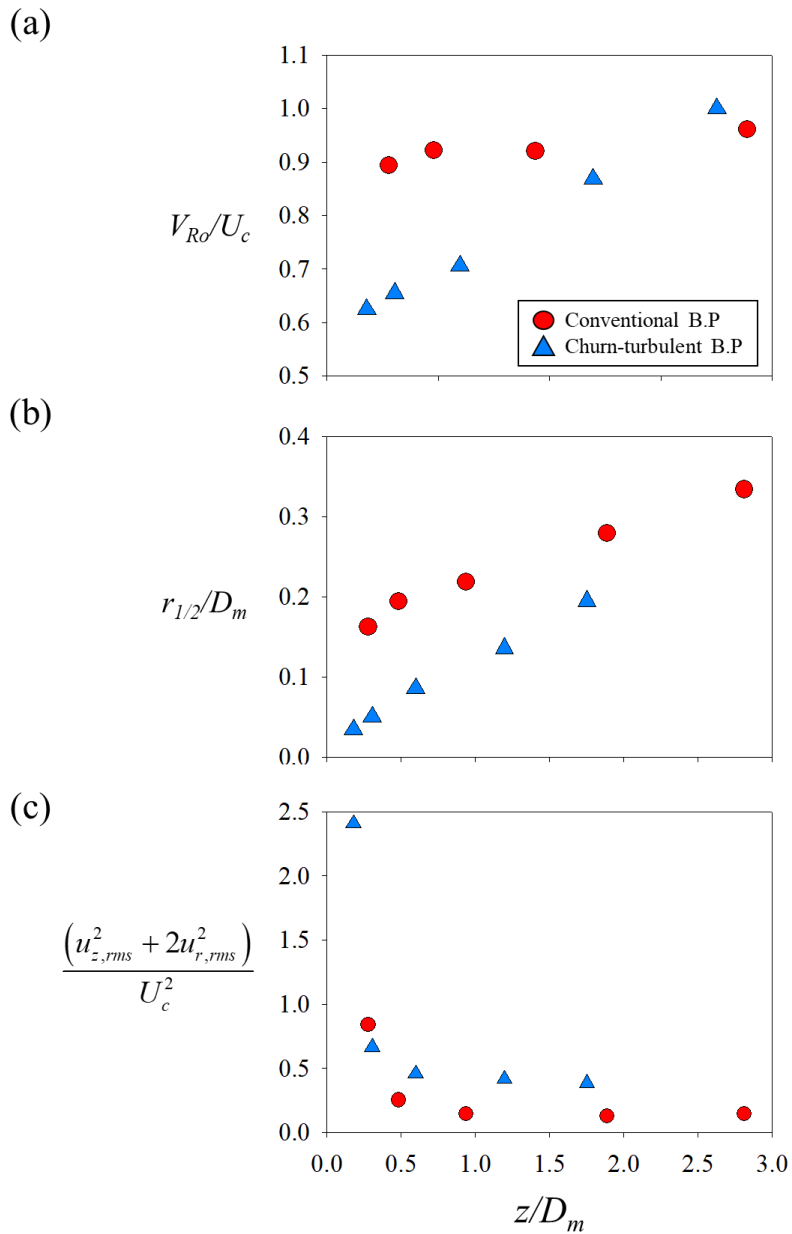


FIGURE 3.9. Axial variation of the liquid parameters: (a) the inverse of the central velocity normalized by bubble relative velocity, (b) the normalized  $r_{1/2}$ , and (c) the normalized turbulence kinetic energy.

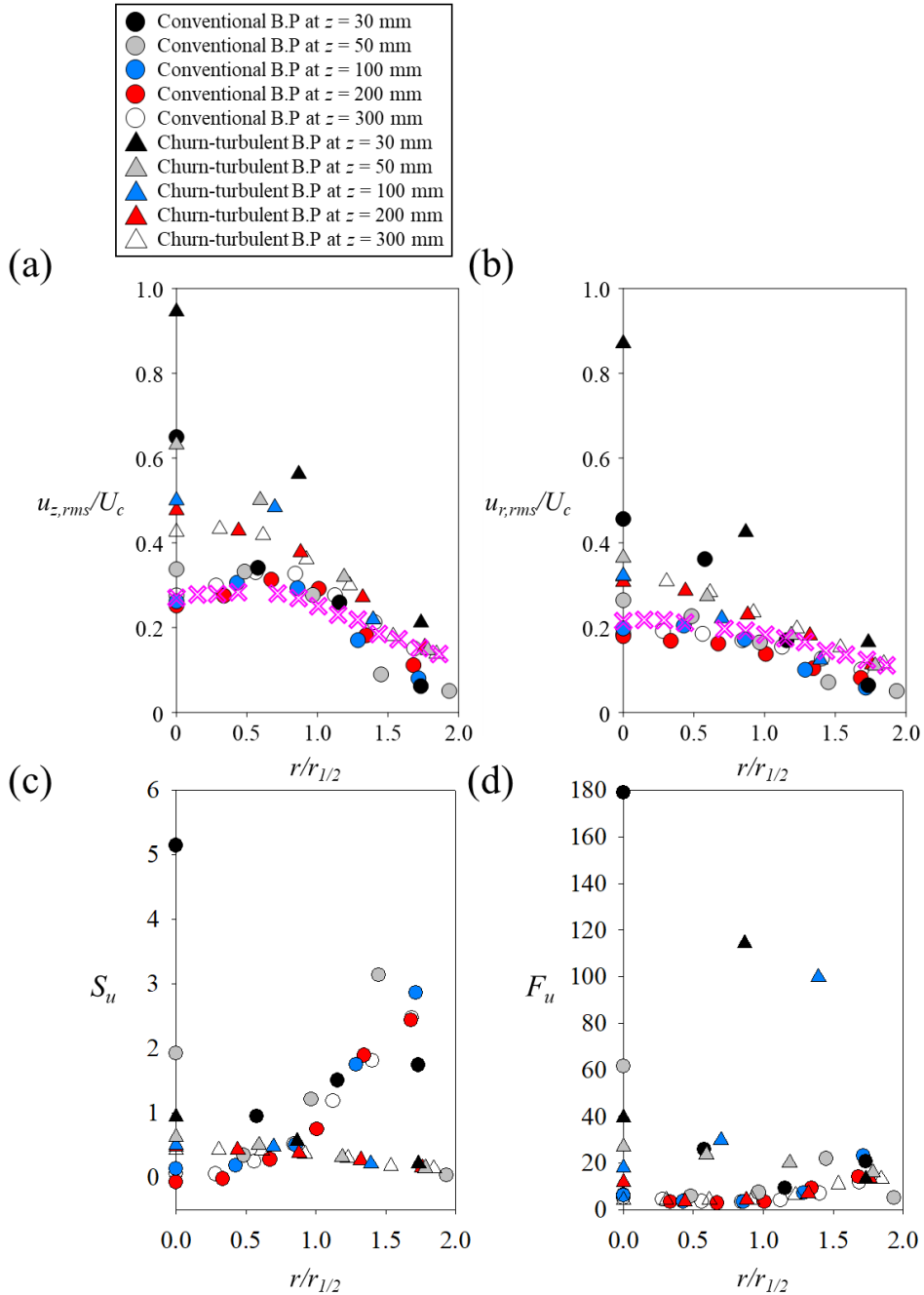


FIGURE 3.10. Turbulence statistics of the liquid fluctuation velocity normalized by central velocity. (a) root-mean square vertical velocity, (b) root-mean square radial velocity, (c) skewness of the vertical liquid velocity fluctuation, and (d) flatness of the vertical liquid velocity fluctuation.

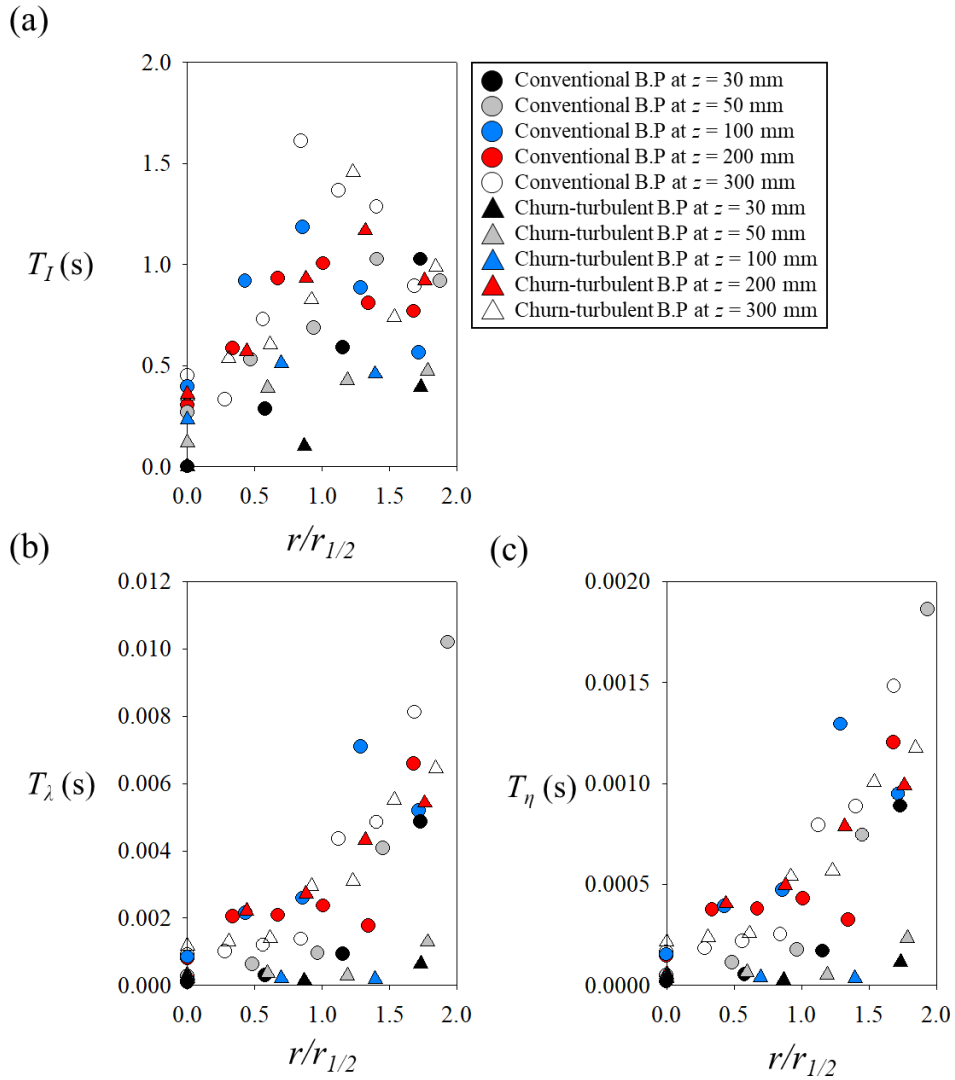


FIGURE 3.11. Characteristic time scales of the liquid vertical velocity fluctuation. (a) Integral time scale, (b) Taylor microscale, and (c) Kolmogorov time scale.

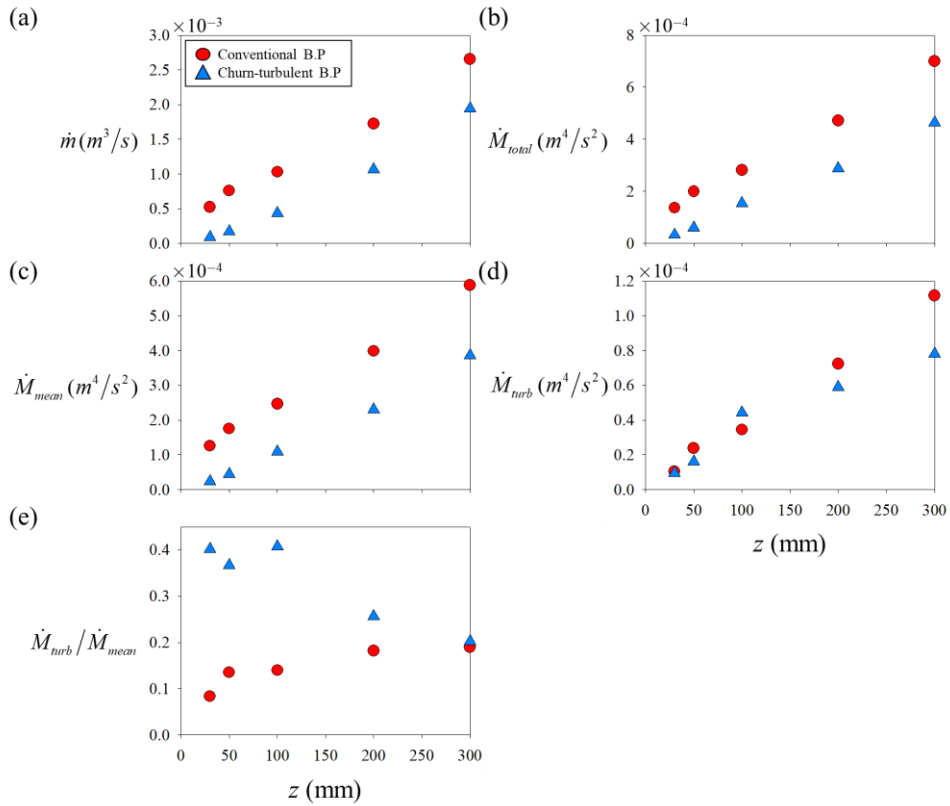


FIGURE 3.12. Integrated parameters of the induced liquid plume. (a) mass flow rate, (b) total momentum flow rate, (c) mean momentum flow rate, (d) turbulence momentum flow rate, and (e) the ratio of turbulence to mean momentum flow rate.

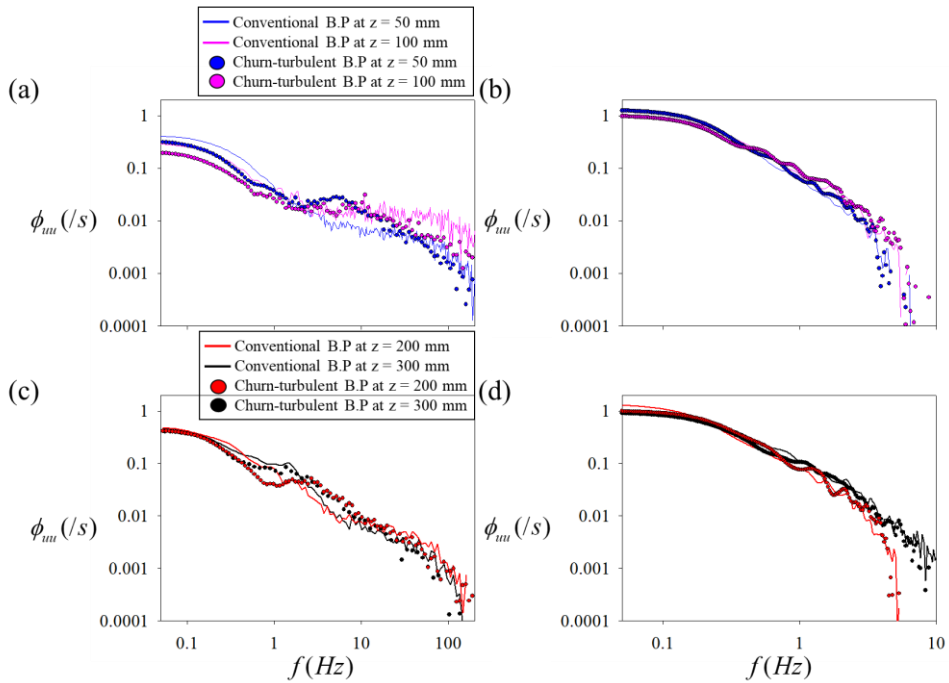


FIGURE 3.13. Energy spectrum of the vertical liquid velocity fluctuations at the center ( $r = 0$  mm) and the edge ( $r = 75$  mm) of the induced liquid plume. (a)  $r = 0$  mm,  $z = 50, 100$  mm, (b)  $r = 75$  mm,  $z = 50, 100$  mm, (c)  $r = 0$  mm,  $z = 200, 300$  mm, (d)  $r = 75$  mm,  $z = 200, 300$  mm.

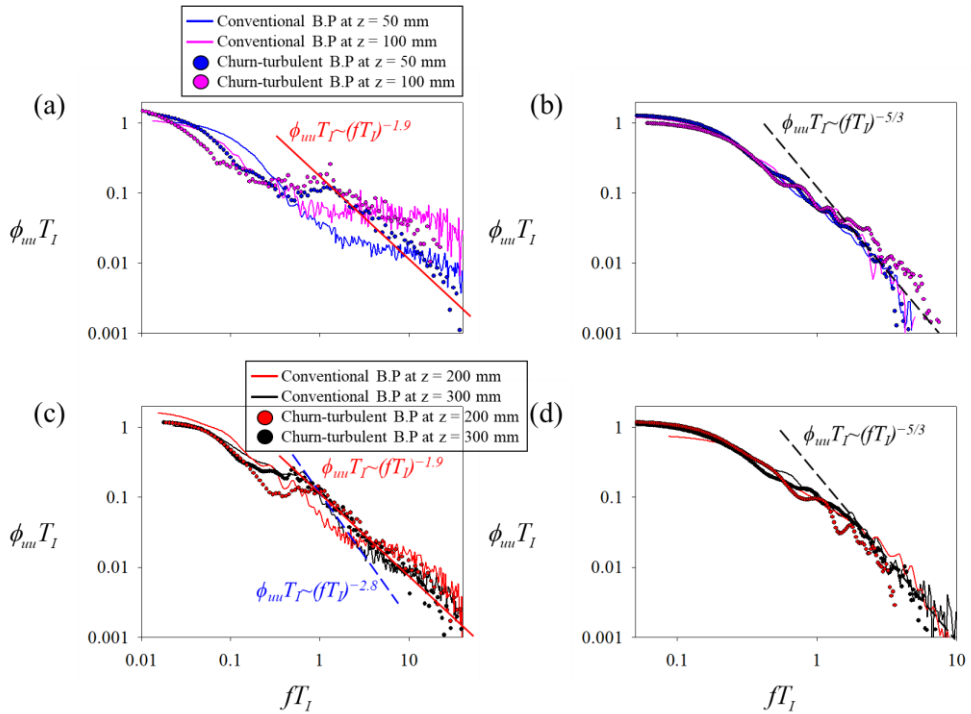


FIGURE 3.14. Energy spectrum of the vertical liquid velocity fluctuations at the center ( $r = 0$  mm) and the edge ( $r = 75$  mm) of the induced liquid plume normalized by integral time scale. (a)  $r = 0$  mm,  $z = 50, 100$  mm, (b)  $r = 75$  mm,  $z = 50, 100$  mm, (c)  $r = 0$  mm,  $z = 200, 300$  mm, (d)  $r = 75$  mm,  $z = 200, 300$  mm.

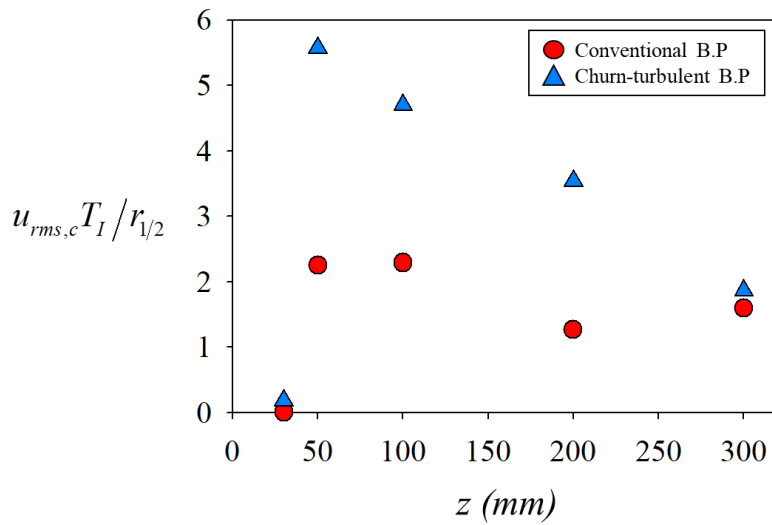


FIGURE 3.15. Characteristic length scale of energy bump representing spectral energy injection by bubbles.

## Chapter 4

# An analytical framework to characterize the bubble-induced turbulence

### 4.1 Background

During past decades, there has been a noticeable enhancement in our understanding of the turbulence characteristics in a gas-liquid two-phase flow; however, it is also true that we need a universal (independent of gas-liquid flow geometry) framework (or relation) to characterize the bubble-induced turbulence (agitation) and gas-phase statistics (Risso 2018). Depending on the flow geometry or regime, there have been some models (or parameters) developed to successfully explain the bubble-induced turbulence in the flow targeted therein; specifically, for a bubble swarm (Riboux *et al.* 2010; Risso 2018; Lee & Park 2020), bubbles with grid turbulence (Rensen *et al.* 2005; Alm eras *et al.* 2017), and bubbly channel (pipe) flow (Ma *et al.* 2020a, 2020b), to name a few. As we will introduce below, we think it is still necessary to have an approach to describe the contribution of bubble statistics on the two-phase flow turbulence with a unified framework. This is mostly because the main source of turbulence modulation by rising bubbles is originated from the dynamics of the bubble wake, which varies in time, space, and scales (Risso & Ellingsen 2002; Riboux *et al.* 2010; Risso 2016; Alm eras *et al.* 2017; Risso 2018; Ma *et al.* 2020b; Lee *et al.* 2021).

Maybe the simplest approach to characterize the bubble-induced turbulence is the ratio of bubble size ( $\overline{d_b}$ ) to the integral length scale ( $L_I$ ) of the flow; Gore & Crowe (1989) suggested that the turbulence is enhanced (suppressed) when  $\overline{d_b}/L_I$  is larger (smaller) than approximately 0.1. This is quite intuitive such that in the turbulence energy spectrum, the eddies larger than the integral length scale take the role of turbulence production (Tennekes & Lumley 1972). On the other hand, for a homogeneous bubble swarm, the simplest geometry of a bubbly flow, in which the bubbles are injected homogeneously over the entire domain (without the confinement effect) containing an otherwise stagnant water, the variance of liquid velocity fluctuation was related to the bubble rise velocity and void fraction as  $u'_{z,rms} = V_o \alpha^{0.4}$  (Risso & Ellingsen 2002; Riboux *et al.* 2010; Lee & Park 2020). Here,  $u'_{z,rms}$  is the root-mean-square streamwise liquid fluctuation velocity,  $V_o$  is the averaged rising velocity of a single bubble, and  $\alpha$  is the volume void fraction. This relation, validated up to a moderate value ( $< 10\%$ ), was found to be useful when the flow statistics are uniform along the transverse (horizontal) direction (Riboux *et al.* 2010) and there is no background liquid flow so that the flow disturbance caused by individual bubbles are attributed to global variables like volume void fraction. However, it is not easy to apply this to other types of bubbly flow with a confinement effect or existing background turbulence, partly because it was a phenomenological model that came from the physical intuition, not derived from the governing equation of the flow. Many studies have reported that the

bubbles even with the same condition affect the turbulence differently (even the turbulence reduction, somewhat opposite to our intuition) depending on the turbulence in the background liquid flow (Lance & Bataille 1991; Shawkat *et al.* 2008; Prakash *et al.* 2016; Alm eras *et al.* 2017; Lee *et al.* 2021).

The bubblance parameter ( $b$ ), defined to compare the energy associated with the bubble-induced perturbations of the liquid with the turbulent kinetic energy in the background flow (Lance & Bataille 1991; Rensen *et al.* 2005), in this sense is a good approach to understand the bubble-induced turbulence. Considering the pseudo-turbulent contribution by bubbles as  $\sim \alpha V_R^2$  (van Wijngaarden 1998), where  $V_R$  is the relative bubble velocity, and the turbulent kinetic energy is scaled as  $\sim u_o'^2$ , where  $u_o'$  is the velocity fluctuation (typically vertical direction component without the presence of bubbles), it is defined as:

$$b \sim \alpha V_R^2 / u_o'^2 . \quad (4.1)$$

By definition, the turbulent-dominant flow belongs to  $b < \sim 1.0$  ( $b = 0$  represents a single-phase flow), whereas the flow mostly driven by the rising bubbles to  $b > \sim 1.0$  ( $b = \infty$  corresponds to a bubble swarm in a quiescent liquid (pseudo-turbulence), as a limiting case). When the rising bubbles interact with the grid turbulence, the liquid velocity fluctuation was measured to scale as  $u_{l,rms}'^2 \sim b^{0.4}$  ( $b < 0.7$ ) and  $u_{l,rms}'^2 \sim b^{1.3}$  ( $b > 0.7$ ) (Alm eras *et al.* 2017). On the other hand, Rensen *et al.* (2005) commented that the appearance of -3 (or -8/3) slope in an energy spectrum, which is commonly reported as a trait of bubbly flows, was not determined by bubblance parameter alone. In some cases, -3 exponent was not observed even for  $b = \infty$  (Mudde *et al.* 1997; Mudde & Saito 2001; Cui & Fan 2004; Mazzitelli & Lohse 2005), while Prakash *et al.* (2016) measured it for the case with the bubblance parameter as small as 0.01. As noticed, it is not possible to relate the bubblance parameter to the conditions of bubble-induced turbulence reduction. While driving our framework, we will revisit the bubblance parameter and discuss more in section 4.2.

As we have addressed, it becomes more difficult to characterize the two-phase flow turbulence with a set of global parameters as the flow geometry becomes more complex. First, the statistical approach is not readily applicable for the developing flow transiently in time and space. For example, for a bubble plume important for fluid mixing and heat transfer in natural and industrial processes (Milgram 1983; Bombardelli *et al.* 2007; Fraga & Stoesser 2016; Lai & Socolofsky 2019; Boufadel *et al.* 2020), bubble-induced entrainment of time-averaged mass ( $\dot{m}$ ) and momentum ( $\dot{M}$ ) flow rates along the vertical ( $z$ ) direction has been modeled into  $d\dot{m}/dz = 2\alpha_e \sqrt{\pi \dot{M}}$  and  $d\dot{M}/dz = (\rho_l / \rho_p - 1) / g \lambda^2 (\dot{m}^2 / \dot{M})$ ,

respectively. Here,  $\rho_l$  and  $\rho_p = (1 - \alpha)\rho_l + \alpha\rho_b$  is the density of the liquid and the gas-liquid mixture, respectively ( $\rho_b$ : the gas density),  $\alpha_e$  is the entrainment coefficient,  $g$  is the gravitational acceleration, and  $\lambda$  is the fraction of plume width containing bubbles (Wuest *et al.* 1992; Bombardelli *et al.* 2007). As shown, it was less modeled of its turbulence characteristics, and for now, it is understood that the

similarity, among different bubble source conditions, is achieved at  $z/D \geq 5.0$ , where  $D$  is the characteristic length scale obtained from the above 1D plume model (Bombardelli *et al.* 2007; Lai & Socolofsky 2019). At  $z/D < 5.0$ , on the other hand, turbulence kinetic energy of the liquid flow is maximized where bubble relative velocity is the highest (Simiano *et al.* 2009); it has been reasonably supported, from other studies, that the relative bubble velocity is highly relevant to the liquid-phase turbulence. The bubble parameter, in terms of relative bubble velocity, is infinity in a bubble plume by definition, thus, cannot provide a useful explanation for this tendency.

Secondly, the confinement effect, i.e., the existence of the solid wall, causes the locally varying, e.g., from the core to the near-wall region in a bubbly pipe flow, turbulence characteristics (Shawkat *et al.* 2008; Hosokawa & Tomiyama 2013; Kim *et al.* 2016; Lee *et al.* 2021). For a bubbly pipe flow, most of the previous efforts focused on developing a two-phase Reynolds stress model, starting from the assumption that the flow velocity can be decomposed as a linear superposition of time-averaged, fluctuating (without bubbles) and bubble-induced fluctuating components (Sato & Sekoguchi 1975, 1981). They can be roughly assorted as the eddy-viscosity model (Sato & Sekoguchi 1975, Ma *et al.* 2017), a transport equation for Reynolds stress (Kataoka *et al.* 1992; Ma *et al.* 2020b), and an explicit algebraic equation for Reynolds stress (Hosokawa & Tomiyama 2013; Kim *et al.* 2016; Ma *et al.* 2020a; Lee & Park 2020). While comparing the strengths and limitations of each strategy is out of the scope of the present study, each showed quite a good agreement with the data set chosen for validation. Although it has not been reported that these models can characterize (or predict) the bubble-induced turbulence in different types of flow geometry, it is possible to draw some insightful lessons from the above models; that is, interfacial stress term, which is a function of bubble Reynolds number ( $Re_b = V_r \bar{d}_b / \nu$ ) and volume void fraction, has a critical role in determining the Reynolds stress (for both diagonal and off-diagonal components) (Ma *et al.* 2020a, 2020b).

It can be summarized that different approaches have been taken to uncover the physics of bubble-induced turbulence occurring in various types of flow geometry, which has enhanced our knowledge substantially. However, our effort toward a unified framework is still ongoing, which can characterize the effect of rising bubbles on the turbulence in the flow, whether it is developing or fully developed, or in an open or confined environment. Motivated by this necessity, in the present study, we try to answer our question of whether it is possible to draw a set of global parameters, which describe the relation between bubble-induced turbulence and gas-phase flow statistics. Our main idea is to perform a scaling analysis of the two-phase averaged Navier-Stokes equation, which includes the terms for interfacial momentum transfer (most of the bubble-induced agitation is related to the interface dynamics) and resulting flow (time-averaged and fluctuating velocities). With some assumptions, reasonably correct for the bubble swarm, we derived a scaling relation including a dimensionless variable fairly similar (not exactly the same) to the bubble parameter, which was validated with available experimental data in the literature. The same relation is to be successfully extended to bubble plume and bubbly pipe flows (including our own experiments for both). While this may not be a complete solution like the closure model, we think the present approach is very

useful toward the unified description of the bubble-induced turbulence, compensating for the limitations of the bubbance parameter.

## 4.2 Scaling analysis of two-phase averaged Navier-Stokes equation

### 4.2.1 Revisit to the bubbance parameter

In this section, we are going to derive the bubbance parameter with the scaling relation between the Reynolds stress and the interfacial momentum transfer term. With this, it comes out that the bubbance parameter is nothing but a limiting case of the normalized interfacial momentum transfer term. Thus, it becomes clear that a different form of normalized interfacial momentum transfer term (corresponding to the bubbance parameter for rising bubbles under the prescribed grid turbulence) is required for different flow geometry.

Let us consider the time-averaged two-phase averaged Navier-Stokes equation for the liquid phase (du Cluzeau *et al.* 2020b), in which the local phenomena occurring near the bubble surface relevant to the interaction with the surroundings (e.g., enhanced energy dissipation due to interface deformation, accumulation and shedding of vorticity in the shear layer, and resulting vortex dynamics in bubble wakes) are implemented as an interfacial momentum transfer term. They are strongly related to the fundamental, including turbulent, behaviour of bubbly flows (Balachandar & Eaton 2010; Balachandar 2020). The equation is stated as:

$$\begin{aligned} \nabla \cdot [(1-\alpha)\rho_l \mathbf{U}\mathbf{U}] = & -\nabla [(1-\alpha)\bar{p}_l] + \nabla \cdot [(1-\alpha)\bar{\tau}_\mu] - \nabla \cdot [(1-\alpha)\rho_l \overline{\mathbf{u}'\mathbf{u}'}] \\ & + (1-\alpha)\rho_l \mathbf{g} + \overline{\sigma\kappa\nabla\chi_b} - \Phi_b \end{aligned} \quad (4.2)$$

Here, the index l and b denotes the liquid and the gas phase, respectively, and the overbar represents the time average,  $\chi_k$  is the phase indicator function (1 in the case of phase  $k$  and 0 otherwise). A vector is represented by a bold letter. The liquid velocity vector is decomposed into the mean and fluctuating part as  $\mathbf{u} = \mathbf{U} + \mathbf{u}'$ , and  $\bar{p}_l$  is the time-averaged pressure for liquid.  $\bar{\tau}_\mu = \mu_l(\nabla\mathbf{U} + \nabla^T\mathbf{U})$  is the time-averaged viscous stress of liquid phase, and  $\overline{\sigma\kappa\nabla\chi_b}$  denote the surface tension force, where  $\sigma$  and  $\kappa$  are the surface tension and the local curvature, respectively.  $\alpha$  is the time-averaged volume void fraction of the gas phase. Finally,  $\Phi_b$  counts the interfacial momentum transfer on the gas phase. If we can assume that the contribution of mean shear ( $\nabla \cdot [(1-\alpha)\rho_l \mathbf{U}\mathbf{U}]$ ), pressure gradient ( $-\nabla [(1-\alpha)\bar{p}_l]$ ), gravity ( $(1-\alpha)\rho_l \mathbf{g}$ ), and surface tension ( $\overline{\sigma\kappa\nabla\chi_b}$ ) is negligible compared to the Reynolds stress term ( $-\nabla \cdot [(1-\alpha)\rho_l \overline{\mathbf{u}'\mathbf{u}'}]$ ). then we draw the following scaling relation from equation (4.2).

$$\nabla \cdot [(1-\alpha)\rho_l \overline{\mathbf{u}'\mathbf{u}'}] \sim -\Phi_b \quad (4.3)$$

The above assumptions are reasonably acceptable for the case of the

homogeneous bubble swarm and rising bubbles under the prescribed grid turbulence (Lance & Bataille 1991; Alm eras *et al.* 2017), considering that the homogeneity of background flow. The details of this derivation are described in section 4.3. Equation (4.3) states that under previously listed assumptions, the Reynolds stress term is scaled with the interfacial momentum transfer term. In other words, the Reynolds stress of the liquid phase is mainly determined by the interfacial momentum transfer term and if we specify the functional expression of  $\Phi_b$  in terms of liquid and gas phase parameters, that could be also the functional description of the Reynolds stress of the liquid phase.

Although there is an ongoing debate on the accuracy (or validity) of some force terms composing of the interfacial momentum transfer term,  $\Phi_b$  (Ishii & Hibiki 2011; Ling *et al.* 2013), we are to follow the two-fluid formulation by Ishii & Hibiki (2011), applied for a wide range of volume void fractions (see section 4.2.2 for the details on  $\Phi_b$ ). Among the various components in  $\Phi_b$ , for the moment, we consider that the drag force ( $\Phi_b \sim \alpha V_R^2 / \bar{d}_b$ ) is the most dominant, which is the case where the flow without spatial acceleration (for example, the homogeneous bubble swarm, rising bubbles under the prescribed grid turbulence, and fully developed bubbly pipe flow) (Ishii & Hibiki 2011). If bubble diameter is selected as the characteristic length scale of the liquid velocity field variation, equation (4.3) is scaled as  $(1 - \alpha)\rho_l u_{z,rms}'^2 / \bar{d}_b \sim \alpha V_R^2 / \bar{d}_b$ . Finally, the following scaling relation can be obtained when both sides of the equation are divided by  $u_o'^2$ .

$$\frac{u_{rms}'^2}{u_o'^2} \sim \frac{\alpha}{1 - \alpha} \frac{V_R^2}{u_o'^2} \quad (4.4)$$

Interestingly, it is found that the right-hand side of equation (4.4) is quite similar to the bubbance parameter; it becomes identical to equation (4.1), if the volume void fraction is very small ( $\alpha \ll 1.0$ ). The left-hand side of equation (4.4) represents the ratio of turbulence intensity of bubbly flow to that of a single-phase flow (without bubbles), as expected, which shows that the bubbance parameter is somehow related to the bubble-induced turbulence. Furthermore, it is understood that the bubbance parameter is equivalent to the normalized interfacial momentum transfer term considering the drag force only; in the below, we will discuss how the above scaling relation can be modified and applied to different flow geometries (and conditions). It is obvious that some of the assumptions that were used to derive equation (4.4) need to be re-assessed and adjusted according to the characteristics of the bubbly flow.

## 4.2.2 Interfacial momentum transfer term, $\Phi_b$

As we have shown above, it will be very important how we deal with the interfacial momentum transfer term, and we are to discuss its formulation and meaning. As shown in equation (4.5), the interfacial momentum transfer is mostly contributed by the drag ( $\Phi_{b,DR}$ ), lift ( $\Phi_{b,LT}$ ), virtual mass ( $\Phi_{b,VM}$ ), basset history ( $\Phi_{b,BH}$ ), and turbulent dispersion forces ( $\Phi_{b,TD}$ ) (Ishii & Hibiki 2011). These force terms can be further divided into the convective ( $\Phi_{b,conv} = \Phi_{b,VM} + \Phi_{b,BH}$ ) and the non-convective ( $\Phi_{b,N-conv} = \Phi_{b,DR} + \Phi_{b,LT} + \Phi_{b,TD}$ ) components, which are dominant

when there is convective (spatial) acceleration or not, respectively. Please note that because we are dealing with the time-averaged case, ‘acceleration’ means spatial acceleration only.

$$\Phi_b = \Phi_{b,DR} + \Phi_{b,LT} + \Phi_{b,TD} + \Phi_{b,VM} + \Phi_{b,BH} \quad (4.5)$$

In general, bubbles rise along the vertical direction in a typical configuration of bubbly flow, so, we focus on the vertical component (i.e.,  $z$ -direction) of each force term. The drag force is proportional to the void fraction and relative bubble velocity as  $\Phi_{b,DR} = -0.5\alpha C_D (A_b/B_b) \rho_l V_R^2 \cong -(4/3)\alpha C_D \rho_l V_R^2 / d_b$  (Ishii & Hibiki 2011). Here,  $C_D$  is the drag coefficient,  $A_b$  and  $B_b$  are the projected area and volume of the bubble, respectively. The relative bubble velocity is defined as  $V_R = V_b - U_z$ , where  $U_z$  is the vertical component of the time-averaged liquid velocity. In the case of the lift and the turbulent dispersion force, the direction of these forces is the horizontal direction (Ishii & Hibiki 2011). Therefore,  $\Phi_{b,N-conv}$  is dominated by drag force. This assumption is supported by DNS results of du Cluzeau *et al.* 2020b. Finally, we have the following scaling relation.

$$\Phi_{b,N-conv} \cong \Phi_{b,DR} \sim -\frac{1}{d_b} \rho_l \alpha V_R^2 \quad (4.6)$$

Among the convective contributions, the virtual mass force (Ishii & Hibiki 2011) is formulated as equation (4.7).

$$\begin{aligned} \Phi_{b,VM} &= -C_M \alpha \rho_l \left( \frac{D_b V_R}{Dt} - V_R \cdot \nabla U \right) = -C_M \alpha \rho_l \left( V_b \frac{\partial}{\partial z} V_R - V_R \frac{\partial}{\partial z} U_z \right) \\ &\sim -\alpha \rho_l \left( \frac{V_b V_R}{L_z} \right) \sim -\alpha \rho_l \frac{(U_c + V_R) V_R}{L_z} \sim -\alpha \rho_l \frac{V_R U_c + V_R^2}{L_z} \end{aligned} \quad (4.7)$$

Here,  $D_b/Dt = \partial/\partial t + V_b \cdot \nabla$  is the material derivative in terms of the bubble velocity  $V_b$  and  $C_{VM}$  is the virtual mass coefficient. As we are focusing on the time-averaged equation, the time derivative as zero in equation (4.2), only the convective acceleration remains for  $D_b/Dt$ , by which  $D_b V_R/Dt$  is scaled with  $V_b V_R/L_z$ , where  $L_z$  is the characteristics length scale for the liquid velocity gradient in the vertical direction. Similarly,  $V_R \cdot \nabla U$  is scaled to  $V_R U_c/L_z$ , where  $U_c$  is the vertical component of the characteristic velocity of liquid phase flow. Because  $V_b > U_z$ ,  $(V_b \frac{\partial}{\partial z} V_R - V_R \frac{\partial}{\partial z} U_z)$  term can be scaled as  $(V_b V_R/L_z)$ . On the other hand, the basset history force, responsible for the history of the bubble as it moves in the unsteady flow field, is determined by differences in the acceleration of bubble and surrounding fluid and shown in equation (4.8) (Ishii & Hibiki 2011).

$$\Phi_{b,BH} = -\frac{9\alpha}{\pi} \rho_l \sqrt{\frac{\mu_m}{\mu_l}} \left( \frac{D_b V_R}{Dt} \right) \sim -\alpha \rho_l \frac{U_b V_R}{L_z} \sim -\alpha \rho_l \frac{V_R U_c + V_R^2}{L_z} \quad (4.8)$$

Here,  $\mu_m$  is the gas-liquid mixture viscosity. Following the same scaling approach, it is possible to find that  $\Phi_{b,BH}$  is scaled with  $V_b V_R$ , which is again expanded to  $V_R U_c + V_R^2$ . It is noted that in equation (4.8), the term of  $V_R U_c$  comes from the convective derivative of relative bubble velocity,  $V_R$ . From equations (4.7) and (4.8), we see that the comprehensive scaling relation for  $\Phi_{b,conv}$  is reasonably given with the equation (4.9), which can embrace both contributions from both virtual mass and basset history forces.

$$\Phi_{b,conv} \sim -\alpha \rho_l \frac{V_R U_c + V_R^2}{L_z} \quad (4.9)$$

As we will discuss later, the consideration of  $\Phi_{b,conv}$  is the key in the successful characterization of bubble-induced turbulence in different flow geometries.

### 4.2.3 Contribution of surface tension force

In the two-phase averaged Navier-Stokes equation (equation (4.2)), the contribution of surface tension is given by  $(\overline{\sigma \kappa \nabla \chi_b})$ , which is decomposed into averaged and fluctuating terms as  $\overline{\sigma \kappa \nabla \chi_b} = \overline{\sigma(\bar{\kappa} + \kappa') \nabla(\bar{\chi}_b + \chi'_b)}$   
 $\overline{\sigma \kappa \nabla \chi_b} = \overline{\sigma(\bar{\kappa} + \kappa') \nabla(\bar{\chi}_b + \chi'_b)} = \overline{\sigma(\bar{\kappa} + \kappa') \nabla(\alpha + \chi'_b)}$ . Therefore,

$$\overline{\sigma \kappa \nabla \chi_b} = \overline{\sigma \bar{\kappa} \nabla \alpha} + \overline{\sigma \kappa' \nabla \chi'_b} \quad (4.10)$$

This states that the role of surface tension consists of the time-averaged component  $(\overline{\sigma \bar{\kappa} \nabla \alpha})$  and the fluctuation component  $(\overline{\sigma \kappa' \nabla \chi'_b})$ , and du Cluzeau et al. (2020) modeled the second part as  $\overline{\sigma \kappa' \nabla \chi'_b} \sim \nabla \alpha$ . In the present approach, we will adopt the scaling relation for the surface tension term, as shown in equation (4.11).

$$\overline{\sigma \kappa \nabla \chi_b} \sim \nabla \alpha \quad (4.11)$$

As far as the relation (4.11) satisfies, the surface tension force term can be neglected in the vertical component of the momentum equation with the system which is statistically homogeneous along the vertical direction. On the other hand, in the case of we are dealing with developing flow such as bubble plume, a contribution of surface tension force term varies depending on Weber number defined by the characteristic length scale of the flow (see below for the details).

## 4.3 Relation between total liquid momentum and interfacial momentum transfer for bubble plume

In section 4.2, we have shown how the interfacial momentum transfer and surface tension terms can be scaled when we consider the two-phase averaged Navier-Stokes equation in a typical (in which the Reynolds stress term is dominant compared to terms representing the mean shear, pressure gradient, gravity, viscous effect, and the surface tension effect) range of gas-liquid flows. In this section,

starting from equation (4.3) or an equivalent form, we will derive and discuss the usefulness of the scaling relations between liquid turbulence statistics and bubble parameters for different configurations of bubbly flow such as a homogeneous bubble swarm, bubbles with grid turbulence, bubble plume, and bubbly pipe flow (results for the geometries except bubble plume are described in chapter 7, appendix). The flow conditions of the gas-liquid flows, used for validation, are summarized in table 1, including some important dimensionless parameters. It is noted that to check the universality of the present relation, we tried to collect the available data in the literature, from our own experiments and others, in which the information of liquid-phase turbulence and bubbles is adequately provided. Excluding the bubble plume data of the present study, the averaged bubble diameter was 1.4 to 6.3 millimeters, and the maximum volume void fraction was 14 %. In the case of the bubble plume, the averaged bubble diameter was 4.6 – 7.0 mm, and the maximum volume void fraction was very high, 33%. These data cover various types of bubbly flows. In some cases, turbulence is solely induced by bubbles while in other cases, it is determined by an interaction between background flow and a bubble-induced agitation. On the other hand, in some cases, the flow is statistically homogeneous along the vertical direction, whereas, in other cases, the system is developing along the vertical direction (i.e., there is a convective acceleration even in the time-averaged statistics).

For the cases of homogeneous bubble swarm with or without background turbulence, it was reasonably possible to neglect the effect of the spatial gradient of flow statistics (chapter 7); and it is obviously necessary to extend our approach to the condition, in which the bubble dynamics is more complex to cause non-uniform distribution. In this sense, the bubble plume (Lai & Socolofsky 2019) is regarded as a suitable configuration to examine using our approach. However, previous studies on bubble plume have mainly focused on the parameters at the plume scales, such as induced liquid plume width, central velocity, and integrated mass and momentum flux, as we have introduced. Accordingly, few experimental data were providing the spatial distribution of the gas-phase parameters like volume void fraction and bubble velocity of the bubble plume, so we were able to verify with our own data only.

It is well known that the spatial profile of liquid statistics in bubble plume scales well with the central velocity of the induced liquid plume and plume width (Lai & Socolofsky 2019), and it was confirmed that based on our measurement data (figure S1 in the supplementary material). Therefore, we will derive the governing equation through several approximations in the cylindrical coordinate for the two-phase averaged Navier-Stokes equation by referring to the process of deriving the governing equation in the single-phase jet. The assumptions we will use are as follows:

- ① Axisymmetry, ②  $U_r \ll U_z$ , ③  $\partial/\partial z \ll \partial/\partial r$ , ④ High  $Re = U_c L_r / \nu$ ,
- ⑤  $\bar{p}_\infty(z)|_{r>L_r} = \bar{p}_\infty$  (outside the plume, pressure is constant, i.e., the effect of circulation inside the bath is negligible), ⑥  $\overline{u'_r u'_r} \approx \overline{u'_\theta u'_\theta}$

Here, the characteristic length scale for variation of statistics along radial direction  $L_r$  is the radius of the induced liquid plume, which is defined as twice the full width at half maximum (FWHM) of the time-averaged streamwise liquid

velocity.  $L_z$  is a characteristic length scale for variation of statistics along axial direction and  $\nu$  is the kinematic viscosity of water. Among the above assumptions ②, ④, ⑥ were verified through the experimental data of this study (figure 4.1(a),(b),(e), and table 4.1), and ③ is simply derived from the assumption ② and continuity equation.

For the time-averaged liquid velocity field, the continuity equation  $\nabla \cdot [(1-\alpha)\mathbf{U}] = 0$  satisfies the relation.

$$\frac{\partial(1-\alpha)U_z}{\partial z} = -\frac{1}{r} \frac{\partial}{\partial r} r(1-\alpha)U_r \quad (4.12)$$

To normalize equation (4.2), both sides are multiplied by  $L/\rho_l U_c^2$  and divided by  $(1-\alpha)$ . Then we get equation (4.13). In this case,  $L_c$  is  $L_z$  for the axial direction and  $L_r$  for the radial direction. Here,  $\nabla^* = L_c \times \nabla$ ,  $\mathbf{U}^* = \mathbf{U}/U_c$ ,  $\mathbf{u}^* = \mathbf{u}'/U_c$ ,  $Fr = U_c^2/gL_c$ ,  $We = \rho_l V_R^2 L_c/\sigma$ ,  $\kappa^* = \kappa \bar{d}_b/2$ ,  $p^* = p/\rho_l U_c^2$ ,  $\tau_\mu^* = \tau/\rho_l U_c^2$ .

$$\begin{aligned} \frac{1}{(1-\alpha)} \nabla^* [(1-\alpha)\mathbf{U}^*\mathbf{U}^*] &= -\frac{\nabla^* [(1-\alpha)\bar{p}_l^*]}{(1-\alpha)} + \frac{1}{Re} \frac{\nabla^* \cdot [(1-\alpha)\bar{\tau}_\mu^*]}{(1-\alpha)} \\ &\quad - \frac{\nabla^* \cdot [(1-\alpha)\overline{\mathbf{u}^*\mathbf{u}^*}]}{(1-\alpha)} + \frac{1}{Fr} \hat{z} + \frac{2}{We(1-\alpha)} \overline{\kappa^* \nabla^* \chi_b} \\ &\quad - \frac{L_r \Phi_b}{\rho_l U_c^2 (1-\alpha)} \end{aligned} \quad (4.13)$$

In the above equation, the viscous stress term is removed by the assumption ④ ( $Re_c$  calculated from the experimental data is the order of  $10^4$ , see table 4.1), and the surface tension term can be neglected considering the  $We$  of the present study (table 4.1 in the manuscript). Also, the gravity term is a constant, which means that it does not affect the scaling relation between the liquid statistics and the  $\Phi_b$ , so it can be ignored.

By combining equation (4.12) and the  $z$ -direction component of the above equation and apply the assumption ①, we can get equation (4.14) in a conservative form (with the dimensional form).

$$\begin{aligned} &\frac{\partial}{\partial z} (1-\alpha) (U_z^2 + \overline{u'_z u'_z}) + \frac{1}{r} \frac{\partial}{\partial r} (1-\alpha) r (U_r U_z + \overline{u'_r u'_z}) + U_z^2 \frac{\partial(1-\alpha)}{\partial z} + U_r U_z \frac{\partial(1-\alpha)}{\partial r} \\ &= -\frac{\partial}{\partial z} \frac{(1-\alpha)\bar{p}_l}{\rho_l} - \Phi_{b,z} \end{aligned} \quad (4.14)$$

On the other hand, in the  $r$ -direction,

$$\begin{aligned}
& \frac{\partial}{\partial z} \left[ (1-\alpha) (U_r U_z + \overline{u'_r u'_z}) \right] + \frac{1}{r} \frac{\partial}{\partial r} \left[ (1-\alpha) r (U_r^2 + \overline{u'_r u'_r}) \right] - \frac{(1-\alpha) \overline{u'_\theta u'_\theta}}{r} \\
& = -\frac{\partial(1-\alpha) \bar{p}_l}{\partial r} - \Phi_{b,r}
\end{aligned} \tag{4.15}$$

Integrate either side as  $\int_r^{L_r} dr'$ , and apply ⑥.

$$\begin{aligned}
& \int_r^{L_r} \left[ \frac{\partial}{\partial z} \left\{ (1-\alpha) (U_r U_z + \overline{u'_r u'_z}) \right\} + \frac{(1-\alpha) U_r^2}{r'} + U_r U_z \frac{\partial(1-\alpha)}{\partial z} + U_r^2 \frac{\partial(1-\alpha)}{\partial r'} \right] dr' \\
& - (1-\alpha) (U_r^2 + \overline{u'_r u'_r}) = -\frac{1}{\rho_l} \left[ (1-\alpha) \bar{p}_l \right]_r^{L_r} + \int_r^{L_r} \left[ \overline{\sigma \kappa \frac{\partial \chi_b}{\partial r'}} - \Phi_{b,r} \right] dr'
\end{aligned} \tag{4.16}$$

In addition, take partial differentiation with respect to  $z$  and apply ⑤,

$$\begin{aligned}
\frac{1}{\rho_l} \frac{\partial(1-\alpha) P}{\partial z} &= \frac{1}{\rho_l} \frac{\partial P_\infty}{\partial z} - \frac{\partial}{\partial z} \left\{ (1-\alpha) (U_r^2 + \overline{u'_r u'_r}) \right\} - \int_r^{L_r} \frac{\partial}{\partial z} \left[ \overline{\sigma \kappa \frac{\partial \chi_b}{\partial r'}} - \Phi_{b,r} \right] dr' \\
& + \int_r^{L_r} \left[ \frac{\partial^2}{\partial z^2} \left\{ (1-\alpha) (U_r U_z + \overline{u'_r u'_z}) \right\} + \frac{\partial}{\partial z} \frac{(1-\alpha) U_r^2}{r'} \right. \\
& \left. + \frac{\partial}{\partial z} \left\{ U_r U_z \frac{\partial(1-\alpha)}{\partial z} + U_r^2 \frac{\partial(1-\alpha)}{\partial r'} \right\} \right] dr'
\end{aligned} \tag{4.17}$$

and put (4.17) into (4.14).

$$\begin{aligned}
\frac{\partial}{\partial z} (1-\alpha) (U_z^2 - U_r^2 + \overline{u'_z u'_z} - \overline{u'_r u'_r}) & + \frac{1}{r} \frac{\partial}{\partial r} (1-\alpha) r (U_r U_z + \overline{u'_r u'_z}) + U_z^2 \frac{\partial(1-\alpha)}{\partial z} \\
& + U_r U_z \frac{\partial(1-\alpha)}{\partial r} = \int_r^{L_r} \frac{\partial}{\partial z} \left[ \overline{\sigma \kappa \frac{\partial \chi_b}{\partial r'}} - \Phi_{b,r} \right] dr' + \overline{\sigma \kappa \frac{\partial \chi_b}{\partial z}} - \Phi_{b,z} \\
& - \int_r^{L_r} \frac{\partial^2}{\partial z^2} \left\{ (1-\alpha) (U_r U_z + \overline{u'_r u'_z}) \right\} dr' - \int_r^{L_r} \frac{\partial}{\partial z} \frac{(1-\alpha) U_r^2}{r'} dr' \\
& - \int_r^{L_r} \frac{\partial}{\partial z} \left\{ U_r U_z \frac{\partial(1-\alpha)}{\partial z} + U_r^2 \frac{\partial(1-\alpha)}{\partial r'} \right\} dr'
\end{aligned} \tag{4.18}$$

From equation (4.12),  $U_c/L_z \sim U_r/L_r$ . Also, from figure S1, we can find that  $O(U_r/U_c) \sim 0.01$  whereas,  $O(U_{z,rms}/U_c) \sim 0.1$ ,  $O(U_{r,rms}/U_c) \sim 0.1$ . Therefore,  $U_r^2$  term can be ignored in (4.18). The order of magnitude of each term is as follows.

$$\frac{U_c^2}{L_z}, \frac{U_c^2}{L_z}, \frac{U_c^2}{L_z}, \frac{U_c^2}{L_z}, \frac{U_c^2}{L_z}, \frac{U_c^2}{L_z} \alpha, \frac{U_c^2}{L_z} \alpha, \frac{L_r}{L_z} \Phi_{b,r}, \Phi_{b,z}, \frac{U_c^2}{L_z} \left( \frac{L_r}{L_z} \right)^2 \alpha, \frac{U_c^2}{L_z} \left( \frac{L_r}{L_z} \right)^2 \alpha,$$

$$\frac{U_c^2 \left(\frac{L_r}{L_z}\right)^2}{L_z} \alpha, \frac{U_c^2 \left(\frac{L_r}{L_z}\right)^2}{L_z} \alpha, 0.1 \frac{U_c^2 \left(\frac{L_r}{L_z}\right)^2}{L_z}$$

Consequently, (4.18) is reduced to

$$\frac{\partial}{\partial z} \left\{ (1-\alpha) \left( U_z^2 + \overline{u'_z u'_z} - \overline{u'_r u'_r} \right) \right\} + \frac{1}{r} \frac{\partial}{\partial r} \left\{ (1-\alpha) r \left( U_r U_z + \overline{u'_r u'_z} \right) \right\} = -\Phi_{b,z} \quad (4.19)$$

The two terms on the left side have comparable order in a rough order of magnitude analysis. Therefore, it is necessary to compare the scales of  $\frac{\left( U_z^2 + \overline{u'_z u'_z} - \overline{u'_r u'_r} \right)}{L_z}$  and  $\frac{\left( U_r U_z + \overline{u'_r u'_z} \right)}{L_r}$  by considering more detailed data. The

actual value of  $\frac{\left( U_z^2 + \overline{u'_z u'_z} - \overline{u'_r u'_r} \right)}{U_c^2}$  and  $\frac{\left( U_r U_z + \overline{u'_r u'_z} \right) L_z}{U_c^2 L_r}$  was calculated from the

measured data and compared in figure 4.2. Note that we did not have cross-correlation between fluctuation components of radial and axial velocity, in this scaling comparison, we replaced it by multiplication of root-mean-squared velocities of it. The actual value of the cross-correlation is smaller than this (in Lai & Sokolofsky 2019,  $\overline{u'_r u'_z} \approx \frac{1}{3} u_{r,rms} u_{z,rms}$ ). Here,  $L_z/L_r$  is obtained as the ratio of the

plume radius to the height at the farthest downstream of the measured height. When comparing the center value as a representative value of each variable, the former was 2 to 5 times larger in the conventional bubble plume, and 1.5 times larger in the churn-turbulent bubble plume except the nearest point ( $z = 30$  mm) to the sparger. This simplifies the scaling relation as  $\frac{\partial}{\partial z} \left\{ (1-\alpha) \left( U_z^2 + \overline{u'_z u'_z} - \overline{u'_r u'_r} \right) \right\}$

$\sim -\Phi_{b,z}$ . At this point, please note that in the churn-turbulent bubble plume, the difference between the first and second terms is not significant. On the other hand, in bubble plume, because there is convective acceleration, so we have to consider the effects of the convective acceleration in interfacial momentum transfer term,  $\Phi_{b,z} \approx \Phi_{b,conv}$ . Therefore, we can have the final scaling relation.

$$\frac{U_z^2 + \overline{u'_z u'_z} - \overline{u'_r u'_r}}{U_c^2} \sim \frac{\alpha}{(1-\alpha)} \frac{V_R^2 + V_R U_c}{U_c^2} \quad (4.20)$$

It is noted that both the time-averaged and fluctuating velocities (including the radial components as well as the streamwise one) contribute to  $M_i$ , but the most important thing, compared with the relation for homogeneous bubble swarm flows (equations (4.14) and (4.15)), is the additional contribution of  $V_R U_c$  in  $I$ . As we have explained above,  $V_R U_c$  comes from the convective acceleration of relative bubble velocity,  $V_R$  (equation (4.7), (4.8)), which is critical to characterize the spatially evolving bubbly flow like the bubble plume.

In figure 4(a), we have shown the variation of the total liquid momentum parameter with the interfacial momentum parameter, which shows two dominant

correlations. One includes conventional bubble plume except for the highest position case and the results from churn-turbulent bubble plume in the lower region ( $z = 30$  mm, 50 mm). The other includes the rest cases. The former has a higher slope, which means that  $M_t$  is induced more easily by  $I$  compared to the later cases. This difference comes from the force coefficient corresponding to this system. As in section 4.3.1, because we don't know the exact functional expression of force coefficient in this system, we evaluated the empirical relation between  $M_t$  and  $I$ . Apart from  $Re_b$  and  $We_b$ , we additionally considered the Reynolds number based on the central velocity and the plume width ( $Re = U_c \delta / \nu$ , here,  $\delta = 2r_{1/2}$ ), and the averaged volume void fraction  $\langle \alpha \rangle$ , which is defined by the integration of  $\alpha$  in the plume area, because bubble plume consists of time-averaged plume flow with the additive agitation due to bubbles. As a result, we have figure 4(b) with a relation  $M_t \sim (I Re_b^2 We_b^{-2} Re^{-0.6} \langle \alpha \rangle^{-2})^{0.34}$ . The force coefficient is strongly correlated to  $Re_b$ ,  $We_b$ , and  $\langle \alpha \rangle$ , and has a relatively weak dependency on  $Re$ . For both types of bubble plumes, despite its clear difference in turbulence characteristics (figure 4.3(c)), interestingly, the results collapse into a single curve. For now, there is room for improvement in this relation, such as we need more data with different volume flow rates.

#### 4.4 Concluding remarks

In the present study, we have suggested an analytical approach to characterize the bubble-induced turbulence and validated its universal applicability for different types of bubbly flows of homogeneous bubble swarm (with and without prescribed background turbulence), bubble plume, and upward turbulent pipe flow. The comprehensive data for these flows were obtained by our own experiments or adopted from those available in the literature. The main strategy of the present approach is establishing a simple relation from the governing equation (i.e., two-phase Navier-Stokes equation) by applying several assumptions appropriate to the system, resulting in the linear scaling relation between the interfacial momentum transfer parameters ( $I$ ) and total liquid momentum parameters ( $M_t$ ). Though a specific expression of  $M_t$  and  $I$  vary depending on the flow geometry, the fundamental essence is the same. That is,  $M_t$  represents the change in momentum (including turbulence stress) induced by imposed bubbles and  $I$  expresses the interfacial momentum transferred by an interaction between bubbles and the surrounding liquid. Accordingly,  $M_t$  is determined by the time-averaged liquid velocity and the root-mean-square liquid fluctuation velocities. Also,  $I$  is a function of bubble relative velocity and the characteristic velocity of the background liquid shear rate. For each bubbly flow, the detailed formulation of  $M_t$  and  $I$  needs to be modified to address the important characteristics of bubble-induced agitation specific to the bubbly flow, such as the spatially varying (non-uniform) flow statistics and confinement (wall) effect. As a result, it was successfully shown that the linear correlation between two global parameters defined in the present studies applies to the bubble-induced turbulence (both enhancement and suppression) obtained in a wide range of flow geometries and conditions, which was not possible by the previous models that are valid for a specific condition. While characterizing the contribution of bubbles in the homogenous bubble swarm (with or without prescribed turbulence), we additionally confirmed that the bubble

parameter, previously devised to explain the liquid turbulence modulation due to bubbles, is a limiting case of the present interfacial momentum transfer parameter at the very small void fraction.

The most important thing in the proposed methodology is to determine the dominant contributions in the interfacial momentum transfer term, properly representing the nature of interfacial forces acting on the liquid surrounding the bubble, depending on the bubbly flow system. In addition, it is critical to find the characteristic velocity and length scales involved, which can adequately address the origins of flow turbulence (agitation) in determining the parameters of  $M_t$  and  $I$ .

Furthermore, we suggested an empirical relation that relates  $M_t$  and  $I$  in a single collapsed curve. Unfortunately, the dependence of each relation on a particular parameter is somewhat arbitrary now. To explain this in more detail, it is necessary to address the accurate force coefficient model based on detailed dynamics of the bubble-liquid interaction. While the scaling parameters devised in the present study showed a promising result such that they can be used to characterize how the conditions of bubbles determine the bubble-induced turbulence universally irrespective of the existence of background liquid-phase flow (turbulence) and the confining wall, we think that they can be extended to other types of the multiphase flow, such as the particle (or droplet) laden flow, in which the turbulence modulation by the dispersed phase is still a very important issue.

TABLE 4.1. Flow conditions of various bubbly flows characterized with the scaling relation developed in the present study:  $\langle \overline{d_b} \rangle$ , bubble size;  $\langle \alpha \rangle$ , volume void fraction;  $Re_b (= V_R \langle \overline{d_b} \rangle / \nu)$ , bubble Reynolds number;  $Re (= U_c 2L_c / \nu)$ , liquid-phase Reynolds number (in the case of bubble plume,  $L_c = L_r$  and for the bubbly pipe flow,  $Re$  is the bulk Reynolds number before the bubble injection);  $We_b (= \rho V_R^2 \langle \overline{d_b} \rangle / \sigma)$ , bubble Weber number;  $We (= \rho U_c^2 L_c / \sigma)$ , Weber number based on liquid-phase scales;  $Fr (= U_c^2 / g L_c)$ , Froude number. Here,  $< >$  and the overbar denotes spatial and temporal average respectively, and  $U_c$  and  $L_c$  is the characteristic velocity scale and length scale of the liquid phase, respectively. Without any comment,  $L_c$  is  $L_z$  for the bubble plume and  $L_r$  for the bubbly pipe flow.

Flow geometry	References	$\langle \overline{d_b} \rangle$ [mm]	$\langle \alpha \rangle$ [%]	$Re_b$	$Re$	$We_b$	$We$	$Fr$
Homogeneous bubble swarm	Lance & Bataille (1991)	5.0	0 – 3.0	1190	-	4.0	-	-
	Martínez-Mercado <i>et al.</i> (2007)	1.4 – 2.5	0.3 – 9.8	420 – 520	-	4.0	-	-
	Riboux <i>et al.</i> (2010)	1.6 – 2.5	0.5 – 4.3	450 – 800	-	1.8 – 3.5	-	-
	Mendez-Díaz <i>et al.</i> (2013)	1.7 – 3.7	0.5 – 6.0	340 – 960	-	1.0 – 3.5	-	-
	Lee & Park (2020)	3.5	0.6 – 1.1	330 – 670	-	0.3 – 1.7	-	-
Rising bubbles under the prescribed grid turbulence	Lance & Bataille (1991)	5.0	0 – 3.0	1190	-	4.0	-	-
	Almérás <i>et al.</i> (2017)	2.0 – 3.6	0.25 – 0.93	600 – 900	-	1.8 – 7.1	-	-
Bubble plume	The present study	4.6	2.2 – 17.1	310 – 2300	36000 – 65000	0.3 – 16.5	140 – 210	0.3 – 0.8
		7.0	2.9 – 33.4	120 – 3100	15000 – 53000	0.2 – 18.8	70 – 150	0.3 – 3.8
Laminar bubbly pipe flow	Hosokawa & Tomiyama (2013)	2.6 – 3.6	0.2 – 1.3	320 – 700	900	0.5 – 2.0	0.3	0.02
	Kim <i>et al.</i> (2016)	2.2 – 3.7	0.05 – 0.64	230 – 1000	750	0.6 – 3.2	0.1	0.002
Turbulent bubbly pipe flow	Lee <i>et al.</i> (2021)	3.9 – 4.9	0.2 – 1.5	1100 – 2700	44000	5.4 – 30	342	6.3
	Shawkat <i>et al.</i> (2008)	3.1 – 6.3	1.1 – 14.3	1000 – 2400	37000-130000	3.8 – 15.0	45 – 954	0.03 – 0.7

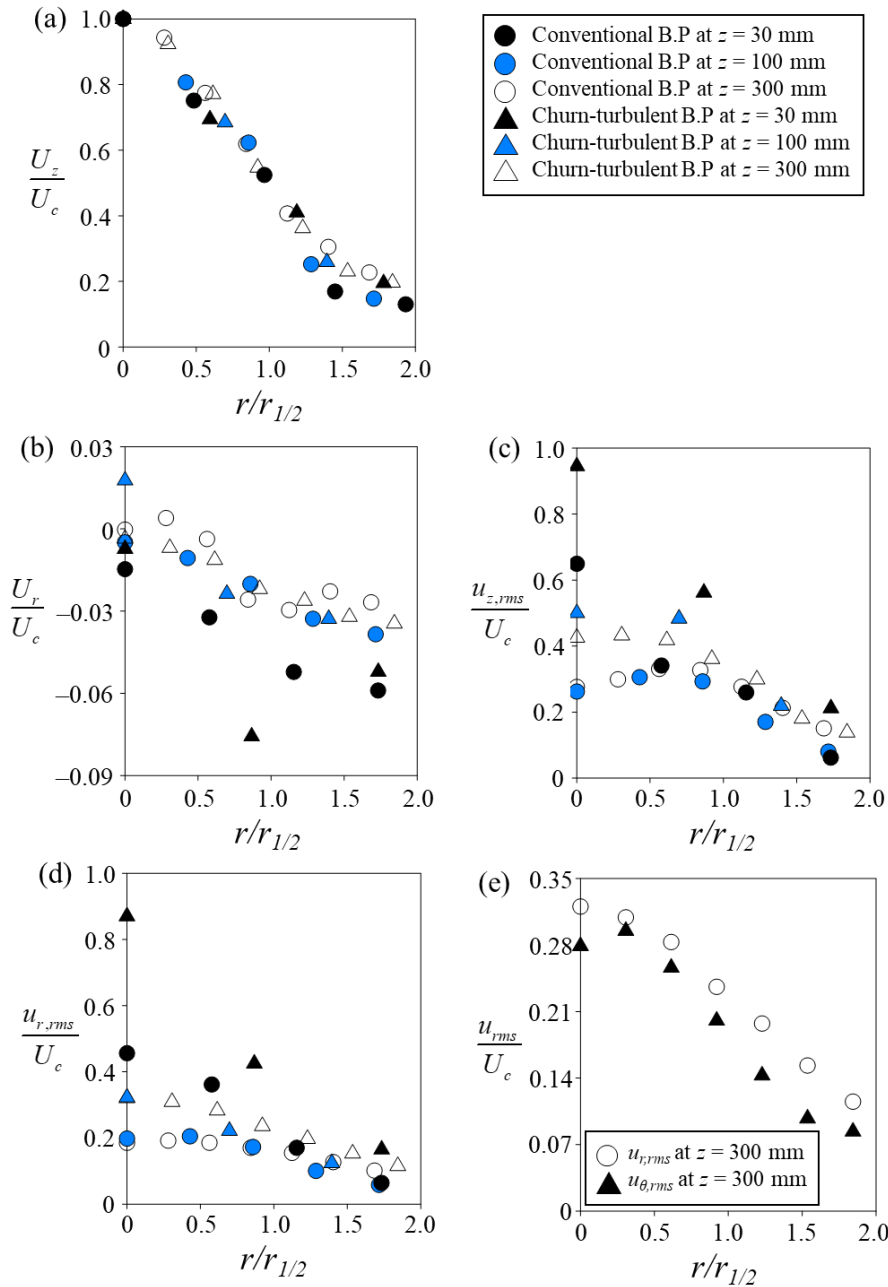


FIGURE 4.1. Induced liquid flow statistics in bubble plume, (a) averaged axial velocity, (b) averaged radial velocity, and (c) root-mean-square vertical fluctuation velocity, (d) root-mean-square radial fluctuation velocity and (e) root-mean-square radial and azimuthal fluctuation velocity normalized by the plume central velocity  $U_c$  and a half of the full width half maximum of  $U_z$ ,  $r_{1/2}$ .

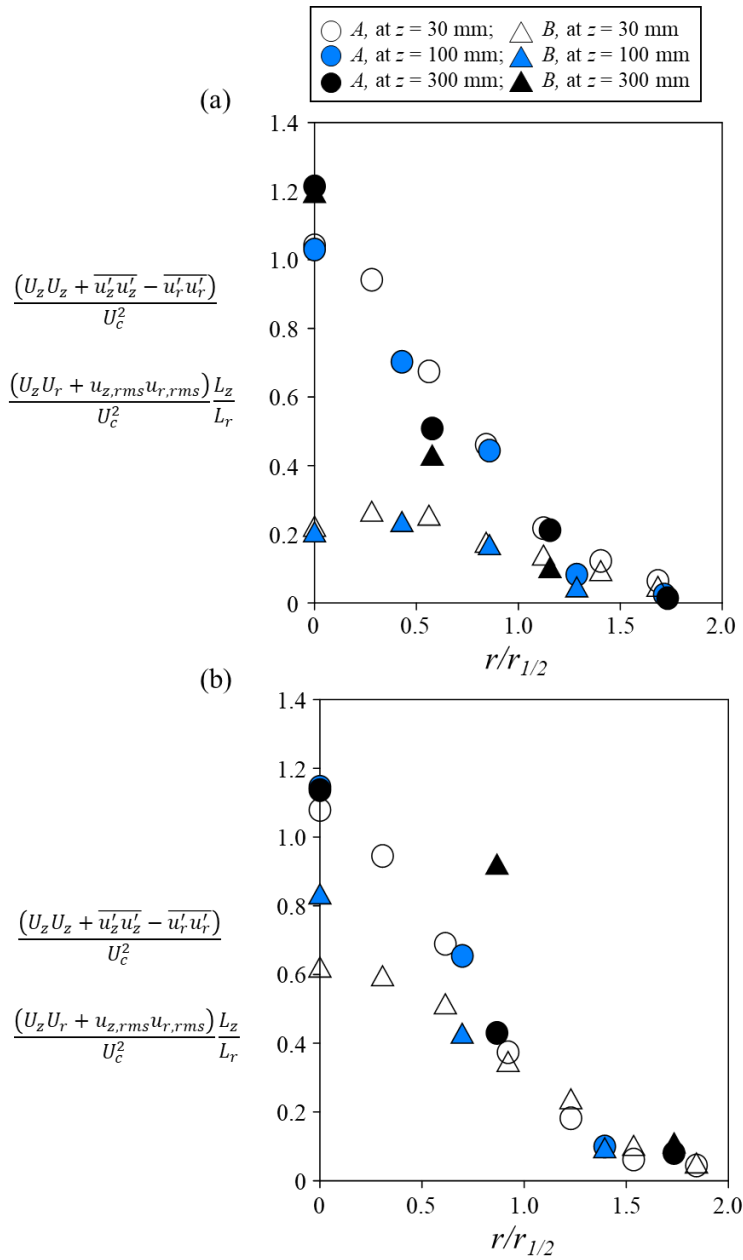


FIGURE 4.2. Scale comparison of  $A$  ( $(U_z U_z + \overline{u'_z u'_z} - \overline{u'_r u'_r}) / U_c^2$ ) and  $B$  ( $((U_z U_r + u_{z,rms} u_{r,rms}) / U_c^2) \cdot L_z / L_r$ ) in the case of (a) conventional bubble plume and (b) churn-turbulent bubble plume.

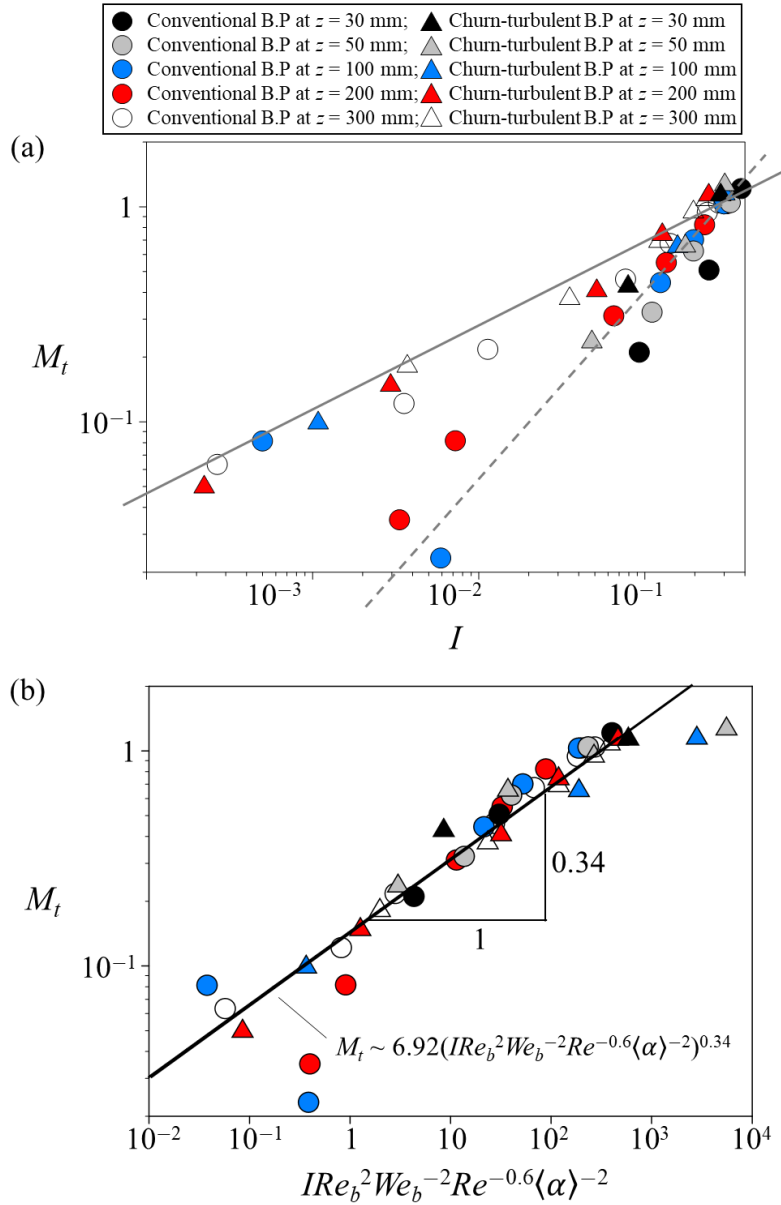


FIGURE 4.3. In the case of the bubble plume, total liquid momentum parameter ( $M_t = (U_z^2 + \overline{u'_z u'_z} - \overline{u'_r u'_r})/U_c^2$ ) as a function of (a) the interfacial momentum transfer parameter ( $I = \alpha/(1 - \alpha) \cdot (V_R^2 + V_R U_c)/U_c^2$ ) and (b) the interfacial momentum transfer parameter weighted by the bubble Reynolds number, the bubble Weber number, the Reynolds number (based on the central velocity and the plume width) and the averaged volume void fraction. In (b), the solid line is  $M_t = 6.92(IRe_b^2We_b^{-2}Re^{-0.6}\langle\alpha\rangle^{-2})^{0.34}$ .

## Chapter 5

# Stably stratified fluids mixing induced by bubble plume

### 5.1 Background

Bubble plume mixing is a commonly found system in nature and industry. It is a phenomenon that occurs over an extremely wide scale range from several  $\mu\text{m}$  to several kilometers (Boufadel *et al.* 2020). Furthermore, it is a multi-scale, multi-physics, and multi-phase phenomenon that various phenomena such as chemical reaction and phase change as well as hydrodynamic effect participate together. There is a lot of difficulty in accessing this bubble plume mixing numerically. Even recently studied research is about a laboratory scale ( $\sim O(1\text{m})$ ) using large eddy simulation which models for a small scale contribution. Therefore, it is essential to closely observe and analyze the phenomenon through an experimental approach.

As such, the study of bubble plume mixing has been very important, but studies in a limited way (Asaeda & Imberger 1993; Seol *et al.* 2009; Lima Neto *et al.* 2016; Yang *et al.* 2016). Bubble plume mixing has been mainly investigated in two types of the density profile. One is a linear function and the other is a step function with respect to  $z$ . Also, there are two types of mixing patterns which are, falling and peeling type (according to Lima Neto *et al.* 2016, plume and fountain mode respectively). Most of the previous studies have been done on a peeling type for a linear density profile (Mcdougall 1978; Asaeda & Imberger 1993; Seol *et al.* 2009; Yang *et al.* 2016). Falling type mixing occurs when the liquid momentum induced by the bubble plume is relatively large compared to the gravitational force acting on the density difference. Heavy fluid is pulled up to the top of the bath along the bubble plume and then spreads down (figures 5.1-5.2). Peeling type mixing occurs when the liquid momentum induced by the bubble plume is relatively small compared to the gravitational force acting on the density difference (figure 5.3). In this chapter, we look at the stably stratified fluids mixing for three kinds of density differences (table 5.1) for the bubble plume discussed in chapter 3. The setup of this study covers both the falling type and the peeling type, and since the flow field information of the induced liquid plume in chapter 3 is accurately obtained, the scaling relation for the system mixing velocity is derived using these parameters.

### 5.2 Types of the mixing induced by bubble plume

For the two types of bubble plume (conventional bubble plume and churn-turbulent bubble plume) which are examined closely in chapter 3, experiments were performed at three density differences, and the time sequence of each experiment is summarized in figures 5.1-5.3. First, in the case of the smallest density difference ( $\Delta\rho/\rho_w = 0.016$ ), the heavy fluid entrained by the bubble plume reaches the air-water interface on the top of the bath and then falls to the outside of the bubble plume. It is shown that the conventional bubble plume is mixed faster than the churn-turbulent bubble plume. If the density difference is higher ( $\Delta\rho/\rho_w =$

0.037), the same change occurs at a slower rate, and at the highest density difference ( $\Delta\rho/\rho_w = 0.068$ ), the heavy fluid cannot follow the bubble plume and peeling is observed. In this case, as well, it was confirmed that the conventional bubble plume was mixed at a faster rate.

Figure 5.4 shows the observed mixing process schematically. The process is the same in the heavy fluid area for both falling and peeling. The heavy fluid is entrained by the bubble plume and rises, and the water-heavy liquid interface descends accordingly. When the lifted heavy liquid has enough momentum, it reaches the top of the bath and falls down to the periphery (falling type), and the case that it slips down and propagates to the periphery without reaching the top of the bath is called the peeling type.

It is important to predict this because the mixing speed and time of the light fluid (water in this case) vary depending on the mixing type. We defined the mixing type parameter,  $\Xi$  through a simple relationship as follows, and confirmed that the mixing type can be predicted using this (figure 5.5).

$$\Xi = \frac{\rho_w Q_b}{\Delta\rho \dot{m}(h_t)} \quad (5.1)$$

The definition of the mixing type parameter is simple. The buoyant force applied to the gas phase injected at the flow rate of  $Q_b$  (=6 lpm in the present study) is placed in the numerator, and the amount of momentum required to raise the fluid below is in the denominator. Finally, based on  $\Xi \approx 1$ , if it is less than 1, peeling occurs, and if it is greater than 1, falling occurs.

### 5.3 Mixing time

The most important thing in fluid mixing induced by bubble plume is probably the mixing time. It is a complex problem to completely describe how long fluids mixing takes as a result of numerous physical phenomena. We will first look at the trend of mixing time according to the key parameters defining the system and then propose a simple scaling relation.

From chapter 5.2, it can be seen that when stably stratified fluids are mixed by bubble plume, mixing proceeds relatively quickly in the upper layer where light fluid is initially located, and mixing takes longer as it goes down from the fluid interface. To quantify this, we define the local mixing time and plot it as a contour (figure 5.5). In the contour, the black box is the area that is mostly obscured by the bubble shadow, and the border indicated by the red solid line is an approximate representation of the width of the bubble plume. Also, the horizontal dashed line is the fluid boundary before bubble plume is applied. As expected, in all cases, it was confirmed that with the larger density difference, the mixing time becomes longer and the lower height took longer mixing time. In addition, churn-turbulent bubble plume showed a longer mixing time than conventional bubble plume. And it was confirmed that the local mixing time was shorter as the distance from the bubble plume was increased at the height belonging to the heavy fluid region.

The trend identified at the local mixing time is also observed at the global mixing time (figure 5.6). The greater the density difference and the further away from the bubble plume, the shorter the global mixing time, and the churn-turbulent

bubble plume had a longer global mixing time than the conventional bubble plume.

The reason why mixing speeds up as the distance away from the bubble plume increases can be explained by the factors that cause mixing. In the area close to the bubble plume, the lower fluid rises to the upper layer along the bubble plume by the entrainment of the bubble plume, and accordingly, the upper-lower layer interface sinks down. However, the area away from the bubble plume and close to the bath wall promotes mixing by adding not only the entrainment effect but also the circulating flow that is largely formed inside the bath. Accordingly, the further away from the bubble plume, the faster the mixing speed, and eventually, the degree to which this difference occurs is expected to have system dependency.

## 5.4 Mixing velocity

The sinking speed of the upper-lower layer interface ( $u_{low}$ ) is shown in [figure 5.8](#). Since the lower layer plays a key role in the mixing time of this system,  $u_{low}$  is defined as the mixing velocity. As mentioned in [section 5.3](#), the mixing time around the bubble plume is long and becomes shorter as it goes toward the wall, so  $u_{low}$  tends to be inversely proportional to this. The mixing time and  $u_{low}$  around the wall have a system dependency, so by averaging the global mixing time around the bubble plume (inside the red box but outside of the black box), the representative global mixing time,  $\langle T_m \rangle_i$  and the mixing velocity,  $\langle u_{low} \rangle_i$ , was defined. Then,  $\langle T_m \rangle_i$  and  $H_{low}/\langle u_{low} \rangle_i$  were drawn and compared according to the density difference ([figure 5.9](#)). Here,  $H_{low}$  is the lower layer height.

$\langle T_m \rangle_i$  and  $H_{low}/\langle u_{low} \rangle_i$  show similar values and the error occurs for the largest density difference. This difference may due to the fact that  $u_{low}$  was treated as a constant even though it had a spatial distribution along the height. Looking at the  $z$ - $t$  contour shown in [figure 2.10](#), the slope corresponding to  $u_{low}$  slightly decreases with time. In this study, it is assumed that the slope is constant, so it is believed that an error occurred in this assumption.

## 5.5 Scaling relation on the mixing velocity

Since the source that generates  $u_{low}$  is entrainment, we defined the reference velocity  $u_{low,o}$  as follows. The mass flow rate at  $z = H_{low}$  is obtained with the definition of the mass flow rate derived in [chapter 3](#).  $A_{bath}$  is the bath bottom area and  $A_{plume}$  is the induced liquid plume cross-sectional area.

$$u_{low,o} = \dot{m}(H_{low}) / (A_{bath} - A_{plume}(H_{low})) \quad (5.2)$$

[Figure 5.10](#) shows the mixing velocity normalized with this reference velocity versus the density difference. Interestingly, as the density difference increases, the mixing velocity becomes slower compared to the reference velocity, and the churn-turbulent bubble plume has more decreased velocity. The dominant factor that determines the tendency of the mixing velocity is the competition between the gravitational force that stabilizes the fluid layer and the induced liquid momentum that provides the momentum in which the fluid layer mixes. There is a Froude number as a dimensionless number that has such a physical meaning, and we derive [figure 5.11](#) by defining the Froude number with the following definition.

$$Fr_U = \frac{U_c}{\sqrt{gR\Delta\rho/\rho_w}} \quad (5.3)$$

Here,  $R$  is the induced liquid plume radius ( $R = 2r_{l2}$ ). As the  $Fr_U$  becomes smaller, it means that the gravitational force is greater than the induced momentum, and accordingly, the normalized mixing velocity becomes slower. And as the  $Fr_U$  increases, the induced momentum becomes dominant, so the normalized mixing velocity converges to 1.

What we found through chapters 3 and 4 is that the relationship between the gas phase and the liquid phase in the bubble plume is established between the interfacial momentum parameter and the total liquid momentum parameter. Therefore, if we redefine  $Fr$  as the gas phase parameter, it is straightforward to use  $\sqrt{V_R^2 + V_R U_c}$  an instead of  $U_c$ .

$$Fr_I = \frac{\sqrt{V_R^2 + V_R U_c}}{\sqrt{gR\Delta\rho/\rho_w}} \quad (5.4)$$

As shown in figure 5.10, scaling with  $Fr_I$  gives more aligned results than when scaling with  $Fr_U$ , and satisfies the following scaling relation:  $\langle u_{low} \rangle_i / u_{low,o} \sim Fr_I^{1.3}$ .

The reason why  $Fr_I$  is more aligned than  $Fr_U$  is that it contributes not only the mean momentum flow rate but also the turbulence momentum flow rate to the mixing velocity. Through the scaling relation proposed in this study, it can be confirmed that the interfacial momentum transfer parameter is very important not only in turbulence modeling but also in fluid mixing velocity (or, mixing time) modeling.

## 5.6 Concluding remarks

In this chapter, stably stratified fluids mixing induced by bubble plume was quantitatively analyzed. First, a bubble plume type and a mixing type that varies depending on the density difference were defined, and a quantitative parameter (ratio of buoyancy exerted on bubble plume to gravity acting on the heavier fluid element) was proposed. In addition, by examining the spatial distribution of the mixing time, the mixing characteristics of the system were identified, and a scaling relation for the mixing velocity, a factor that determines the global mixing time, was proposed. The normalized mixing velocity was scaled to the Froude number, but it was scaled well for the  $Fr_I$  defined as the characteristic velocity of the interfacial momentum transfer parameter.

TABLE 5.1. Mixing type depending on density difference and the bubble plume type

	$\Delta\rho/\rho_w = 0.016$	$\Delta\rho/\rho_w = 0.037$	$\Delta\rho/\rho_w = 0.068$
Conventioanl bubble plume	falling	falling	peeling
Churn-turbulent bubble plume	falling	falling	peeling

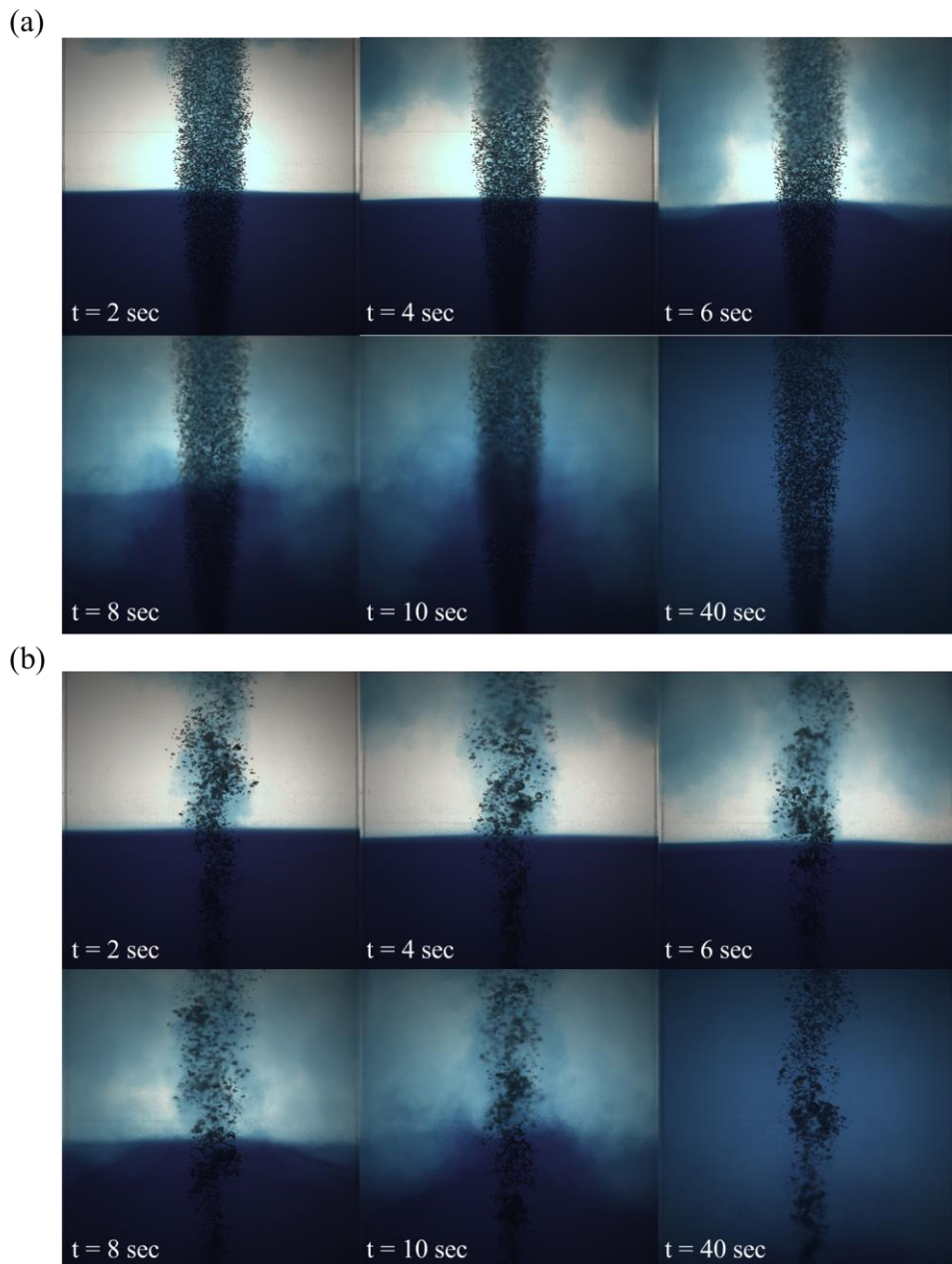


FIGURE 5.1. Stably stratified fluids mixing induced by (a) conventional bubble plume, and (b) churn-turbulent bubble plume when  $\Delta\rho/\rho_w = 0.016$ .

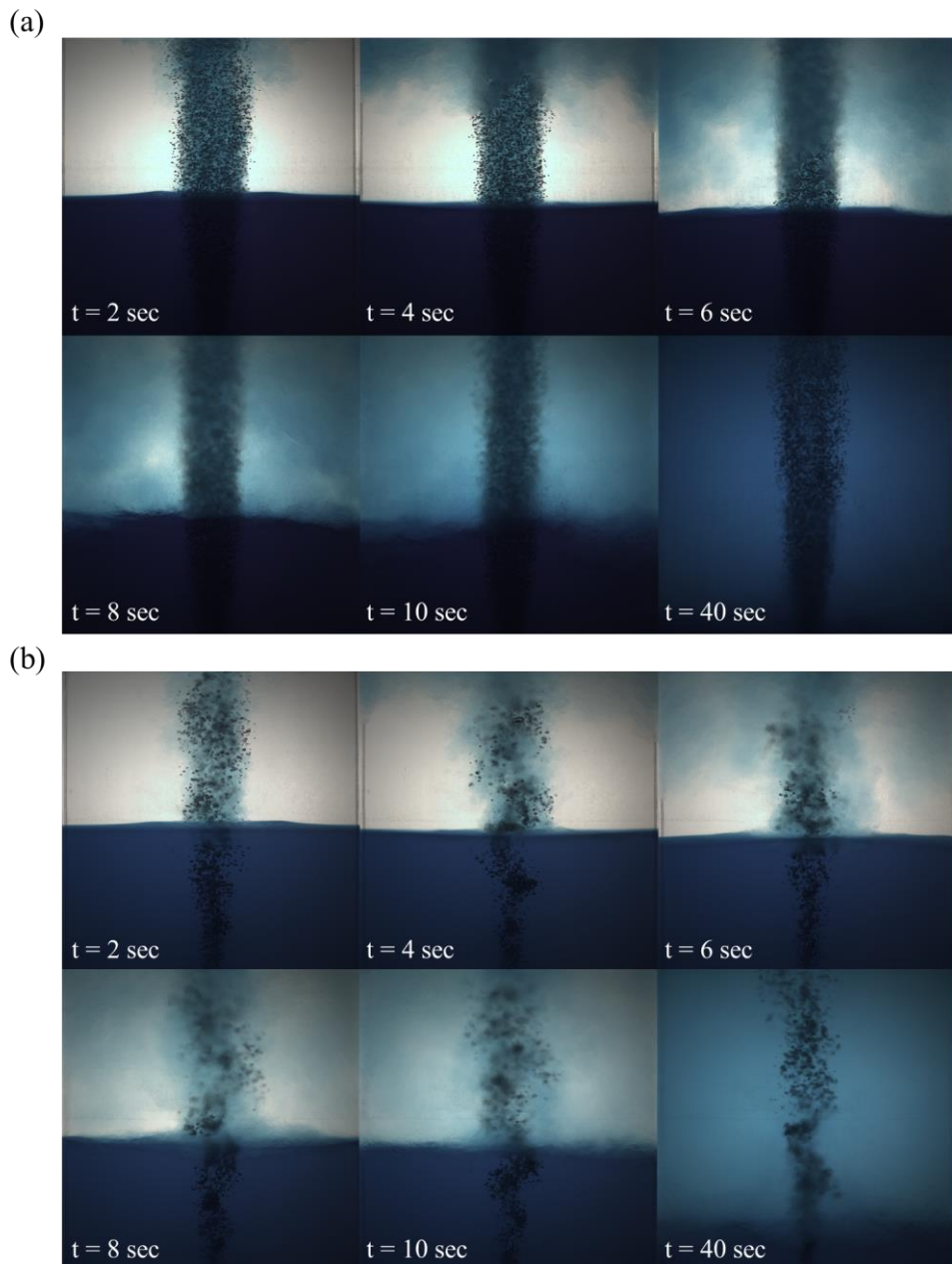


FIGURE 5.2. Stably stratified fluids mixing induced by (a) conventional bubble plume, and (b) churn-turbulent bubble plume when  $\Delta\rho/\rho_w = 0.037$ .

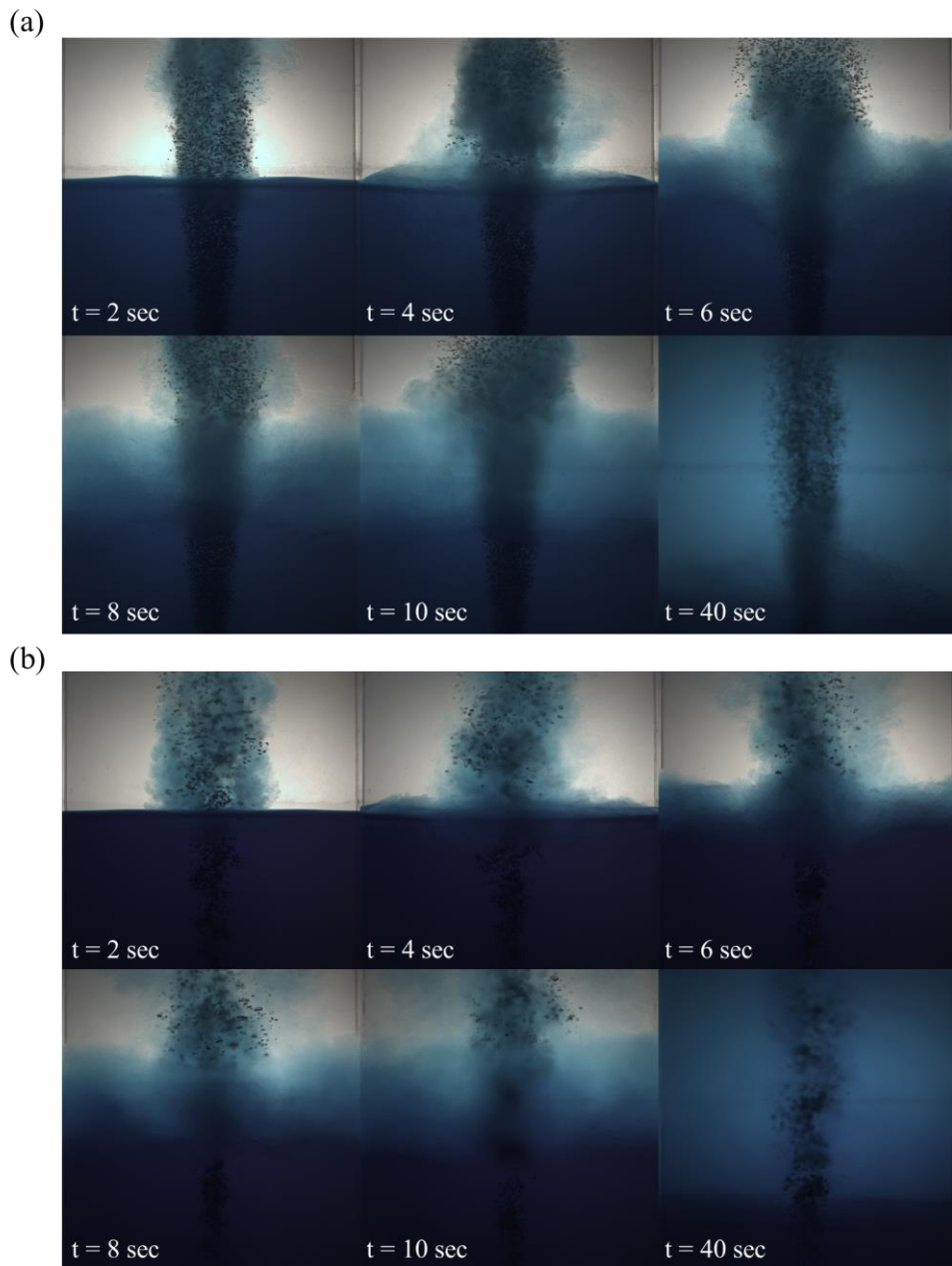


FIGURE 5.3. Stably stratified fluids mixing induced by (a) conventional bubble plume, and (b) churn-turbulent bubble plume when  $\Delta\rho/\rho_w = 0.068$ .

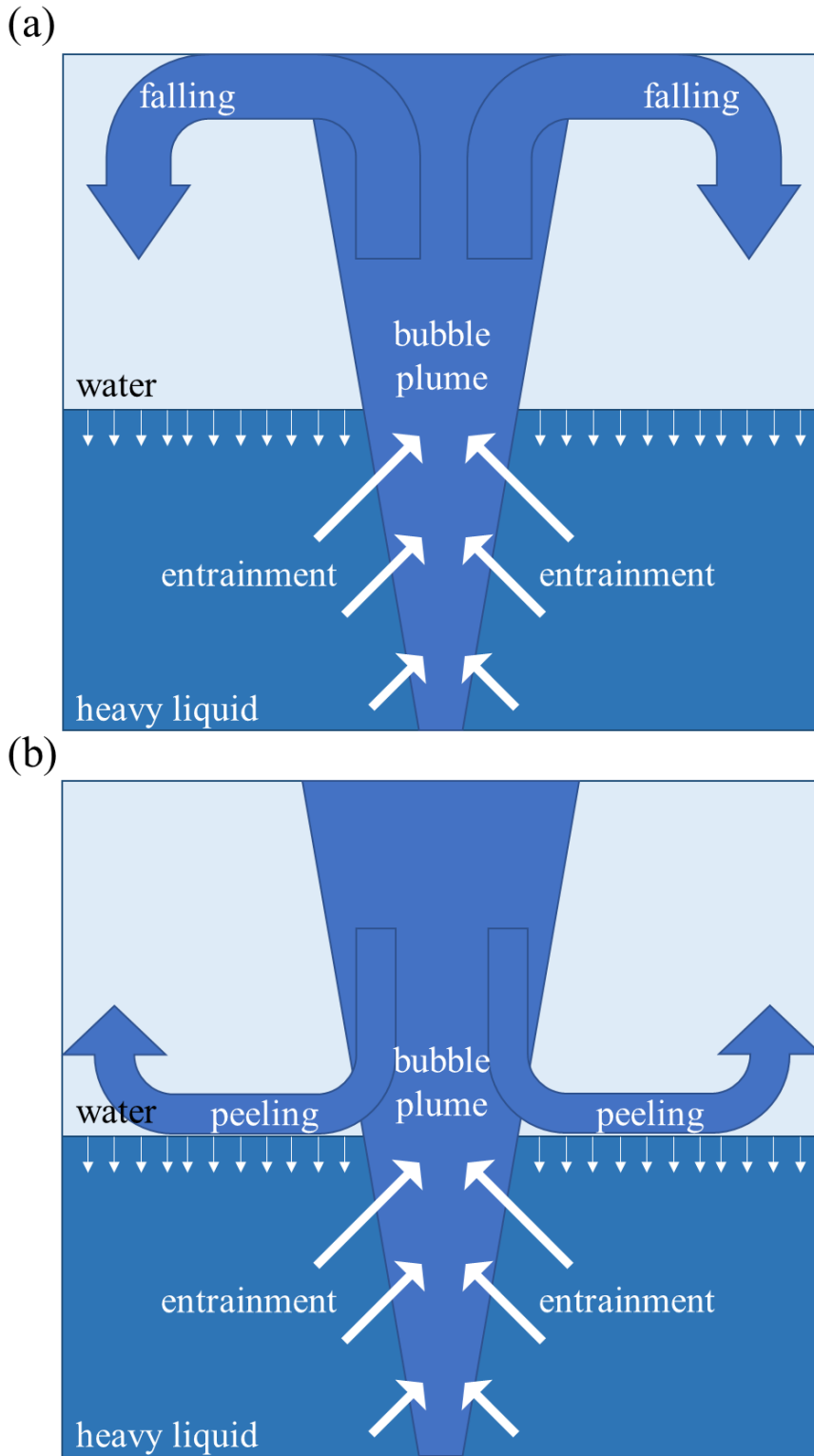


FIGURE 5.4. Schematics of mixing type. (a) Falling type. (b) Peeling type.

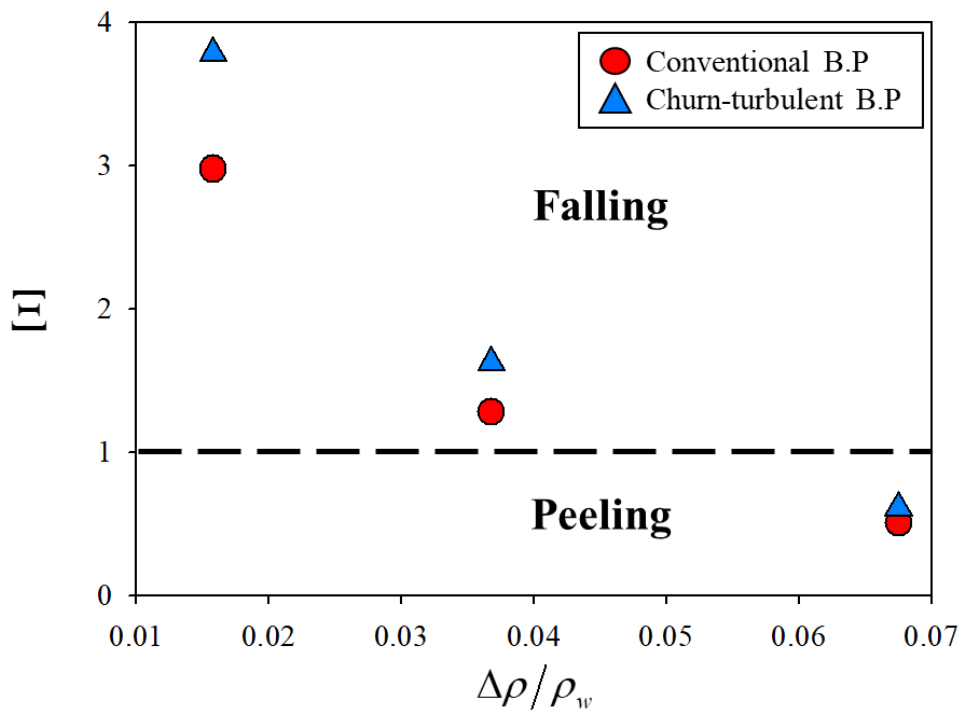


FIGURE 5.5. Mixing type parameter depending on the density difference

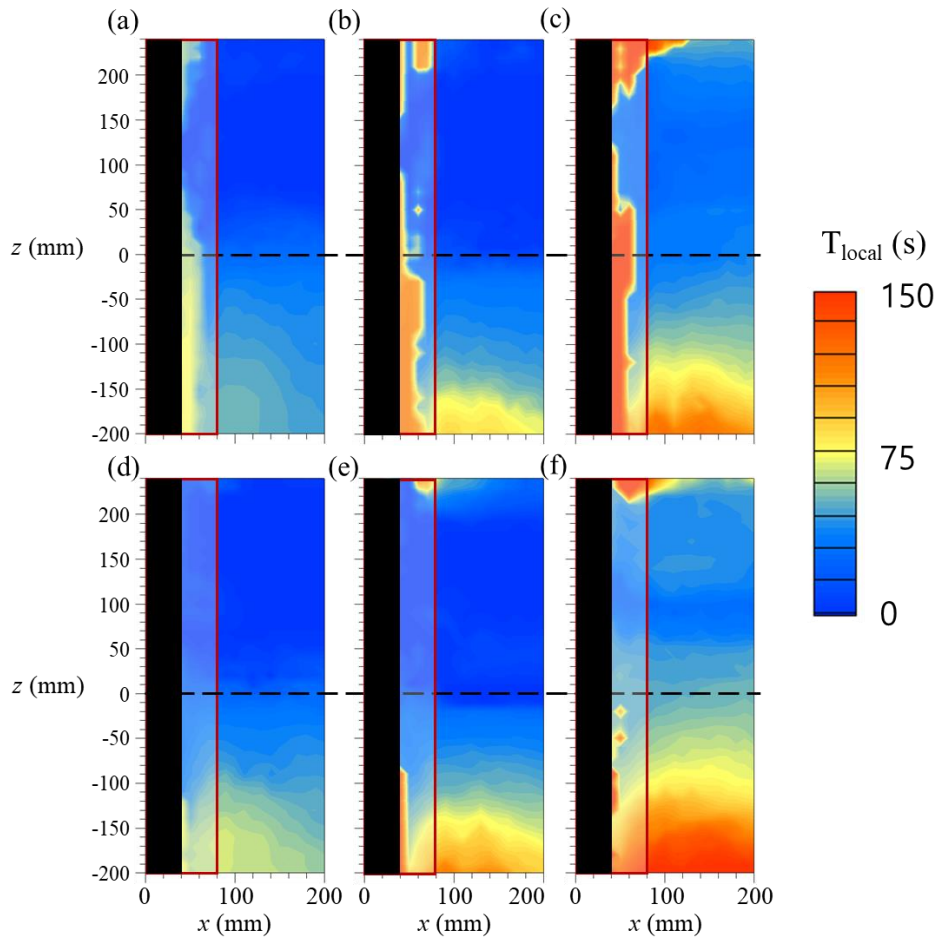


FIGURE 5.6. Local mixing time contour for conventional bubble plume ((a), (b), and (c)) and churn-turbulent bubble plume (d), (e), and (f). The density difference is (a), (d):  $\Delta\rho/\rho_w = 0.016$ , (b), (e):  $\Delta\rho/\rho_w = 0.037$ , and (c), (f):  $\Delta\rho/\rho_w = 0.067$ .

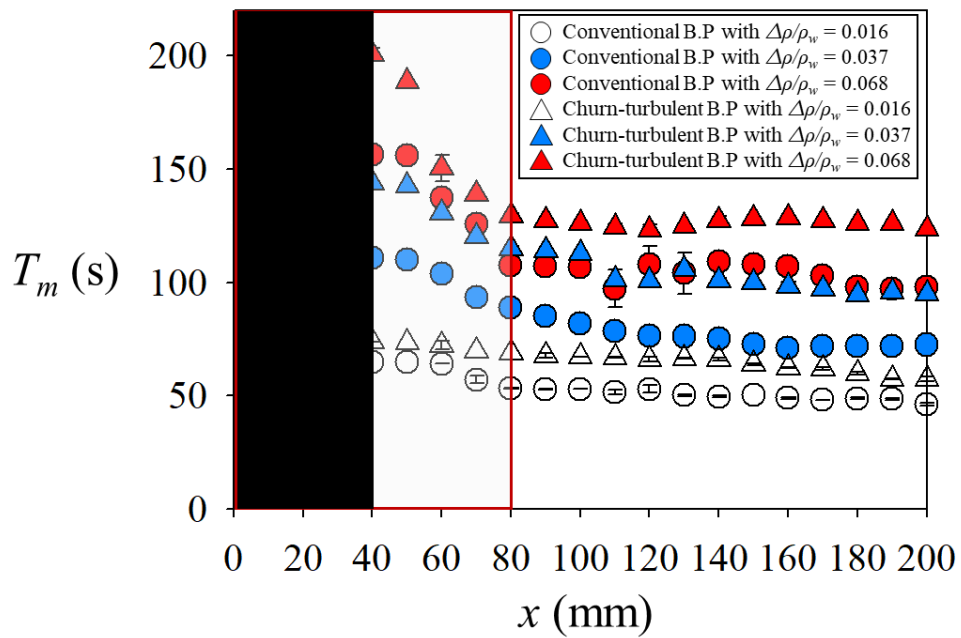


FIGURE 5.7. Global mixing time variation with  $x$

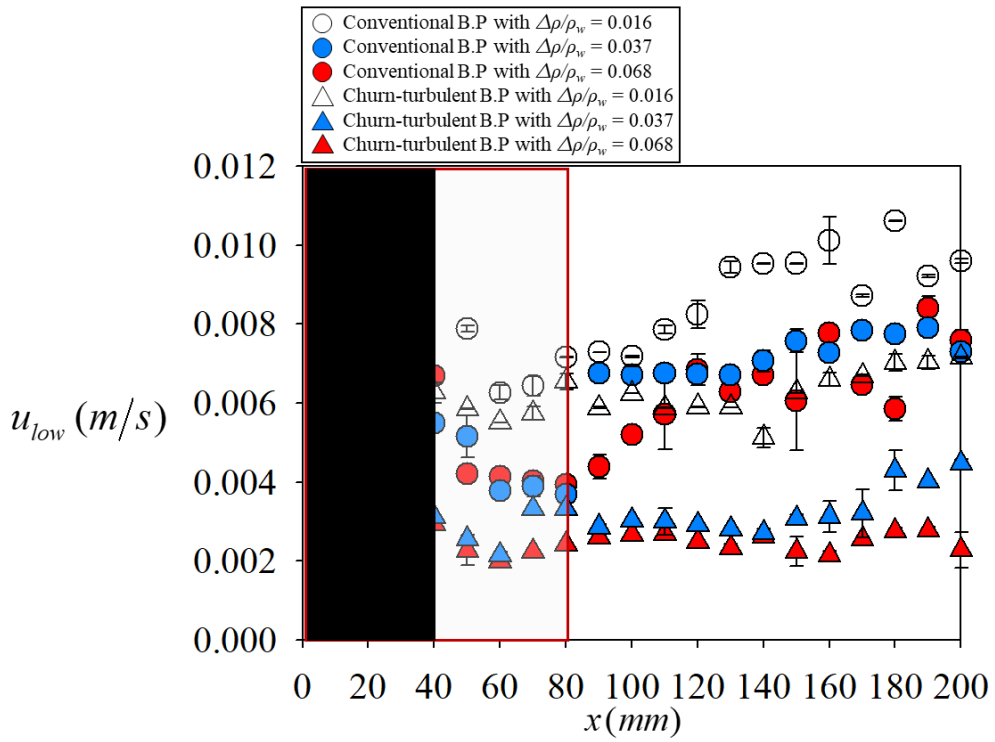


FIGURE 5.8. Mixing velocity variation with  $x$ .

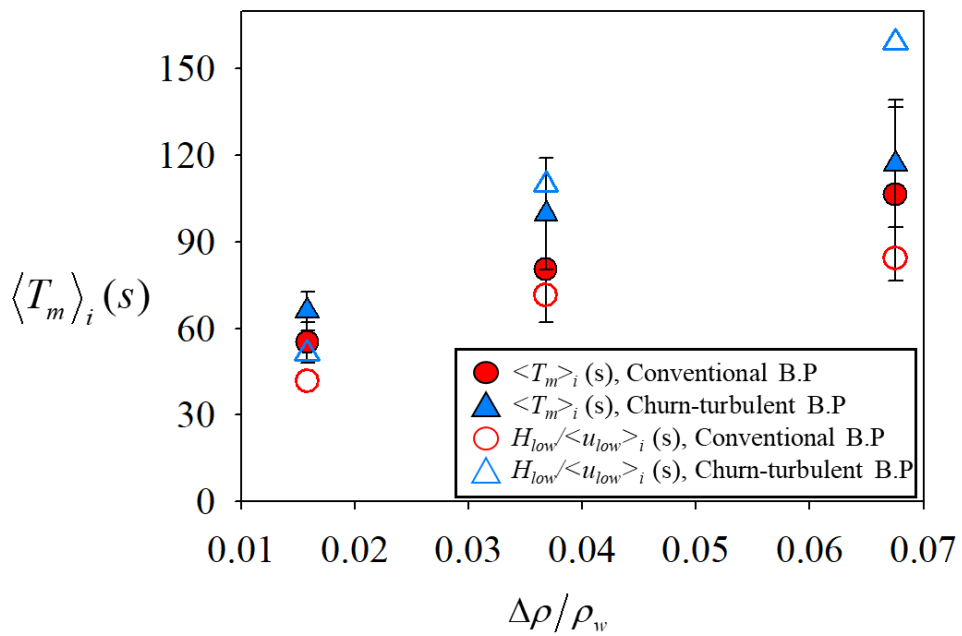


FIGURE 5.9. Global mixing time averaged inside the bubble plume with respect to difference difference.

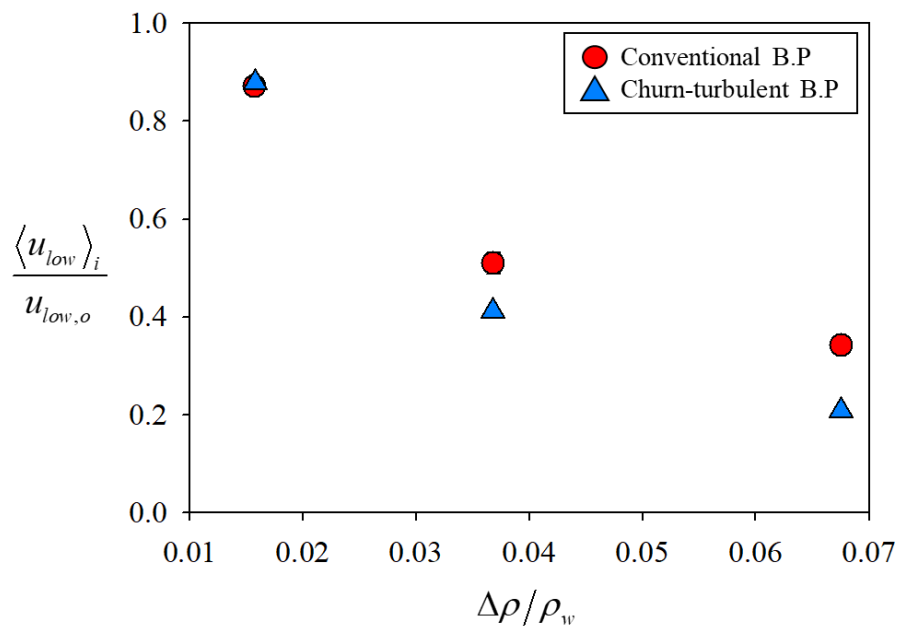


FIGURE 5.10. Mixing velocity averaged inside the bubble plume with respect to difference difference.

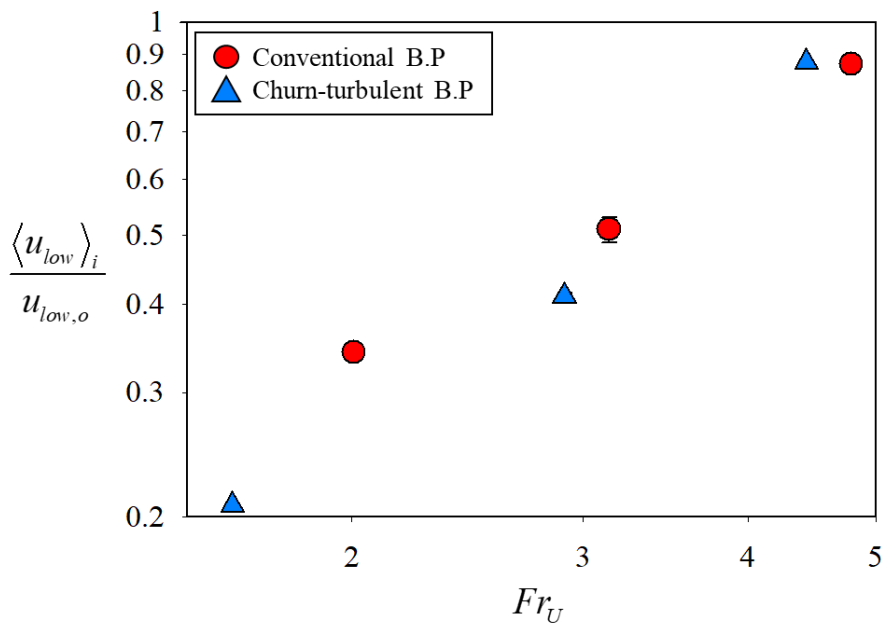


FIGURE 5.11. Mixing velocity averaged inside the bubble plume scaled with the Froude number based on the liquid central velocity.

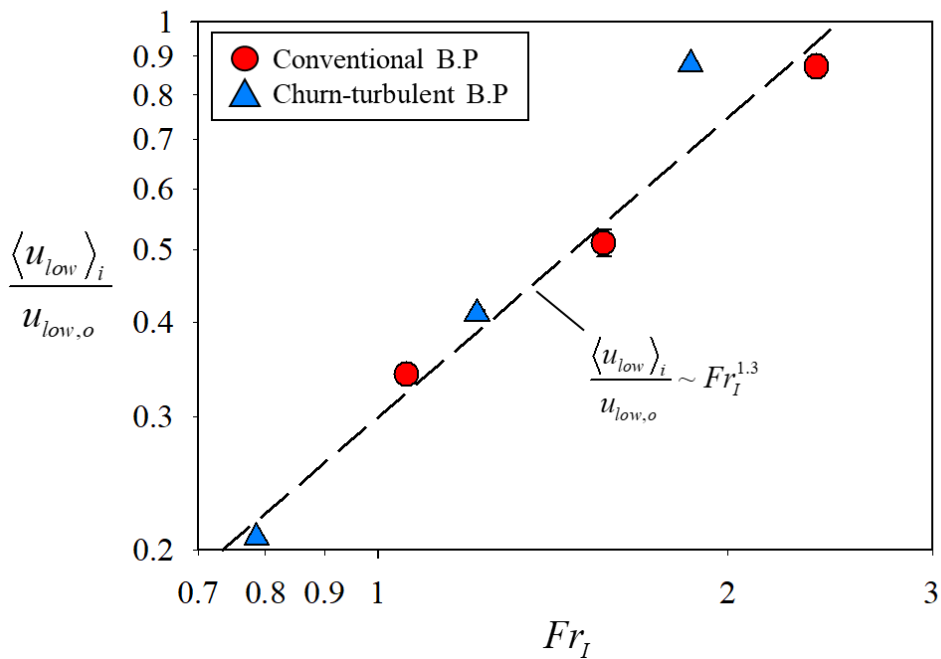


FIGURE 5.12. Mixing velocity averaged inside the bubble plume scaled with the Froude number based on the interfacial momentum transfer parameter.

# Chapter 6

## Conclusion

In this study, the fluid mixing induced by bubble plume, which is very important academically and industrially, was experimentally and theoretically analyzed. First, in order to thoroughly elaborate the unsteady characteristics of the bubble plume, gas and liquid phase information is quantitatively measured using a high precision measurement technique, and these are analyzed by dividing into bubble plume kinematics, gas and liquid phase dynamics, and then the characteristic length governing the system and velocity scales were determined. In addition, using these tools, time-averaged flow, turbulence statistics, and mixing velocity that vary according to the bubble plume regime were analyzed, and a scaling relation was proposed to explain the relationship between them.

First of all, the bubble plume regime is determined by the confinement parameter (ratio of tank height to sparger diameter) and superficial velocity. In this study, conventional bubble plume and churn-turbulent bubble plume were investigated at the volume flow rate  $Q_b = 6$  lpm.

Bubble plume kinematics were well scaled to  $r_{1/2}$  in the radial direction and  $D_m$  in the vertical direction. Through this, it was confirmed that the adjustment region and the asymptotic region were clearly distinguished. In addition, all of the unsteady parameters except for the time-averaged width had a higher normalized value of the churn-turbulent bubble plume than the conventional bubble plume, that is, a relatively large value compared to the bubble plume width. Likewise, the central bubble relative velocity also clearly distinguished the adjustment and asymptotic regions and converged to the previously reported value of 0.2 m/s regardless of the bubble plume type.

Likewise, in the case of the liquid velocity field,  $r_{1/2}$  and  $D_m$  were characteristic length scales, and in the case of the velocity parameters, the time-averaged vertical central velocity  $U_c$  well-scaled the velocity statistics. In the case of conventional bubble plume and churn-turbulent bubble plume, there was a clear difference in turbulence statistics than in the time-averaged velocity field. The churn-turbulent bubble plume consistently had higher values than the conventional bubble plume in turbulence statistics, and interestingly, the second and third moments of the vertical velocity of the conventional bubble plume almost coincided with the single-phase jet.

In the entrainment coefficient, which is one of the important parameters defining the induced liquid plume, the two bubble plumes showed a difference. Surprisingly, the churn-turbulent bubble plume is the same as the entrainment coefficient reported in conventional bubble plumes with a low volume void fraction. But the conventional bubble plume had a lower entrainment coefficient. This suggests that the macroscopic parameters of the bubble plume (i.e., entrainment coefficient and normalized velocity variation) may vary depending on the volume void fraction.

In the case of the integrated mass and momentum flow rate of the induced liquid plume, the conventional bubble plume had high values, because the conventional bubble plume has a wider width. However, since the entrainment coefficient has a higher churn-turbulent bubble plume, further downstream, the churn-turbulent

bubble plume may have a larger mass and momentum flow rate. As for the total momentum flow rate, the conventional bubble plume had a larger value, but the turbulence to mean momentum flow rate ratio was higher in the churn-turbulent bubble plume.

The scalewise distribution of turbulence energy was investigated through the energy spectrum, and it was confirmed that the frequency of the energy bump in which spectral energy injection by the bubble occurs is determined near the integral time scale in both bubble plumes. This corresponds to a much larger scale (plume scale) than the frequency previously observed in the bubble swarm (Prakash *et al.* 2016; Alm eras *et al.* 2017). In addition, the energy bump was first observed at a lower height in the churn-turbulent bubble plume.

An important fact learned through experimental investigations is that the time-averaged flow of induced liquid plume, as well as turbulence statistics, are well described as large-scale parameters (such as,  $U_c$ ,  $r_{1/2}$ ,  $D_m$ , and  $T_l$ ). Also, the gas-liquid interaction, i.e. interfacial momentum transfer, is very important. Therefore, with the idea that liquid turbulence induced by bubble plume can be derived in a similar manner to the equation describing single-phase jet, break down the two-phase Navier-Stokes equation according to some assumptions to represent liquid turbulence. The scaling relation of the interfacial momentum transfer parameter consisting of the total liquid momentum parameter and the gas phase parameters was derived.

Prior to obtaining the scaling relation for the bubble plume, the simplest bubbly flow geometry, the bubble swarm that has been actively studied (Martinez-Mercado *et al.* 2007; Riboux *et al.* 2010; Mendez-Diaz *et al.* 2013), is analyzed and the scaling relation between the root-mean-square velocity of liquid agitation and the volume void fraction and bubble relative velocity was proposed. Through this, the previously suggested scaling relation (Riboux *et al.* 2010) was analytically justified. Also, the same analysis was performed on the situation where bubble swarm and grid turbulence exist together. The relation proposed by Alm eras *et al.* (2017) was theoretically derived.

Bubble plume is a more complex system that develops spatially compared to the bubble swarm, which was a homogeneous system. In particular, unlike the homogeneous bubbly flow in which only drag force had to be considered for interfacial momentum transfer, convective contribution (consists of virtual mass and basset history force) had to be additionally considered. For the bubble plume we were able to derive a relatively simple scaling relation thanks to the order of magnitude analysis.

Finally, a similar scaling analysis was applied on bubbly pipe flow where confinement by wall plays an important role. In the case of the fully developed pipe flow, the Navier-Stokes equation in the two-phase pipe flow was combined with that in the single-phase pipe flow in order to eliminate the pressure gradient in the vertical direction, and a scaling relation between the Reynolds shear stress change caused by the bubble and the interfacial momentum transfer parameter was derived.

Stably stratified fluids mixing induced by bubble plume was quantitatively analyzed through experiments (chapter 5) based on the understanding obtained through precise experiments and theoretical analysis (chapter 3-4), and important parameters and scaling relations were derived. Similarly, the mixing of stratified

fluids with three density differences was investigated for conventional bubble plume and churn-turbulent bubble plume. It was observed that there are two mixing types, and it was confirmed that criterion can be determined by the ratio of buoyancy, the momentum source of bubble plume, and the gravitational force stabilizing stably stratified fluids. The global mixing time, which means until all fluids are mixed, was defined to quantify the variation of mixing tendency depending on the bubble plume type and density difference. Naturally, the larger the density difference, the longer the global mixing time, and depending on the bubble plume type, it took longer in the churn-turbulent bubble plume.

The mixing velocity corresponding to the global mixing time was defined, and it was confirmed that it was well scaled by the Froude number. The definition of the Froude number was defined as the ratio of the bubble plume momentum and the gravitational force corresponding to the density difference. Interestingly, more aligned results were obtained when defined by gas-phase parameters than when defined by liquid mean velocity. This is thought to be because, unlike mean velocity, turbulence contribution can also be considered when both convective and non-convective components are considered in gas-phase parameters.

The analysis and theoretical relations proposed in this study are expected to be useful in understanding and operating bubble-induced turbulence and fluid mixing induced by bubble plume academically and industrially.

Finally, this paper concludes with a summary of the issues left on fluid mixing induced by bubble: (i) the effect of surface tension on turbulence characteristics and fluid mixing of bubbly flow, (ii) the effect of viscosity on turbulence characteristics and fluid mixing of bubbly flow, (iii) entrainment coefficient as a function of volume void fraction and bubble plume type, (iv) global mixing time and mixing velocity depending on the fluid interface height. In this study, since we dealt with the low Weber number cases, the surface tension effect was not considered, but in the spatially developing flow, the surface tension effect should be considered in the high Weber number condition. In addition, because one of the major applications of bubble-induced mixing is high viscosity liquid mixing, it is necessary to consider the viscosity effect. Moreover, as a result of the observation of this study, it was concluded that the entrainment coefficient may change depending on the volume void fraction, unlike the previous premise that the bubble plume entrainment is constant. Therefore, it is necessary to study the entrainment coefficient in both bubble plume types for a wide volume void fraction. Lastly, this study conducted a mixing experiment for only one fluid interface height. Because the entrainment coefficient is different, the relationship between the mass and momentum flow rate of the induced liquid plume will vary according to the height, so a study on this is also necessary.

# Chapter 7

## Appendix

### 7.1 Relation between total liquid momentum and interfacial momentum transfer for various bubbly flows

#### 7.1.1 Homogeneous bubble swarm

Let us start with the homogeneous bubble swarm, possibly the simplest form of a bubbly flow, in which bubbles in a uniform distribution are introduced to a liquid without a prescribed movement (Martínez-Mercado *et al.* 2007; Riboux *et al.* 2010; Mendez-Diaz *et al.* 2013). Thus, in a homogeneous bubble swarm, we do not have an average shear rate, pressure gradient, and void fraction gradient in the liquid-phase flow. Considering this, in the steady-state condition, equation (4.3) is further arranged as:

$$0 = -\nabla \cdot [\overline{u'u'}] + g - \frac{1}{(1-\alpha)\rho_l} \Phi_b \quad (7.1)$$

Since the gravitational acceleration,  $g$ , is constant, the scaling relation for the change of flow variables is eventually established between the first and third terms in the right-hand side of equation (7.1). For the interfacial momentum transfer, we only consider  $\Phi_{b,N\text{-conv}}$  in a homogeneous bubble swarm, because there is no convective acceleration in the liquid phase velocity field, resulting in equation (7.2) along the streamwise (vertical) direction.

$$\overline{u'_z u'_z} \sim - \frac{1}{(1-\alpha)\rho_l} \Phi_{b,N\text{-conv}} \quad (7.2)$$

Because the liquid flow is purely induced by the rising bubbles, the bubble size ( $\langle \bar{d}_b \rangle$ ) and velocity ( $V_b$ ) were chosen as characteristic length and velocity scales, respectively. With equation (4.6), then, the above scaling relation is arranged as:

$$\frac{\overline{u'_z u'_z}}{V_b^2} \sim \frac{\alpha}{1-\alpha} \frac{V_R^2}{V_b^2} \sim \frac{\alpha}{1-\alpha} \quad (7.3)$$

Here, it was further considered that the relative bubble velocity is the same as the bubble rise velocity as  $V_R = V_b - U_z \simeq V_b$  in this system, the time-averaged liquid velocity in the bubble swarm is 0.). From now on, let us name the right- and left-hand side of the resulting scaling relation, representing the dimensionless bubble-induced turbulence and interfacial momentum, respectively, as the total liquid momentum ( $M_t$ ) and the interfacial momentum transfer parameter ( $I$ ), respectively.

The above scaling relation explains that in the bubble swarm, the interfacial momentum transfer that determines the liquid momentum (from bubble-induced

fluctuation) is governed by the volume void fraction. This is a reasonable explanation of a bubble swarm, in which the only source of the flow disturbances is the rising bubbles, of which the uniform distribution makes the global parameter of a void fraction more important than the spatial (or temporal) variation of flow variables. Previously, Riboux *et al.* (2010) suggested the empirical relation of  $\overline{u'_z u'_z} / V_b^2 \sim \alpha$ , which approaches our result when  $\alpha \ll 1.0$ . Thus, we can say that our scaling relation is the analytical justification of their empirical relation. In figure 7.1(a), we have applied equation (7.2) for the bubble swarm data available in the literature (Lance & Bataille 1991; Martinez-Mercado *et al.* 2010; Riboux *et al.* 2010; Mendez-Diaz *et al.* 2013; Lee & Park 2020). As shown, the total liquid momentum parameter ( $M_t = \overline{u'_z u'_z} / V_b^2$ ) increases with the interfacial momentum transfer parameter ( $I = \alpha / (1 - \alpha)$ ), for the collected data. Lee & Park (2020) has higher  $M_t$  about an order compared to other cases. This discrepancy is owing to the fact that  $U_z$  has a finite value in Lee & Park (2020) unlike previous studies which disregarded the  $U_z$  as it has a negligible value compared to fluctuation velocity (Lance & Bataille 1991; Martinez-Mercado *et al.* 2010; Riboux *et al.* 2010; Mendez-Diaz *et al.* 2013). Therefore, in the case of Lee & Park (2020),  $I$  is defined as  $\alpha / (1 - \alpha) \cdot \overline{V_R^2} / V_b^2$  and it is clearly smaller than  $\alpha / (1 - \alpha)$ . It is hard to indicate the reason why the time-averaged vertical liquid velocity is non-zero in Lee & Park (2020) contrary to previous reports. We suppose that this difference may come from the measurement technique. Lee & Park (2020) used two-phase PIV while other studies measured the velocity data with Laser doppler anemometry (Riboux *et al.* 2010), hot-film anemometry (Martinez-Mercado *et al.* 2010; Mendez-Diaz *et al.* 2013), or both (Lance & Bataille 1991).

Currently, the universal drag coefficient (the coefficient between  $M_t$  and  $I$  in the statistically spatially homogeneous system) model is not available. So we empirically evaluated the coefficient between the relation (7.3). It is already known that the drag coefficient is a function of bubble Reynolds number and bubble shape. Because bubble shape is generally regarded as is represented by the bubble Weber number (or Eötvös number), we obtained the proportional constant as a function of  $Re_b$  and  $We_b$ . As a result, we established a relation,  $M_t = 2.74 \times 10^{-4} I Re_b^{1.4} We_b^{-0.6}$ . In figure 7.1(b), we can find that all cases agree well with the suggested relation. In the relation,  $M_t$  is linearly proportional to  $I$ , equivalently with the proposed empirical relation  $\overline{u'_z u'_z} / V_b^2 \sim \alpha$  (Riboux *et al.* 2010).

### 7.1.2 Rising bubbles under the prescribed grid turbulence

When the background turbulence in the liquid phase exists in the bubble swarm, now the source of flow agitation is not solely determined by the rising bubbles (Lance & Bataille 1991; Alméras *et al.* 2017). Similar to the homogeneous bubble swarm (section 7.1), it is still justified to assume that the average shear rate, and the gradients of the void fraction, and the pressure are neglected, and thus the equation (7.2) can be used, as well. Likewise, for the length scale, we use the averaged bubble size ( $\langle \overline{d_b} \rangle$ ) representing the bubble-induced agitation; however, the root-mean-squared fluctuation velocity of background liquid flow ( $u'_o$ ) is used as a velocity scale to address the contribution by background turbulence. As a

result, we obtain the following scaling relation from equation (7.2).

$$\frac{\overline{u'_z u'_z}}{u_o'^2} (= M_t) \sim \frac{\alpha}{1 - \alpha} \frac{V_R^2}{u_o'^2} (= I) \quad (7.4)$$

When the volume void fraction is quite small ( $\alpha \ll 1$ ), the present relation becomes  $\overline{u'_z u'_z}/u_o'^2 \sim \alpha V_R^2/u_o'^2$  which is the same as suggested by previous studies (Rensen *et al.* 2005; Alm eras *et al.* 2017). As we have discussed in section 4.1, the right-hand side of this relation is the bubble parameter, introduced to evaluate the ratio of the kinetic energy of bubbles to the turbulent kinetic energy in the background. Hence, it is possible to say that the bubble parameter is a specific form of the interfacial momentum transfer parameter or the present parameter set of  $M_t$  and  $I$  is more comprehensive.

In figure 7.2, we have plotted the variation of the total liquid momentum parameter ( $M_t = \overline{u'_z u'_z}/u_o'^2$ ) with the interfacial momentum transfer parameter ( $I = (\alpha V_R^2)/((1 - \alpha)u_o'^2)$ ), defined in equation (7.4). The two-phase flow data were adopted from Lance & Bataille (1991) and Alm eras *et al.* (2017), in which the bubble diameter ranges from 2.0 to 5 mm, the bubble Reynolds number was 600 – 1190, the bubble Weber number was 1.8 – 7.1 (see table 4.1) and the ratio of the background turbulence intensity to the bubble relative velocity ( $u'_o/V_R$ ) was 3 % – 16 % (see the legend in figure 7.2).

As shown in figure 7.2, it is clear that  $M_t$  is proportional to  $I$ . It agrees well with the empirically evaluated equation,  $M_t = 2.5I^{0.7}$ . Alm eras *et al.* (2017) reported that before  $b < 0.4$ ,  $\sqrt{M_t} \sim b^{0.4}$  and the exponent becomes 1.3 after  $b > 0.7$  (note that here,  $b$ 's the bubble parameter which has almost the same definition as  $I$  in this case). In figure 7.2, the slopes corresponding to those are 0.7 and 2.67 respectively. It is consistent that because Alm eras *et al.* (2017) suggested the slope for  $\sqrt{M_t}$  and it would be double for  $M_t$ .

Also, it seems that the case satisfying  $u'_o/V_R > 0.08$ , has a stiff increase in  $M_t$  along with  $I$  when  $I \geq 1$ . We suppose that there is a transition in the mechanism of interaction between bubble-induced agitation and the background turbulence. About this point, Alm eras *et al.* (2017) suggested that after  $b (\simeq I) \simeq 0.7$ , the bubble wake structure changes and it is responsible for the slope change of  $M_t$ . Specifically, they defined the bubble wake based on the conditionally averaged liquid fluctuation velocity behind the bubble. In their observation, the fluctuation velocity decays exponentially along with the distance from the rear side of the bubble. The decaying slope was divided into two regions, which are, the primary wake with a higher decaying slope and the secondary wake with a reduced slope. According to Alm eras *et al.* (2017), the length of the secondary wake increased when  $b > 0.7$ . As a result, the overall wake region increased. On the other hand, if we consider the data from Lance & Bataille (1991) together, we can see that the cases with  $u'_o/V_R < 0.08$  follow  $M_t \sim I^{0.7}$  even at  $I > 1$ . It implies that  $I \simeq 1$  (or 0.7) is not a sufficient condition for the mechanism change. We think that  $u'_o/V_R \simeq 0.8$  is another condition for the change of the interaction between the background turbulence and

the bubble-induced agitation. It is reasonable that the scale of the characteristic velocities needs to be similar within about an order to interact with each other. The physical mechanism underlying this transition is still obscure (Alm eras *et al.* 2017). There are several issues to understand the detailed mechanism causing the change in the proportionality between  $M_t$  and  $I$ , such as, ‘what triggers the secondary wake?’ (Alm eras *et al.* 2017) and ‘what is accompanying change in terms of vortex dynamics?’. A deepen understanding on these aspects makes more precise  $M_t$  model possible.

### 7.1.3 Upward bubbly pipe flow

Finally, we apply our approach to the upward bubbly pipe flow, in which the bubbly flow evolves inside the confined environment, i.e., with the existence of the wall, and thus the bubble-induced liquid-phase turbulence modulation occurs in the most complicated way. For both laminar and turbulent single-phase pipe (or channel) flow, the effect of rising bubbles has been vigorously studied so far (Shawkat *et al.* 2008; Hosokawa & Tomiyama 2013; Kim *et al.* 2016; Ma *et al.* 2017; du Cluzeau *et al.* 2019; Ma *et al.* 2020a; Ma *et al.* 2020b; Lee *et al.* 2021). For the relevant data available in the literature, the void fraction ranges 0.05 – 14.3 % and the Reynolds number of the single-phase (without bubbles) flow varies in 750 – 130000 (see table 4.1). Assuming that the upward bubbly flow in a pipe is fully developed, we derive the total liquid momentum parameter and the interfacial momentum transfer parameter, as shown in below.

In steady-state with the fully developed flow, from the continuity equation, we have  $\frac{\partial(1-\alpha)U_z}{\partial z} = -\frac{1}{r}\frac{\partial}{\partial r}r(1-\alpha)U_r = 0$ , and by considering no-slip condition,  $r(1-\alpha)U_r = 0$ . So, the axial component of the two-phase averaged Navier-Stokes equation becomes

$$0 = (1-\alpha) \left[ -\frac{1}{\rho_l} \frac{\partial}{\partial z} p_l + \frac{\nu}{r} \frac{\partial}{\partial r} r \frac{\partial U_z}{\partial r} - \frac{1}{r} \frac{\partial}{\partial r} \overline{ru'_z u'_r} \right] + \nu \frac{\partial U_z}{\partial r} \frac{\partial}{\partial r} (1-\alpha) - \overline{u'_z u'_r} \frac{\partial}{\partial r} (1-\alpha) + (1-\alpha)g + \frac{\sigma \kappa'}{\rho_l} \frac{\partial \chi'_b}{\partial z} - \frac{1}{\rho_l} \Phi_{b,z} \quad (7.5)$$

In the case of the surface tension term, du Cluzeau *et al.* (2020) models it as  $\frac{\sigma \kappa'}{\rho_l} \frac{\partial \chi'_b}{\partial z} \sim \nabla \alpha$  (see section 4.2.3). Considering this, since the flow is fully developed, the vertical component of the surface tension force term can be ignored. Also, if we define the sum of viscous stress and Reynolds stress as total stress,  $\tau = \tau_\mu + \tau_{uv} = \mu \frac{\partial U_z}{\partial r} - \rho_l \overline{u'_z u'_r}$ , the above equation is summarized as follows.

$$0 = (1-\alpha) \left[ -\frac{1}{\rho_l} \frac{\partial}{\partial z} p_l + \frac{1}{r \rho_l} \frac{\partial}{\partial r} r \tau \right] + \nu \frac{\partial U_z}{\partial r} \frac{\partial}{\partial r} (1-\alpha) - \overline{u'_z u'_r} \frac{\partial}{\partial r} (1-\alpha)$$

$$+(1-\alpha)g - \frac{1}{\rho_l} \Phi_{b,z} \quad (7.6)$$

Here we still do not have any information on the pressure term. So, let us move on to the radial component of the equation. With assuming  $\overline{u'_r u'_r} \approx \overline{u'_o u'_o}$ , we have

$$0 = -\frac{1}{\rho_l} \frac{\partial}{\partial r} \left[ (1-\alpha) p_l \right] + \overline{\sigma \kappa} \frac{\partial \chi_b}{\partial r} - \frac{\partial}{\partial r} (1-\alpha) \overline{u'_r u'_r} - \frac{1}{\rho_l} \Phi_{b,z} \quad (7.7)$$

On the other hand, in the single-phase pipe flow, the radial component of the RANS equation does not have the surface tension force term and the interfacial momentum transfer term. So,  $\partial p / \partial r = 0$  then,  $\partial \overline{p} / \partial z = d\overline{p}_o / dz$  with the following expression. Here, subscript “o” represents the parameter at the single-phase flow.

$$\frac{1}{\rho_l} \frac{d}{dz} p_o = \frac{\nu}{r} \frac{\partial}{\partial r} \left[ r \frac{\partial U_{z,o}}{\partial r} \right] + \left[ -r \overline{u'_{z,o} u'_{r,o}} \right] = \frac{1}{\rho_l r} \frac{\partial}{\partial r} r \tau_o \quad (7.8)$$

According to Michaelides *et al.* (2017), in the case of the volume void fraction has a value  $\alpha \sim 10\%$  or lower,  $\partial \overline{p} / \partial r \ll d\overline{p} / dz$  and  $d\overline{p} / dz = d\overline{p}_o / dz$ . Therefore, it is summarized as follows with total stress difference  $\Delta \tau = \tau - \tau_o$ . Here, we need to note that even though we neglected  $\partial \overline{p} / \partial r$  in the axial direction momentum equation, it does not imply that  $\partial \overline{p} / \partial r = 0$ . Indeed,  $\partial \overline{p} / \partial r$  is not zero, and accompanying the effect of surface tension, it is important to determine the void fraction in radial distribution (du Cluzeau *et al.* (2020a); du Cluzeau *et al.* (2020b)). Put (7.8) into (7.6):

$$0 = (1-\alpha) \left[ \frac{1}{r \rho_l} \frac{\partial}{\partial r} r \Delta \tau \right] + \nu \frac{\partial U_z}{\partial r} \frac{\partial (1-\alpha)}{\partial r} - \overline{u'_z u'_r} \frac{\partial (1-\alpha)}{\partial r} + (1-\alpha) g - \frac{1}{\rho_l} \Phi_{b,z} \quad (7.9)$$

Now when equation (7.9) is normalized by the bulk velocity  $U_c$ , and pipe radius  $R$ ,

$$0 = \frac{1}{r^*} \frac{\partial}{\partial r^*} r^* \Delta \tau^* + \frac{1}{(1-\alpha)} \frac{1}{Re_c} \frac{\partial U_z^*}{\partial r^*} \frac{\partial (1-\alpha)}{\partial r^*} - \frac{\overline{u_z^* u_r^*}}{(1-\alpha)} \frac{\partial (1-\alpha)}{\partial r^*} + \frac{1-\alpha}{Fr} - \frac{1}{(1-\alpha)} \frac{R}{\rho_l U_c^2} \Phi_{b,z} \quad (7.10)$$

We used dimensionless parameters having the following definition.  $Re = \frac{U_c R}{\nu}$ ,  $Fr = \frac{U_c^2}{gR}$ ,  $\kappa^* = \frac{\overline{d}_b}{2} \kappa'$ . In equation (7.10), the first term is a stress difference term

compared to the single-phase flow and the second and third terms are stress terms related to void fraction gradient. By the order of magnitude analysis, second and third terms appear to be smaller than the first term about an order. Since the constant  $I/Fr$  term does not affect the trend of change, the above equation becomes the following scaling relation.

$$-\frac{1}{r^*} \frac{\partial}{\partial r^*} r^* \Delta \tau^* \sim -\frac{1}{(1-\alpha)} \frac{R}{\rho_l U_c^2} \Phi_{b,z} \quad (7.11)$$

Because we are considering fully developed flow, so, there is no convective acceleration. Therefore,  $\Phi_{b,z} \approx \Phi_{b,N-\text{conv}}$ . Then equation (7.11) becomes as follows.

$$-\frac{1}{r^*} \frac{\partial}{\partial r^*} r^* \Delta \tau^* \sim -\frac{\alpha}{1-\alpha} \frac{V_R^2}{U_c^2} \frac{R}{d_b} \quad (7.12)$$

By integration on a radial coordinate, finally, we have the scaling relation (7.13). The left-hand side is the stress difference between the single and the two-phase flow (the total liquid momentum parameter in this flow geometry) and the right-hand side is the interfacial momentum transfer parameter.

$$-r^* \Delta \tau^* \sim \int_0^{r^*} \frac{\alpha}{1-\alpha} \frac{V_R^2}{U_c^2} \frac{R}{d_b} r'^* dr'^* \quad (7.13)$$

In this derivation, the important assumptions were about pressure gradient, which are  $\partial \bar{p} / \partial r \ll d \bar{p} / dz$ , and  $d \bar{p} / dz = d \bar{p}_o / dz$ . (Michaelides *et al.* (2017), in the case of  $\alpha \sim 10\%$  or lower). Equation (7.13) states that in upward bubbly pipe flow, the total liquid momentum parameter is defined as the total stress difference between the single- and two-phase flows, and the interfacial momentum transfer parameter is determined by integration of  $\Phi_{b,N-\text{conv}}$  along the radial direction. It is noted that the positive (negative)  $-r^* \Delta \tau^*$  represents the enhancement (suppression) of the total stress owing to bubbles. In the following, the suggested relation is going to be tested with existed results. Because most of the previous studies resolve the range  $0 \leq r/R < 0.9$  which satisfies that  $\tau \approx \tau_{uv}$ . Therefore, we considered only the Reynolds shear stress as  $\Delta \tau \approx \Delta \tau_{uv}$ .

The laminar bubbly pipe flow (Hosokawa & Tomiyama 2013; Kim *et al.* 2016) is shown in figure 7.3(a). As  $I$  increases,  $M_t$  increases correspondingly with constant slope independent to the flow conditions. However, there are some differences in  $M_t$  scales even at the same  $I$  which reflects the effects of the force coefficient as we already examined in the previous sections. Similar to previous systems, we figured out empirical relation as a function of parameters that contributing  $\Phi_{b,N-\text{conv}}$ , i.e., the drag force. We supposed that besides the bubble Reynolds number and the bubble Weber number, we need the averaged volume void fraction, the pipe Reynolds number (based on the pipe diameter and the bulk velocity of the single-phase flow), and the ratio of averaged bubble diameter to the pipe diameter for the bubbly pipe flow. As the bubble plume, because the system consists of the imposed bubbles on background shear flow, the averaged volume void fraction and the pipe Reynolds number considered. Also, according to

Michaelides *et al.* (2017), the relative size of the pipe compared to the bubble is an important factor in bubbly pipe flows, so we included  $\langle \bar{d}_b \rangle / D$ . As a result, we got an empirical relation  $M_t \sim I Re_b^{-0.6} Re^{1.8} \langle \alpha \rangle^{-0.4} (\langle \bar{d}_b \rangle / D)^4$  (figure 7.3(b)).  $We_b$  results in that it does not contribute to the relation between  $M_t$  and  $I$ . Interestingly,  $\langle \bar{d}_b \rangle / D$  has the strongest contribution and the next is  $Re$ . In addition,  $\langle \alpha \rangle$  has the smallest contribution except for  $We_b$ . By considering the fact that a small amount of  $\langle \alpha \rangle$  can make a substantial change in the liquid phase statistics (Kim *et al.* 2016; Hosokawa & Tomiyama 2013), this indicates that what matters is whether the bubbles are existed in the system whereas how many bubbles are imposed is less important.

For a turbulent bubbly pipe flow (Shawkat *et al.* 2008; Lee *et al.* 2021), the variation of  $M_t$  with  $I$  shows a quite different trend from those in other types of bubbly flow (figure 7.4(a)). In most cases,  $M_t$  increases with  $I$  as the previous systems. However, in some cases, the turbulence suppression is observed (see the inset in figure 7.4(a)). Here we also evaluated an empirical relation between  $M_t$  and  $I$  as a function of  $Re_b$ ,  $We_b$ ,  $Re$ ,  $\langle \alpha \rangle$ , and  $\langle \bar{d}_b \rangle / D$ . The result is,  $M_t \sim (I Re_b^{2.2} We_b^{-1.4} Re^{-2.2} \langle \alpha \rangle^{0.8} (\langle \bar{d}_b \rangle / D)^{-3.6})^{0.62}$ . Surprisingly, every exponent has an opposite sign compared to the laminar bubbly pipe flow, i.e., in the turbulent bubbly pipe flow, the drag coefficient changes with those parameters in a contrary way to that of the laminar bubbly pipe flow. However, the significance of each parameter is similar. In the turbulent bubbly pipe flow, the effect of the pipe size is the most important, and the pipe Reynolds number is the next as well. Also, the dependency on the averaged volume void fraction is relatively low. In addition, data corresponding to turbulence suppression separate more in figure 7.4(b). This indicates that the turbulence suppression has a different relation with those parameters (i.e.,  $Re_b$ ,  $We_b$ ,  $Re$ ,  $\langle \alpha \rangle$ , and  $\langle \bar{d}_b \rangle / D$ ) compared to the turbulence enhancement.

On the turbulence suppression, a little is known now. Shawkat *et al.* (2008) stated that the turbulence suppression occurs at high pipe Reynolds numbers with small volume void fraction based on their experimental data (which are referred to in the present study). The small volume void fraction condition coheres with the results from Lee *et al.* (2021). In the case of  $Re = 5300$ , the turbulence suppression occurred at  $\langle \alpha \rangle = 0.8\%$  whereas at  $\langle \alpha \rangle = 1.8\%$ , only the turbulence enhancement was observed. However, the results from Lee *et al.* (2021) do not match with the high Reynolds number condition. In Lee *et al.* (2021), turbulence suppression is more encouraged in the lower Reynolds number case (see the inset in figure 7.4(a)). This controversy came from the lack of detailed observation on the interaction between liquid eddies and bubbles. Turbulence suppression appears to be characterized hard by simple relation consists of bulk parameters such as Reynolds number and the volume void fraction. As Serizawa & Kataoka (1990) suggested, the turbulence suppression in a turbulent bubbly pipe flow might result from the interaction between bubble interface and eddies of liquid flow. To model this, it is necessary to observe the interaction between liquid eddies and bubbles in

detail and investigate how the interaction brings a decrease in turbulence.

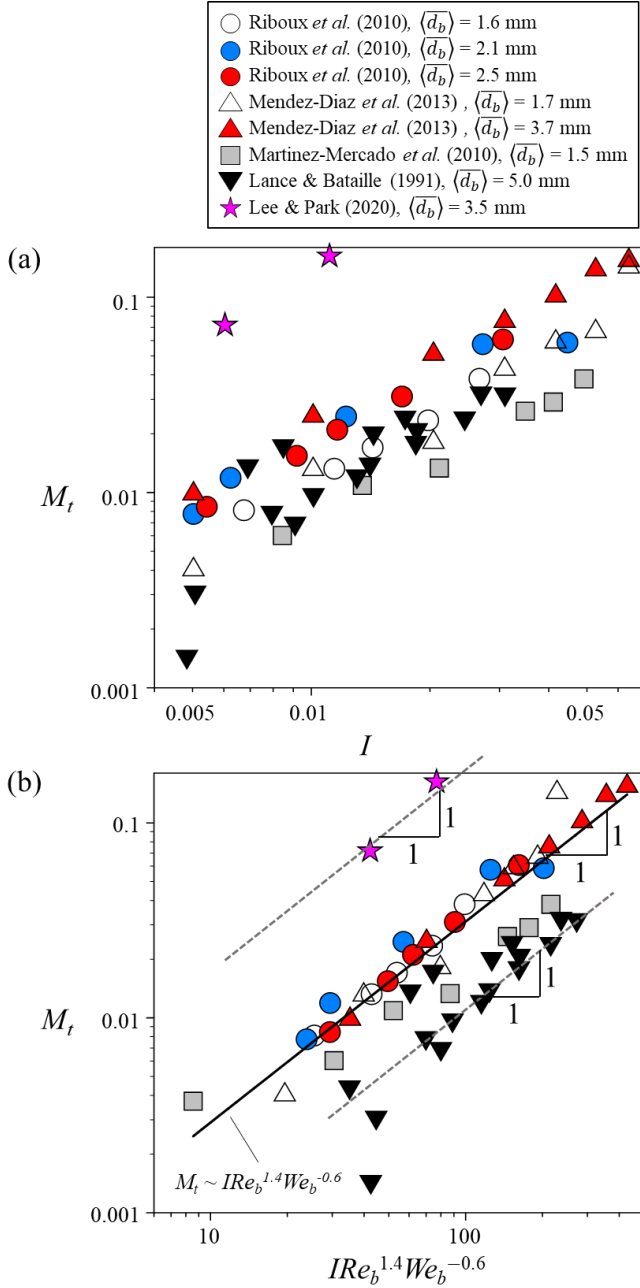


FIGURE 7.1. In the case of the homogeneous bubble swarm (Lance & Bataille 1991; Martinez-Mercado *et al.* 2007; Riboux *et al.* 2010; Mendez-Diaz *et al.* 2013; Lee & Park 2020), variation of total liquid momentum parameter ( $M_t = \overline{u'_z u'_z} / V_b^2$ ) with (a) the interfacial momentum transfer parameter ( $I = \alpha / (1 - \alpha)$ ) and (b) the interfacial momentum transfer parameter weighted by the bubble Reynolds number and the bubble Weber number. In (b), the solid line is  $M_t = 2.74 \times 10^{-4} IRe_b^{1.4}We_b^{-0.6}$ .

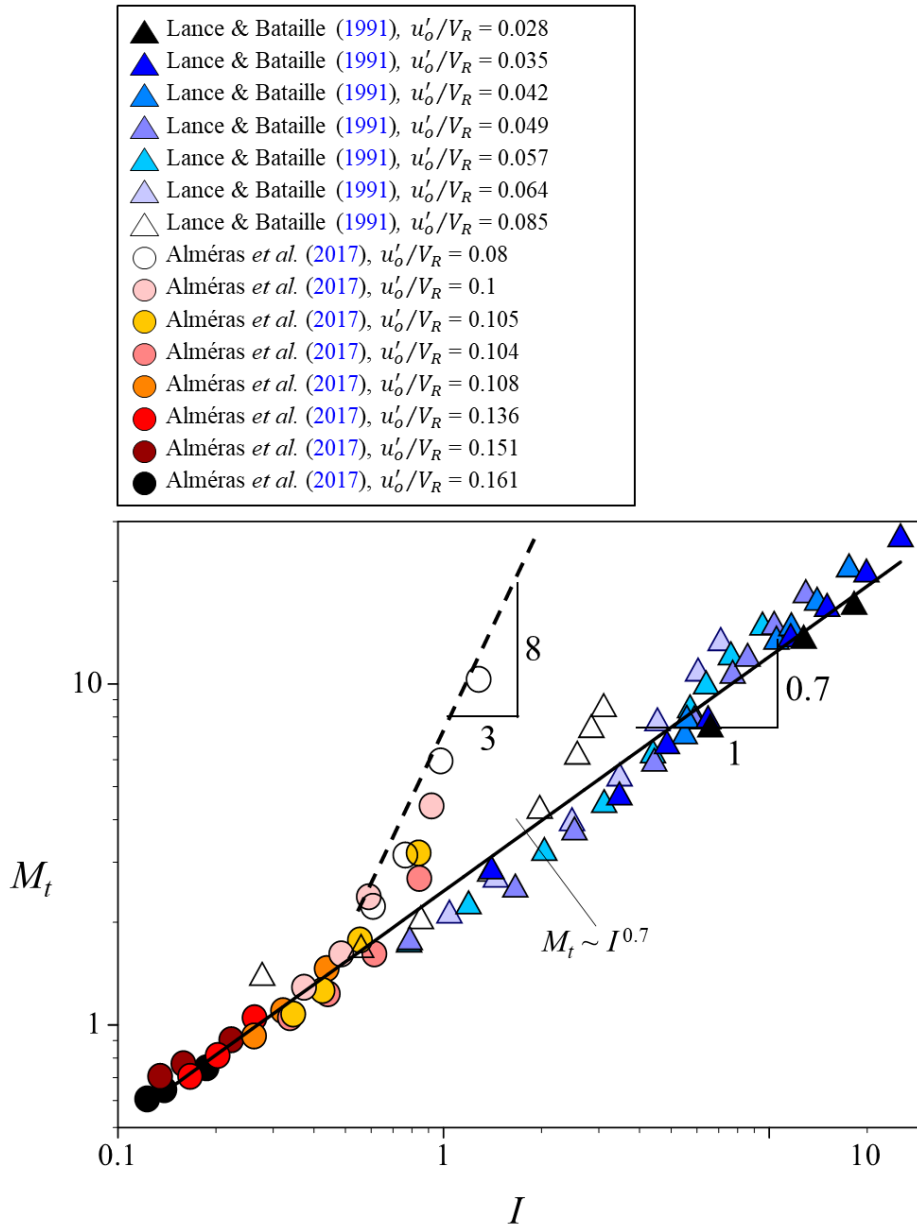


FIGURE 7.2. In the case of the rising bubbles under the prescribed grid turbulence (Lance & Bataille 1991; Alm eras *et al.* 2017), variation of total liquid momentum parameter ( $M_t = \overline{u'_z u'_z} / u_o'^2$ ) with the interfacial momentum transfer parameter ( $I = \alpha / (1 - \alpha) \cdot V_R^2 / u_o'^2$ ). The solid line is  $M_t = 2.5I^{0.7}$ .

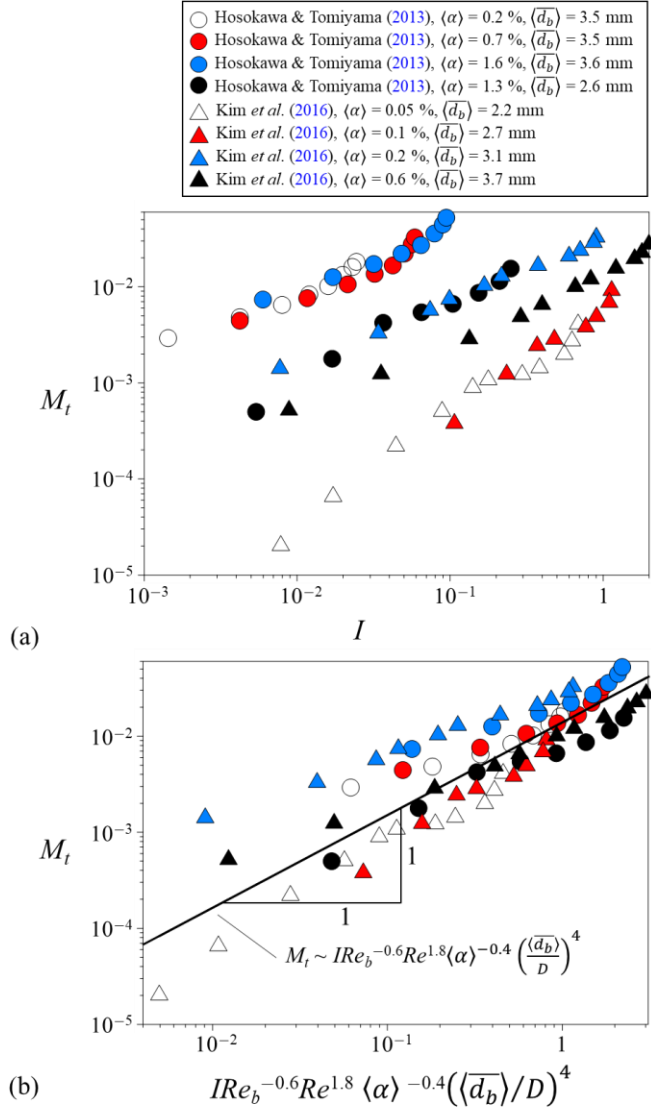


FIGURE 7.3. In the case of the laminar bubbly pipe flow (Hosokawa & Tomiyama 2013; Kim *et al.* 2016), total liquid momentum parameter ( $M_t = -r^* \cdot \Delta\tau / \rho_l U_c^2$ ) as a function of (a) the interfacial momentum transfer parameter ( $I = \int_0^{r^*} \alpha / (1 - \alpha) \cdot V_R^2 / U_c^2 \cdot R / d_b \cdot r'^* dr'^*$ ) and (b) the interfacial momentum transfer parameter weighted by the bubble Reynolds number, the pipe Reynolds number (based on the bulk velocity and the pipe diameter), the averaged volume void fraction and the ratio of averaged bubble diameter to the pipe diameter. In (b), the solid line is  $M_t = 0.014 I Re_b^{-0.6} Re^{1.8} \langle \alpha \rangle^{-0.4} (\langle \bar{d}_b \rangle / D)^4$ .

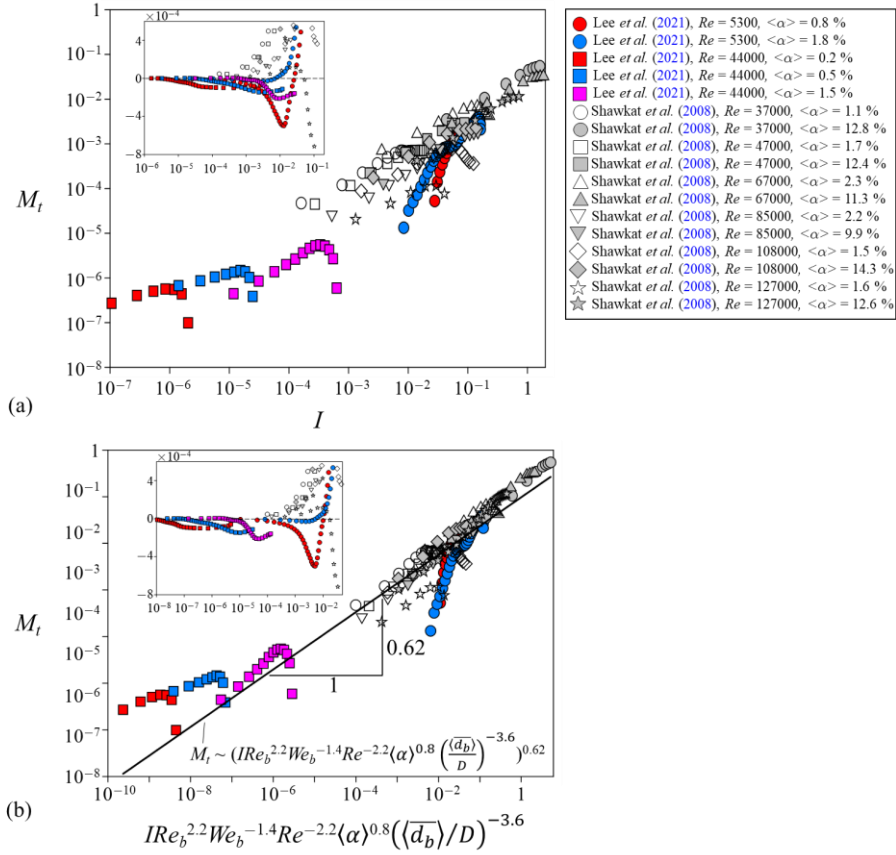


FIGURE 7.4. In the case of the turbulent bubbly pipe flow (Shawkat *et al.* 2008; Lee *et al.* 2021), total liquid momentum parameter ( $M_t = -r^* \cdot \Delta\tau / \rho_l U_c^2$ ) as a function of (a) the interfacial momentum transfer parameter ( $I = \int_0^{r^*} \alpha / (1 - \alpha) \cdot V_R^2 / U_c^2 \cdot R / d_b \cdot r'^* dr'^*$ ) and (b) the interfacial momentum transfer parameter weighted by the bubble Reynolds number, the bubble Weber number, the pipe Reynolds number (based on the bulk velocity and the pipe diameter), the averaged volume void fraction and the ratio of averaged bubble diameter to the pipe diameter. In (b), the solid line is  $M_t = 0.01(IRe_b^{2.2}We_b^{-1.4}Re^{-2.2}\langle \alpha \rangle^{0.8}(\overline{d_b}/D)^{-3.6})^{0.62}$ . The inset in (a) and (b) is the same graph with different range (it is drew by linear scale in y-axis to show the turbulence reduction).

## Bibliography

- Ainsworth C.H., Chassignet E.P., French-McCay D., Beegle-Krause C.J., Berenshtein I., Englehardt J., Fiddaman T., Huang H., Huettel M., Justic D., Kourafalou V.H., Liu Y., Mauritzen C., Murawski S., Morey S., Özgökmen T., Paris C.B., Ruzicka J., Saul S., Shepherd J., Socolofsky S., Solo Gabriele H., Sutton T., Weisberg R.H., Wilson C., Zheng L. & Zheng Y. 2021 Ten years of modeling the Deepwater Horizon oil spill. *Environ. Model. Softw.* 142, 105070.
- Alméras, E., Mathai, V., Lohse, D. & Sun, C. 2017 Experimental investigation of the turbulence induced by a bubble swarm rising within incident turbulence. *J. Fluid Mech.* **825**, 1091-1112.
- Asaeda, T. & Imberger J. 1993 Structure of bubble plumes in linearly stratified environments. *J. Fluid Mech.* 249, 35–57.
- Baker, S. & Matthews, I. 2004 Lucas-kanade 20 years on: A unifying framework. *Int. J. Comput. Vis.* 56, 221-255.
- Balachandar S. 2020. Lagrangian and Eulerian drag models that are consistent between Euler-Lagrange and Euler-Euler (two-fluid) approaches for homogeneous systems. *Phys. Rev. Fluids.* 5, 84302.
- Balachandar S. & Eaton J.K. 2010. Turbulent dispersed multiphase flow. *Annu. Rev. Fluid Mech.* 42, 111–133.
- Bombardelli, F. A., Buscaglia, G. C., Rehmann, C. R., Rincón, L. E. & García, M. H. 2007 Modeling and scaling of aeration bubble plumes: A two-phase flow analysis. *J. Hydraul. Res.* 45, 617-630.
- Boufadel, M. C., Socolofsky, S., Katz, J., Yang, D., Daskiran, C. & Dewar, W. 2020 A Review on Multiphase Underwater Jets and Plumes: Droplets, Hydrodynamics, and Chemistry. *Rev. Geophys.* 58, e2020RG000703.
- Bryant D.B., Seol D.-G. & Socolofsky S.A. 2009 Quantification of turbulence properties in bubble plumes using vortex identification methods. *Phys. Fluids.* 21, 75101.
- Cai S., Mémin E., Dérian P. & Xu C. 2018 Motion estimation under location uncertainty for turbulent fluid flows. *Exp. Fluids.* 59, 149–176.
- Craig V.S.J. 2004 Bubble coalescence and specific-ion effects. *Curr. Opin. Colloid Interface Sci.* 9, 178–184.
- Cui, Z. & Fan, L. S. 2004 Turbulence energy distribution in bubbling gas–liquid and gas–liquid–solid flow systems. *Chem. Eng. Sci.* 59, 1755-1766.
- Damaschke N., Kühn V. & Nobach H. 2018 A fair review of non-parametric bias-free autocorrelation and spectral methods for randomly sampled data in laser Doppler velocimetry. *Digit. Signal Process. A Rev. J.* 76, 22–33.
- Davidson, P. 2015 *Turbulence: An Introduction for Scientists and Engineers.* Oxford University

Press.

- Cederwall, K. & Ditmars, J. D. 1970 Analysis of Air-Bubble Plumes. Report No. KH-R-24, W. M. Keck Laboratory of Hydraulics and Water Resources, California Institute of Technology, Pasadena, Calif., Sept., 1970.
- du Cluzeau A., Bois G. & Toutant A. 2019 Analysis and modelling of Reynolds stresses in turbulent bubbly up-flows from direct numerical simulations. *J. Fluid Mech.* 866, 132–168.
- du Cluzeau, A., Bois, G. & Toutant, A. 2020a Modelling of the laminar dispersion force in bubbly flows from direct numerical simulations. *Phys. Fluids* 32, 012106.
- du Cluzeau, A., Bois, G., Toutant, A. & Martinez, J. M. 2020b On bubble forces in turbulent channel flows from direct numerical simulations. *J. Fluid Mech.* 882, A27.
- Fanneløp, T. K. & Sjoen, K. 1980 Hydrodynamics of underwater blowouts. In *Proceedings AIAA 18th Aerospace Sci. Meeting*, Pasadena, California. AIAA.
- Fraga, B. & Stoesser, T. 2016 Influence of bubble size, diffuser width, and flow rate on the integral behavior of bubble plumes. *J. Geophys. Res. Oceans* 121, 3887-3904.
- Gore R.A. & Crowe C.T. 1989 Effect of particle size on modulating turbulent intensity. *Int. J. Multiph. Flow.* 15, 279–285.
- Hosokawa, S. & Tomiyama, A. 2013 Bubble-induced pseudo turbulence in laminar pipe flows. *Int. J. Heat Fluid Flow* 40, 97-105.
- Hur Y.G., Yang J.H., Jung H. & Park S. Bin 2013 Origin of regime transition to turbulent flow in bubble column: Orifice- and column-induced transitions. *Int. J. Multiph. Flow.* 50, 89–97.
- Hussein H.J., Capp S.P. & George W.K. 1994 Velocity measurements in a high-Reynolds-number, momentum-conserving, axisymmetric, turbulent jet. *J. Fluid Mech.* 258, 31–75.
- Ishii, M. & Hibiki, T. 2011 *Thermo-Fluid Dynamics for Two-Phase Flow*. Springer.
- Kataoka, I., Besnard, D. C. & Serizawa, A. 1992 Basic equation of turbulence and modeling of interfacial transfer terms in gas–liquid two-phase flow. *Chem. Eng. Comm.* 118, 221-236.
- Kataoka, I., Serizawa, A. & Besnard, D. C. 1993 Prediction of turbulence suppression and turbulence modeling in bubbly two-phase flow. *Nucl. Eng. Des.* 141, 145-158.
- Kim, M., Lee, J. H. & Park, H. 2016 Study of bubble-induced turbulence in upward laminar bubbly pipe flows measured with a two-phase particle image velocimetry. *Exp. Fluids* 57, 55.
- Kim, Y. & Park, H. 2019 Upward bubbly flows in a square pipe with a sudden expansion: Bubble dispersion and reattachment length. *Int. J. Multiphas. Flow.* 118, 254-269.

- Kolev, N. I. 2015 *Multiphase flow dynamics 5: nuclear thermal hydraulics*. Springer.
- Lai, C. C. & Socolofsky, S. A. 2019 The turbulent kinetic energy budget in a bubble plume. *J. Fluid Mech.* 865, 993-1041.
- Landeau M., Deguen R. & Olson P. 2014 Experiments on the fragmentation of a buoyant liquid volume in another liquid. *J. Fluid Mech.* 749, 478–518.
- Lance, M. & Bataille, J. 1991 Turbulence in the liquid phase of a uniform bubbly air–water flow. *J. Fluid Mech.* 222, 95-118.
- Lee, J. H., Kim, H., Lee, J. & Park, H. 2021 Scale-wise analysis of upward turbulent bubbly flows: an experimental study. submitted to *Phys. Fluids*.
- Lee, J. & Park, H. 2020 Bubble dynamics and bubble-induced agitation in the homogeneous bubble-swarm past a circular cylinder at small to moderate void fractions. *Phys. Rev. Fluids* 5, 054304.
- Li G, Wang B., Wu H. & DiMarco S.F. 2020 Impact of bubble size on the integral characteristics of bubble plumes in quiescent and unstratified water. *Int. J. Multiph. Flow.* 125, 103230.
- Li Z., Wang G., Yousaf M., Yang X. & Ishii M. 2018 Flow structure and flow regime transitions of downward two-phase flow in large diameter pipes. *Int. J. Heat Mass Transf.* 118, 812–822.
- Lima Neto I.E., Cardoso S.S.S. & Woods A.W. 2016 On mixing a density interface by a bubble plume. *J. Fluid Mech.* 802, R3.
- Ling Y., Parmar M. & Balachandar S. 2013 A scaling analysis of added-mass and history forces and their coupling in dispersed multiphase flows. *Int. J. Multiph. Flow.* 57, 102–114.
- Liu T. & Shen L. 2008 Fluid flow and optical flow. *J. Fluid Mech.* 614, 253–291.
- Ma, T., Santarelli, C., Ziegenhein, T., Lucas, D. & Fröhlich, J. 2017 Direct numerical simulation-based Reynolds-averaged closure for bubble-induced turbulence. *Phys. Rev. Fluids* 2, 034301.
- Ma, T., Lucas, D. & Bragg, A. D. 2020a Explicit algebraic relation for calculating Reynolds normal stresses in flows dominated by bubble-induced turbulence. *Phys. Rev. Fluids* 5, 084305.
- Ma, T., Lucas, D., Jakirlić, S. & Fröhlich, J. 2020b Progress in the second-moment closure for bubbly flow based on direct numerical simulation data. *J. Fluid Mech.* 883, A9.
- Martínez-Mercado J., Palacios-Morales C.A. & Zenit R. 2007 Measurement of pseudoturbulence intensity in monodispersed bubbly liquids for  $10 < Re < 500$ . *Phys. Fluids.* 19, 103302.
- Mazzitelli I.M. & Lohse D. 2009. Evolution of energy in flow driven by rising bubbles. *Phys. Rev. E*, 79: .
- Mcdougall T.J. 1978 Bubble plumes in stratified environments. *J. Fluid Mech.* 85, 655–672.

- Mendez-Diaz S., Serrano-García J.C., Zenit R. & Hernández-Cordero J.A. 2013 Power spectral distributions of pseudo-turbulent bubbly flows. *Phys. Fluids*. 25, 43303.
- Michaelides, E. E., Crowe, C. T. & Schwarzkopf, J. D. 2017 *Multiphase Flow Handbook*, 2nd edn. CRC Press.
- Milgram, J. H. 1983 Mean flow in round bubble plumes. *J. Fluid Mech.* 133, 345-376.
- Milgram, J. H. & Van Houten, R. J. 1982 Plumes from sub-sea well blowouts. In *Proceedings of the 3rd International Conference, BOSS*, vol. I, pp. 659–684. MIT
- Montoya, G., Lucas, D., Baglietto, E. & Liao, Y. 2016 A review on mechanisms and models for the churn-turbulent flow regime. *Chem. Eng. Sci.* 141, 86-103.
- Mudde, R. F., Groen, J. S. & van den Akker, H. E. A. 1997 Liquid velocity field in a bubble column: LDA experiments. *Chem. Eng. Sci.* 52, 4217-4224.
- Mudde, R. F. & Saito, T. 2001 Hydrodynamical similarities between bubble column and bubbly pipe flow. *J. Fluid Mech.* 437, 203-228.
- Nedeltchev S. & Shaikh A. 2013 A new method for identification of the main transition velocities in multiphase reactors based on information entropy theory. *Chem. Eng. Sci.* 100, 2–14.
- Olsthoorn J. & Dalziel S.B. 2015 Vortex-ring-induced stratified mixing. *J. Fluid Mech.* 781, 113–126.
- Otsu, N. 1979 A Threshold Selection Method from Gray-Level Histograms. *IEEE Trans. Syst. Man Cybern.* 9: 62–66.
- Prakash, V. N., Mercado, J. M., Van Wijngaarden, L., Mancilla, E., Tagawa, Y., Lohse, D. & Sun, C. 2016 Energy spectra in turbulent bubbly flows. *J. Fluid Mech.* 791, 174-190.
- Pope, S. B. 2000 *Turbulent Flows*. Cambridge University Press.
- Rensen, J., Luther, S. & Lohse, D. 2005 The effect of bubbles on developed turbulence. *J. Fluid Mech.* 538, 153-187.
- Riboux, G., Risso, F. & Legendre, D. 2010 Experimental characterization of the agitation generated by bubbles rising at high Reynolds number. *J. Fluid Mech.* 643, 509-539.
- Risso, F. 2011 Theoretical model for  $k^{-3}$  spectra in dispersed multiphase flow. *Phys. Fluids* 23, 011701.
- Risso, F. 2016 Physical interpretation of probability density functions of bubble-induced agitation. *J. Fluid Mech.* 809, 240-263.
- Risso, F. 2018 Agitation, mixing, and transfers induced by bubbles. *Annu. Rev. Fluid Mech.* 50, 25-48.
- Risso, F. & Ellingsen, K. 2002 Velocity fluctuations in a homogeneous dilute dispersion of high-Reynolds-number rising bubbles. *J. Fluid Mech.* 453, 395-410.
- Roghair, I., Martínez Mercado, J., Van Sint Annaland, M., Kuipers, J. A. M.,

- Sun, C. & Lohse, D. 2011 Energy spectra and bubble velocity distributions in pseudo-turbulence: numerical simulations versus experiments. *Int. J. Multiphas. Flow* 37, 1-6.
- Sato, Y. & Sekoguchi, K. 1975 Liquid velocity distribution in two-phase bubble flow. *Int. J. Multiphas. Flow*, 2, 79-95.
- Sato, Y., Sadatomi, M. & Sekoguchi, K. 1981 Momentum and heat transfer in two-phase bubble flow-I. Theory. *Int. J. Multiphase Flow*, 7, 167-177.
- Schlegel J.P., Macke C.J., Hibiki T. & Ishii M. 2013 Modified distribution parameter for churn-turbulent flows in large diameter channels. *Nucl. Eng. Des.* 263, 138–150.
- Serizawa, A. & Kataoka, I. 1990 Turbulence suppression in bubbly two-phase flow. *Nucl. Eng. Des.* 122, 1-16.
- Seol D.G., Bryant D.B. & Socolofsky S.A. 2009 Measurement of behavioral properties of entrained ambient water in a stratified bubble plume. *J. Hydraul. Eng.* 135, 983–988.
- Shawkat, M. E., Ching, C. Y. & Shoukri, M. 2008 Bubble and liquid turbulence characteristics of bubbly flow in a large diameter vertical pipe. *Int. J. Multiphas. Flow*, 34, 767-785.
- Simiano, M., Lakehal, D., Lance, M. & Yadigaroglu, G. 2009 Turbulent transport mechanisms in oscillating bubble plumes. *J. Fluid Mech.* 633, 191-231.
- Socolofsky S.A., Adams E.E. & Sherwood C.R. 2011 Formation dynamics of subsurface hydrocarbon intrusions following the Deepwater Horizon blowout. *Geophys. Res. Lett.* 38.
- Strang E.J. & Fernando H.J.S. 2001 Entrainment and mixing in stratified shear flows. *J. Fluid Mech.* 428, 349–386.
- Tennekes, H. & Lumley, J. L. 1972 *A First Course in Turbulence*. MIT Press
- Van Wijngaarden L. 1998 On pseudo turbulence. *Theor. Comput. Fluid Dyn.* 10, 449–458.
- Velte C.M., George W.K. & Buchhave P. 2014 Estimation of burst-mode LDA power spectra. *Exp. Fluids.* 55, 1674.
- Wang, B., Lai, C. C. & Socolofsky, S. A. 2019 Mean velocity, spreading and entrainment characteristics of weak bubble plumes in unstratified and stationary water. *J. Fluid Mech.* 874, 102-130.
- Wüest, A., Brooks, N. H. & Imboden, D. M. 1992 Bubble plume modelling for lake restoration. *Water Resour. Res.* 28, 3235-3250.
- Xue N., Khodaparast S. & Stone H.A. 2019 Fountain mixing in a filling box at low Reynolds numbers. *Phys. Rev. Fluids.* 4, 1–13.
- Yang D., Chen B., Socolofsky S.A., Chamecki M. & Meneveau C. 2016 Large-eddy simulation and parameterization of buoyant plume dynamics in stratified flow. *J. Fluid Mech.* 794, 798–833.
- Zhou X., Sun X. & Liu Y. 2016 Liquid-phase turbulence measurements in air-water two-phase flows over a wide range of void fractions. *Nucl. Eng. Des.* 310, 534–543.

# 기포 플룸에 의해 유도되는 난류 혼합에 대한 실험 및 이론 연구

서울대학교 대학원  
기계항공공학부  
김현석(KIM HYUNSEOK)

## 요약

기포 플룸에 의한 난류 혼합은 넓은 스케일에 걸쳐 일어나며( $\alpha 100 \mu\text{m}$ )~  $\alpha 1 \text{ km}$ ), 기상과 액상의 복잡한 상호 작용 속에 진행되기 때문에 이에 대한 정밀하고 체계적인 이해가 반드시 필요하다. 그러나 기존의 연구들은 기포 플룸을 평균유동의 관점에서만 해석함으로써 기포 플룸의 복잡한 거동과 기포-액체 상호작용에 의해 발생하는 난류량에 대해서는 고려하지 않아왔다. 본 연구에서는 그림자 기법, 옵티컬 플로 방법, 도플러 유속계 등의 광학 기반 고정밀 실험 기법을 활용하여 conventional 및 churn-turbulent, 두가지 종류의 기포 플룸에 대해 기포 플룸의 불안정성과 기포 유발 난류의 성질을 상세히 살펴보고, 이들을 규정하는 특성 길이와 속도, 시간 스케일을 제시하고 상관관계를 밝힌다. 기포 플룸을 규정하는 길이 스케일은 진행 방향으로서는 부력 특성 길이  $D_m$ , 반경 방향으로서는 기포 플룸 반경  $r_{1/2}$ 였고, 속도 스케일은 기포 상대 속도( $V_{Ro}$ )와 액체 중심 속도( $U_c$ )였다. 또한 특성 시간은 integral 시간 스케일이었다. 기포 플룸의 종류에 상관 없이 기포 플룸의 불안정성과 난류 통계량은 진행 방향으로서는  $z/D_m$ 의 함수로 기술되었는데,  $z = D_m$ 을 기준으로 물리량들이 빠르게 변화하는 adjustmet region과 수렴하는 asymptotic region으로 나뉘는 것을 확인하였다. 또한 반경 방향 분포는  $r/r_{1/2}$ 로 잘 기술 됨을 확인하였으며, 이와 같은 큰 스케일의 특성 속도, 길이, 시간 스케일이 기포 플룸의 특징을 잘 나타낼 수 있음을 정량적으로 확인하였다. 난류 에너지 스펙트럼을 통해서 기포에 의한 난류 에너지 생성이 플룸 스케일에서 일어난다는 것을 확인하였으며, 이는 기포 플룸의 물리량이 큰 특성 스케일들로 잘 규정될 수 있음을 뒷받침 한다. 큰 특성 스케일로 묘사하지 못하는, 기포 플룸 종류에 따른 수렴 난류량의 차이를 설명하기 위해 이상 나비에-스톡스 방정식으로부터 기포 유발 난류와 기체상 사이의 상관 관계를 규정하는 이론적인 체계를 수립하였고, 확립한 이론적 방법론을 다양한 기포류 유동 형상에 대해 검증하여 본 연구에서 제시한 방법론이 기존의 경험적 관계식을 이론적으로 합리화 할 수 있음을 밝혔다. 또한 이를 통해 기포 유발 난류의 구체적인 경향을 예측하기 위해서는 각 상황에 적합한 기체-액체 상호작용에 대한 고려가 반드시 필요함을 확인하였다. 획득된 이해를 토대로 최종적으로는 기포 플룸으로 안정한 밀도층을 가지는 유체를 혼합할 때 발생하는 혼합 패턴을 결정하는

기준과 혼합 속도에 대한 스케일링 관계식을 제시하였다. 혼합 패턴은 초기 조건들로 구성된, 기포 플룸에 가해지는 부력과 유체층에 가해지는 중력의 단순 비율로 쉽게 예측할 수 있었고, 혼합 속도는 기포 플룸에서 기체-액체 상호작용의 대표 속도와 유체층을 안정화 시키는 중력의 비율로 정의되는 Froude 수로 잘 기술 된다는 것을 확인하였다. 본 연구는 정확한 실험 결과에 기반하여 매우 복잡한 유동 현상인 기포 플룸에 의한 난류 유체 혼합에 대해 평균 유동에 대한 거시적인 기술부터 난류 통계량에 대한 구체적인 스케일링 관계식에 이르기까지 아울러 제시함으로써 실제 기포 플룸 유체 혼합이 일어나는 산업 현장에서 곧바로 활용할 수 있는 유용한 지식은 물론, 기포류 유동의 물리적 특징을 이해하는데 도움이 되는 학술적 성과들을 제공한다.

**주요어** : 유체 혼합, 난류 혼합, 안정한 유체층, 기포류 유동, 기포 플룸, 기포 유발 난류

**학번** : 2013-23064